Copyright is owned by the Author of the thesis. Permission is given for a copy to be downloaded by an individual for the purpose of research and private study only. The thesis may not be reproduced elsewhere without the permission of the Author.

A Spectroscopic Analysis of Ionic Liquid Properties

A thesis presented in partial fulfilment of the requirements for the degree of

Master of Science
in
Nanoscience

at Massey University, Manawatū,
New Zealand.

Ashley Jacqulyne Way

2013

Abstract

The use of ionic liquids in chemical processes is becoming of increasing interest, due to the low volatility of ionic liquids, and the wide range of properties which they possess. The ability to select properties based on anion and cation choice is also desirable. As such, the development of a solvent reorganization energy scale incorporating both common organic solvents and ionic liquids is useful, as it can be used to determine appropriate ionic liquid replacements of common organic solvents for use in applications.

Raman spectroscopy studies have been performed on solutions of the solvatochromic Reichardt's dye in a selection of common organic and ionic liquid solvents. Due to the solvatochromism of Reichardt's dye, it behaves differently in solvents with differing properties. As such, the cross-sections of bands in Raman spectra associated with Reichardt's dye differ between solvents also. Modelling of these cross-sections enables solvent properties to be determined.

Absorption spectra were acquired of each sample, and resonance Raman spectra of each sample were recorded at a range of excitation wavelengths. After appropriate data treatment, the absorption and Raman cross-sections were determined, in order to enable the modelling of absorption and Raman cross-section profiles. The modelling of these profiles enabled the solvent reorganization energy of the organic solvents and ionic liquids to be determined, and a relative scale of solvent reorganization prepared.

Computational studies were performed in order to better understand the dynamics of Reichardt's dye in solution. The results from the studies were used to assign the vibrational modes of the Reichardt's dye to bands in the resonance Raman spectra.

From a solvent reorganization standpoint, it was found that common organic solvents may be replaced by ionic liquids of similar properties in applications where solvent volatility is an issue. In addition to this, the information obtained through the use of the solvent reorganization energy scale is able to be directly related to applications of ionic liquids involving electron transfer.

Acknowledgements

Firstly, I would like to thank my supervisor Assoc. Prof. Mark Waterland for his continued help and support throughout this project. I would also like to thank Tracey McLean for her assistance with the modelling of Raman intensities.

A part of this work was completed at the University of Otago in April 2012. This would not have been possible without the award of a Massey University Institute of Fundamental Sciences Postgraduate Student Travel Fund Grant. This work was presented at the 2011 Australasian Conference on Vibrational Spectroscopy (ACOVS9) in Wellington (22nd-24th November 2011) and at the Sixth International Conference on Advanced Materials and Nanotechnology (AMN6) in Auckland (11th-15th February 2013). Attendance at these conferences would not have been possible without travel funding from the New Zealand Institute of Chemistry, Manawatu Branch.

Finally, and most importantly, I would like to thank my family, especially my father, who sadly passed away last year, for their continued support throughout my studies.

Contents

Abstract ..... **i**

Acknowledgements ..... **ii**

List of Figures and Tables ..... **vii**

Glossary of ionic liquid names ..... **x**

Cations x

Anions x

Chapter 1 – Introduction 1

1.1 Ionic Liquids 1

1.2 Reichardt's Dye and Solvatochromism 3

1.3 The $E_T(30)$ solvent polarity scale 5

1.4 Aims of the Thesis 7

1.5 Reorganization Energy 8

1.6 Homogeneous Broadening and Reorganization Energy 10

1.7 Inhomogeneous Broadening 11

1.8 Computational studies of Reichardt's Dye 11

1.9 Summary 12

Chapter 2 - The Theory of Raman Intensities 13

2.1 The Classical Model 13

2.2 The Quantum Mechanical Model 15

2.3 The Time-Domain Picture 19

2.4 Solvent Broadening Models in Time-Domain Picture 24

Chapter 3 – Experimental 27

3.1 Synthesis and Purification 27
3.1.1 1-butyl-3-methylimidazolium chloride (BMIM Cl) Synthesis 27
3.1.2 1-butyl-3-methylimidazolium bis(trifluoromethanesulfonyl)-amide (BMIM TFSA) Synthesis 27
3.1.3 Purification of Reichardt's Dye 28
3.1.4 Issues with Reichardt's dye and Solvent Impurities 28

3.2 Resonance Raman of RTILs as solvents 29
3.2.1 Data acquisition at Massey University 29
3.2.1.1 Experimental Setup 488nm 29
3.2.1.2 Experimental Setup 515nm 30
3.2.1.3 Experimental Setup 633nm 30
3.2.2 Data acquisition at Otago University 30
3.2.2.1 Experimental Setup 532nm 30
3.2.2.2 Experimental Setup 568nm 31
3.2.2.3 Experimental Setup 594nm 31
3.2.2.4 Experimental Setup 647nm 31

3.3 Resonance Raman Intensity Analysis 31
3.3.1 Conversion from Relative Intensity to True Intensity 32
3.3.2 Background Subtraction 33
3.3.3 Peak Fitting 35
3.3.4 Calculation of Solvent Cross-Sections 40
3.3.5 Calculation of Solute Cross-Sections 42

3.4 Raman Intensity Modelling 42
3.4.1 Transition Dipole Length 42
3.4.2 Preparing Input Files 43
3.4.2.1 Absorption Spectra 43
3.4.2.2 Cross-Sections 43
3.4.2.3 Final Input File 44
3.4.3 Initial Simulations 47
3.4.4 Raman Profiles 48

3.5 Computational Studies 49

Chapter 4 – Reichardt's Dye in Common Solvents 50

4.1 Reichardt's Dye Absorption Spectra 50

4.2 Reichardt's Dye resonance Raman Spectra and Computational Studies 52

4.2.1 Reichardt's Dye resonance Raman Spectra 52

4.2.2 Reichardt's Dye Computational Studies 53

4.2.2.1 Frequency Shift Analysis 60

4.2.3 Resonance Raman Spectra of Reichardt's Dye in Common Organic Solvents 62

4.3 Reichardt's Dye Modelling 65

4.3.1 Reichardt's Dye in Acetonitrile 65

4.3.2 Reichardt's Dye in Dichloromethane 67

4.3.3 Reichardt's Dye in Dimethylsulfoxide 70

4.3.4 Reichardt's Dye in Ethanol 72

4.3.5 Reichardt's Dye in Methanol 75

4.3.6 Results of Reichardt's Dye Modelling in Common Organic Solvents 77

Chapter 5 – Reichardt's Dye in Ionic Liquids 81

5.1 Reichardt's Dye Absorption Spectra 81

5.2 Reichardt's Dye resonance Raman Spectra 83

5.3 Reichardt's Dye Modelling 86

5.3.1 Reichardt's Dye in BMIM OAc 86

5.3.2 Reichardt's Dye in BMIM PF_6 88

5.3.3 Reichardt's Dye in BMIM TFSA 89

5.3.4 Reichardt's Dye in BMMIM TFSA 92

5.3.5 Reichardt's Dye in BMPY TFSA 94

5.3.6 Results of Reichardt's Dye Modelling in Ionic Liquids 96

5.4 Reliability of Modelling of Raman Profiles 96

5.5 Properties of Ionic Liquids 97

Chapter 6 – Conclusion 100

6.0 Conclusion 100

6.1 Future Work 101

Bibliography 102

Appendices 111

Appendix One – Ionic Liquid Solvent Bands 111

BMIM OAc Raman band positions 111

BMIM PF_6 Raman band positions 111

BMIM TFSA Raman band positions 111

BMMIM TFSA Raman band positions 112

BMPY TFSA Raman band positions 112

List of Figures and Tables

Figure 1.1 - Anions and cations which are often used in ionic liquid synthesis.....1

Figure 1.2 - Electrochemical windows of a selection of ionic liquids from MD + DFT calculations.....2

Figure 1.3 - Reichardt's dye 3

Figure 1.4 - The influence of solvent choice on the electronic structure and intramolecular charge-transfer visible absorption of Reichardt's dye.....4

Figure 1.5 - Reichardt's dye in a selection of common solvents 5

Figure 1.6 - Reichardt's dye in a selection of ionic liquids 5

Figure 1.7 - Normalized ET(30) scale for a range of common molecular solvents and ionic liquids.....6

Figure 1.8 - Activation Energy diagram for Potential Surfaces 8

Figure 1.9 – Marcus Theory Diagram showing reorganization parameters.....9

Figure 2.1 - Stokes, Rayleigh, and anti-Stokes scattering.....14

Figure 2.2 - The time-dependent picture 20

Figure 2.3 - Raman cross-section.....21

Figure 2.4 – Time-dependent wavepacket overlap function for single vibrational mode.....22

Figure 2.5 – Time-dependent wavepacket overlap function decay due to multi-mode effect.....23

Figure 2.6 – Propagation of wavepacket centre on electronic excited-state surface 23

Figure 2.7 - The Brownian oscillator model is able to be applied to resonance Raman modelling.....25

Figure 3.1 - Example of "ICorr" window in Origin after conversion 32

Figure 3.2 - Peak Analyzer in Origin.....33

Figure 3.3 - Subtracting a linear background in Origin.....34

Figure 3.4 - Subtracting a non-linear background in Origin 34
Figure 3.5 - After modifying points for user defined baseline subtraction in Origin 35
Figure 3.6 - Final stage of subtracting baseline from non-linear data in Origin 35
Figure 3.7 - The Fit Peaks function in Origin can be used for peak fitting 36
Figure 3.8 - The "Auto Find" function in Origin 36
Figure 3.9 - Adding peaks manually for peak fitting 37
Figure 3.10 - Selecting the fitting function 37
Figure 3.11 - Applying bounds to the fitting function 38
Figure 3.12 - Selecting the tolerance and number of iterations to be performed 38
Figure 3.13 - An example of a spectrum fitted with a Chi-Sqr tolerance of 1x10-12 39
Figure 3.14 - Fitting output summary 39
Figure 3.15 - The peak information given through the peak fitting function 40
Figure 3.16 - The code builder in Origin 48
Figure 4.1 - Overlaid absorption spectra for Reichardt's dye in common organic solvents 50
Figure 4.2 - Experimental and simulated absorption spectra of common organic solvents 51
Figure 4.3 - Resonance Raman Spectrum of Reichardt's Dye in Ethanol, 532nm excitation 52
Figure 4.4 - Labelling of Reichardt's dye rings 55
Figure 4.5 - Reichardt's HOMO; Mode 145 55
Figure 4.6 - Reichardt's LUMO; Mode 146 56
Figure 4.7 - Stretching across the nitrogen in Reichardt's Dye (Mode 152) 57
Figure 4.8 - A selection of vibrational modes of Reichardt's dye 58
Figure 4.9 - Mode assignment for 1360 cm-1 Raman peak 59

Figure 4.10 - Resonance Raman Spectra of Reichardt's Dye in common organic solvents 63

Figure 5.1 - Absorption spectra of Reichardt's dye in ionic liquids 81

Figure 5.2 - Experimental and simulated absorption spectra of ionic liquids 82

Figure 5.3 - Resonance Raman Spectra of Reichardt's Dye in ionic liquids. 83

Figure 5.4 - Relative scale of homogeneous broadening of common organic solvents and ionic liquids 98

Figure 5.5 - Normalized ET(30) scale for a range of common molecular solvents .. 98

Figure 5.6 - Relative scale of reorganization energies of common organic solvents and ionic liquids 99

Table 4.1 - Mode information for Reichardt's dye in Ethanol 54

Table 4.2 - Frequency shift analysis of the 1295 cm-1 Reichardt's Dye Raman peak 61

Table 4.3 - Electronic properties of common organic solvents from modelling of absorption and Raman profiles 78

Table 4.4 - Reorganization energies of a selection of common organic solvents, from literature 78

Table 5.1 - Electronic properties of ionic liquids from modelling of absorption and Raman profiles 96

Glossary of ionic liquid names

The names of ionic liquids are formed through the combination of the names of the cations and anions present. The acronyms for the cations and anions used in this study are listed below with the corresponding systematic name. The acronyms are used predominantly in this thesis for ease of comparison between ionic liquids.

Cations

BMIM ……. 1-butyl-3-methylimidazolium

BMPY …….. 1-butyl-3-methypyridinuim

BMMIM …….. 1-butyl-2,3-dimethylimidazolium

Anions

PF6 ……. hexafluorophosphate

OAc ……... acetate

TFSA ……... bis(trifluoromethylsulfonyl)imide

Chapter 1 – Introduction

1.1 Ionic Liquids

The term "ionic liquid" is used to describe a solution which is composed entirely of ions.[2] Ionic liquids (ILs) are essentially liquid salts, for example, molten sodium chloride.[3, 4] This means that solutions of salts, even those which are saturated, are not able to be referred to as "ionic liquids". Recently the term "ionic liquid" has come to mean salts which are generally liquid below 100°C and have low viscosity.[5-7] In addition, the term "room temperature ionic liquid" (or RTIL) has come to mean an ionic liquid which is in a liquid state at room temperature.[8]

Figure 1.1 shows a selection of common cations and anions used in ionic liquid synthesis. For the five cations and seven anions shown, there are thirty-five combinations possible, and, as the properties of ionic liquids are very dependent on the anion and cation involved, this leads to a wide range of liquids with differing properties being able to be made by simply switching either anion or cation.[9, 10] This is advantageous over traditional solvents, as they are generally purchased individually with specific tasks in mind. Due to ionic liquids generally having negligible vapour pressure and very low volatility they can be considered as environmentally benign solvents, leading to them being considered viable potential replacements for most common laboratory solvents, which are generally volatile organic compounds.[7, 11-15]

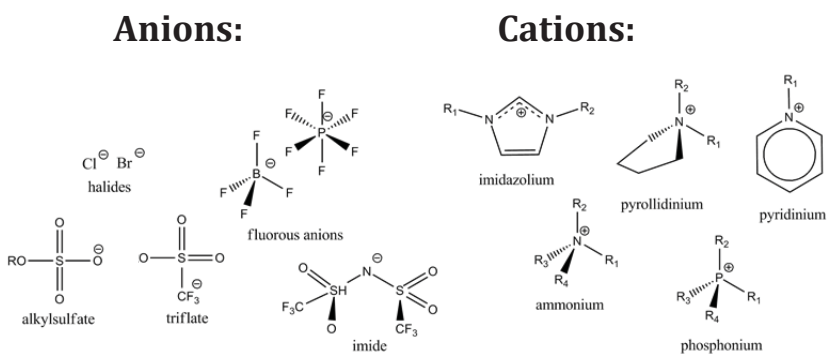


Figure 1.1 - Anions and cations which are often used in ionic liquid synthesis

Whilst ionic liquids generally have high boiling points, changing the anion or cation can have a substantial effect on the boiling point of the liquid.[7] As an example, changing the cation in the ionic liquid 1-ethyl-3-methylimidazolium

tetrafluoroborate (EMIM BF_4) so the ionic liquid becomes 1-methyl-3-butylimidazolium tetrafluoroborate (BMIM BF_4) causes the boiling point to change from 438.9K to 484.6K,[16] whilst changing the anion in 1-methyl-3-butylimidazolium tetrafluoroborate (BMIM BF_4) to form 1-methyl-3-butylimidazolium bis(trifluoromethylsulfonyl)imide (BMIM TFSA) causes a change in boiling point from 484.6K to 851.8K,[16] which is nearly a 400 degree change. Putting this into perspective, the extent of this change is larger than the difference in boiling points of nitrogen (77.4K) and water (373.2K).

The oxidation and reduction of the anions and cations respectively determine the electrochemical cathodic and anodic limits of ionic liquids,[9] giving a range within which RTILs are able to be used in electrochemical applications,[6] including electrochemical deposition.[12] The electrochemical windows of a number of ionic liquids have been measured[9, 17] and are shown in Figure 1.2. It is evident that, in this example, changing the cation has an effect on the width of the electrochemical window, whilst changing the anion tends to cause the maximum and minimum values to shift potentials.

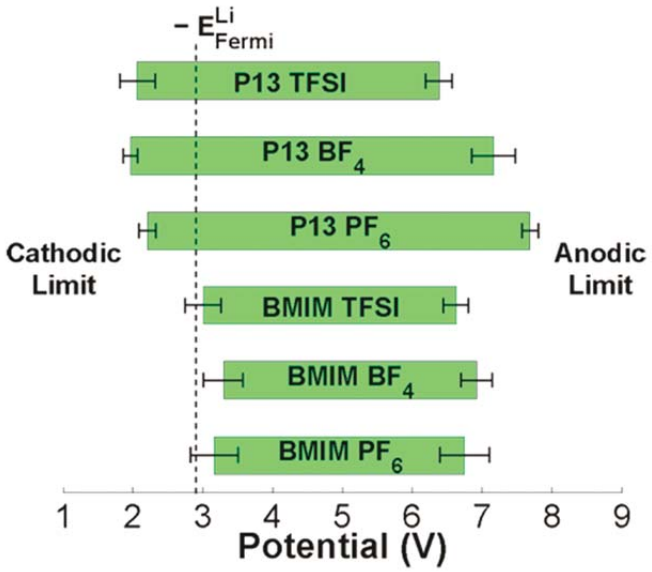


Figure 1.2 - Electrochemical windows of a selection of ionic liquids from MD + DFT calculations. P13 is *N,N*-propylmethylpyrrolidinium. The potential scale is relative to the vacuum level. 95% confidence intervals are shown for each limit[17]

Within the last decade, many applications have been reported wherein ionic liquids have been used in place of traditional solvents.[6, 18-20] Methods using ILs as solvents in headspace chromatography have been described, where it was found

that ILs were able to be used in place of traditional solvents in headspace gas chromatography.[21] In addition to this, there has been investigation into the use of ionic liquids as solvents in extraction, where the nonvolatility of ionic liquids may be advantageous in large-scale processes, and also where RTILs may be viable replacements of volatile organic solvents in liquid-liquid extraction processes.[6] It is also possible to exploit the simple variation of ionic liquid properties, through anion and cation selection, to create new liquid-liquid extraction systems.[6]

In many applications, solvent polarity is a critical property. As with most other solvents, polarities of ionic liquids are able to be determined through the use of dye molecules, with many studies concerning the optical properties of dye molecules in differing solvents having been performed.[11, 22-25] An example of a dye molecule which is highly sensitive to solvent polarity is the solvatochromic Reichardt's dye.[25, 26]

1.2 Reichardt's Dye and Solvatochromism

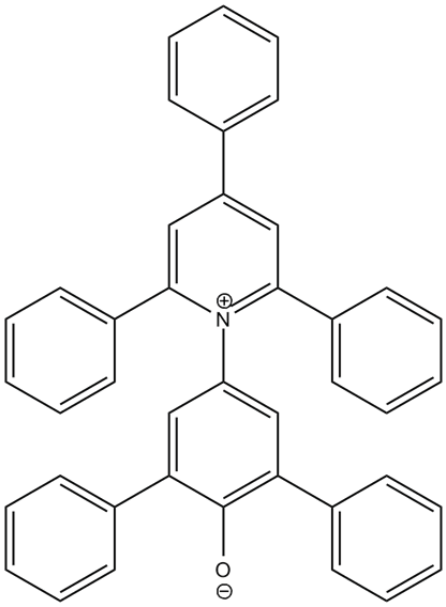


Figure 1.3 - Reichardt's dye

Solvatochromic substances change colour in solvents of differing polarity. Reichardt's dye (2,6-diphenyl-4-(2,4,6-triphenylpyridinium-1-yl)phenolate), shown in Figure 1.3, has a large negative solvatochromism. Figure 1.4 shows that as solvent polarity increases, the ground-state becomes more stabilized by solvation than the excited state, which results in the long-wavelength

solvatochromic, intramolecular CT absorption band being blue-shifted from λ_{max} = 810nm in diphenyl ether (the least polar solvent in which Reichardt's dye is adequately soluble) to λ_{max} = 453nm in water (the most polar solvent in which Reichardt's dye is just soluble).[25]

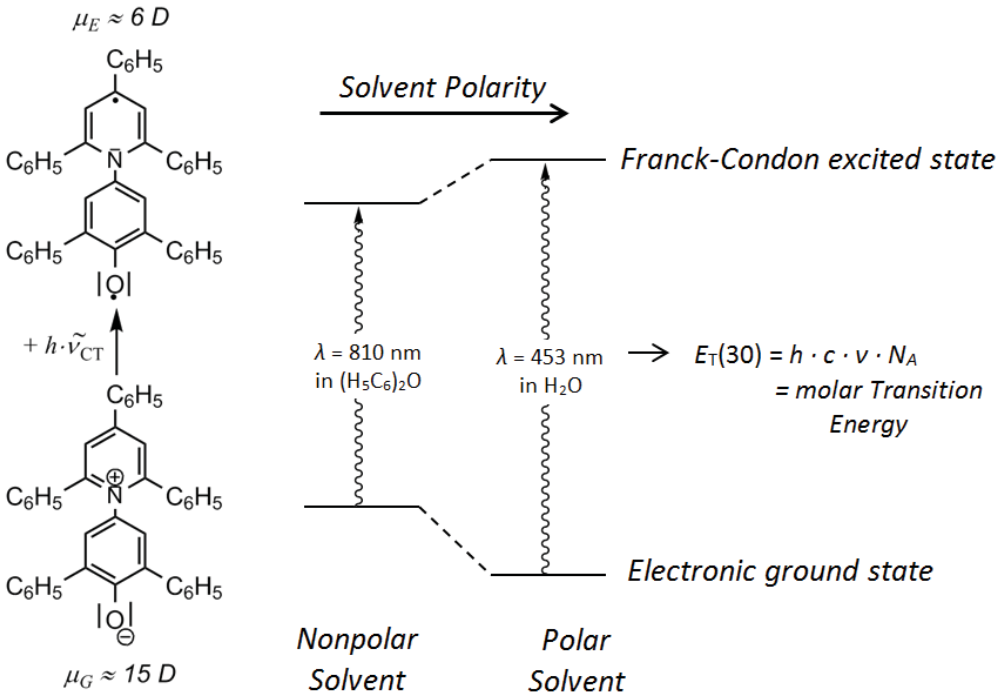


Figure 1.4 - the influence of solvent choice on the electronic structure and intramolecular charge-transfer visible absorption of Reichardt's dye[25]

As this solvatochromic band lies within the visible region of the spectrum, a visual estimate is able to give a fair indication of the polarity of the solvent, whilst absorption measurements can be used to give a relative scale of solvent polarities (known as the $E_T(30)$ scale).[25]

From Figure 1.5 it can be seen that it is possible to make a visual estimate of solvent polarity simply by observing the colour of a solution containing Reichardt's dye. With increasing solvent polarity (from dichloromethane to dimethylsulfoxide to acetonitrile to ethanol to methanol) there is a visible change in the solution colour. The absorption maxima of each of these solutions have also been included, and show that there is also a change in the absorption.



Figure 1.5 - Reichardt's dye in a selection of common solvents; from left to right: ethanol (551nm); methanol (515nm); dichloromethane (703nm); dimethylsulfoxide (633nm); acetonitrile (623nm)

Figure 1.6 shows how Reichardt's dye is able to be used to determine the impact of anion and cation selection on the polarity of ionic liquids. By comparing both the colours and absorption maxima of the samples, it can be seen there are significant differences between the samples. Through visual comparison with the samples in Figure 1.5, it is possible to make initial comparisons between the ionic liquids and common molecular solvents, for example, it appears that BMIM TFSA (Figure 1.6(c)) has similar solvent properties to ethanol (Figure 1.5(d)).



Figure 1.6 - Reichardt's dye in a selection of ionic liquids; from left to right: BMIM TFSA (550nm); BMPY TFSA (490nm); BMIM PF_6 (545nm); BMIM OAc (568nm); BMMIM TFSA (549nm)

1.3 The $E_T(30)$ solvent polarity scale

The solvatochromic absorption of Reichardt's dye has been used to define a solvent polarity scale known as the $E_T(30)$ scale.[25, 27] A solvent's $E_T(30)$ value is defined as the molar transition energies (in kcal mol^{-1}; 1 kcal = 4.184 kJ) of the dye

measured in solvents of differing polarities at room temperature (298K) and normal pressure (1 bar) according to the following equation:

$$E_T(30) = hc\tilde{\nu}_{max}N_A$$

where $\tilde{\nu}_{max}$ is the wavenumber of the maximum of the long-wavelength, solvatochromic, intramolecular CT absorption, and h, c, and N_A are Planck's constant, the speed of light, and Avogadro's constant, respectively. With respect to Figure 1.4, high $E_T(30)$ values correspond to high solvent polarity. As Reichardt's dye is not soluble in nonpolar solvents, such as aliphatic hydrocarbons and tetramethylsilane (TMS) it is not possible to determine their values directly, in which case a similar betaine dye was able to be used as a secondary probe dye. As the two betaine dyes are very well linearly correlated, this allows the calculation of $E_T(30)$ values for solvents in which Reichardt's dye is not soluble. A dimensionless, normalized $E_T(30)$ scale was introduced in 1983, so as to avoid the use of non-SI units. This normalized $E_T(30)$ scale defines water as having a E_T^N value of 1.00, and TMS (which is the least polar solvent that has been measured) as having a E_T^N value of 0.00. The normalized values are able to be calculated using the following equation:

$$E_T^N = \frac{[E_T(solvent) - E_T(TMS)]}{[E_T(water) - E_T(TMS)]} = \frac{[E_T(solvent) - 30.7]}{32.4}$$

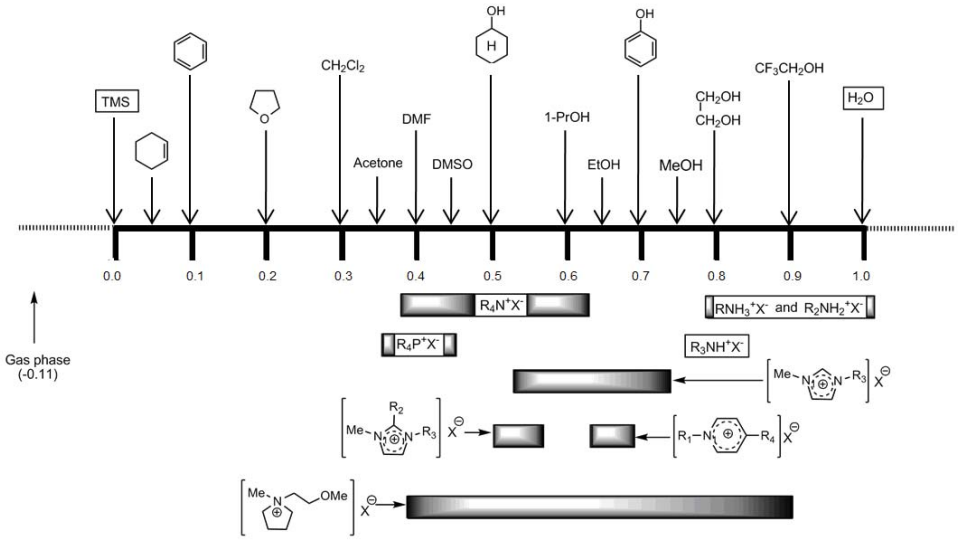


Figure 1.7 - Normalized $E_T(30)$ scale for a range of common molecular solvents (above line) and ionic liquids (below line)[25]

Whilst $E_T(30)$ and E_T^N values are known for more than 350 solvents, and for many binary and ternary solvent mixtures, a graphical representation of the E_T^N scale is shown in Figure 1.7 with a selection of fourteen common molecular solvents and a selection of ionic liquids.

Of great interest, particularly for electrochemical and electron transfer processes, is the ability to make an analogue of the polarity scale for reorganization energy which has been obtained through Raman spectroscopy. Whilst many Raman studies of Reichardt's dye in common organic solvents have been performed,[28-31] there have not been any significant studies comparing across ranges of ionic liquids and common organic solvents. Reichardt's dye has also been found to be thermochromic, meaning that its absorption changes as a function of temperature. Because of this, measurements of absorption and Raman spectra need to be undertaken at approximately the same temperature so as to minimise any effects due to temperature.[32-34]

1.4 Aims of the Thesis

Reorganization energy is able to be related to the solvent dielectric function of simple solvents. Previous studies suggest that this relationship also holds for bulk RTILs.[35-37] It is known that Raman intensities, particularly resonance Raman intensities, are determined in part by the reorganization energy of the solvent. This has been demonstrated experimentally for simple solvents,[38, 39] but resonance Raman has not been used to systematically examine solvent reorganization.

Although simple expressions exist to determine solvent reorganization from dielectric properties, these expressions only apply to limited situations, for example in bulk solvents. Experimental measures of reorganization are more elusive, with a wide range of values being reported by different methods. Specific examples of studies which have been performed previously are given in Chapter 4, Section 3.6.

In this work, resonance Raman spectroscopy will be used to establish an experimental scale of reorganization energy for simple organic solvents and ionic liquids. Given the experimental versatility of Raman spectroscopy and microscopy,

a demonstration that Raman spectroscopy can be used to determine reorganization energy will potentially only provide a more versatile, and hopefully, accurate experimental measure of reorganization energy.

1.5 Reorganization Energy

The concept of reorganization energy originated from Marcus theory. In 1956 Marcus hypothesised that an activation energy diagram of potential surfaces (as shown in Figure 1.8) would be analogous to electron transfer.

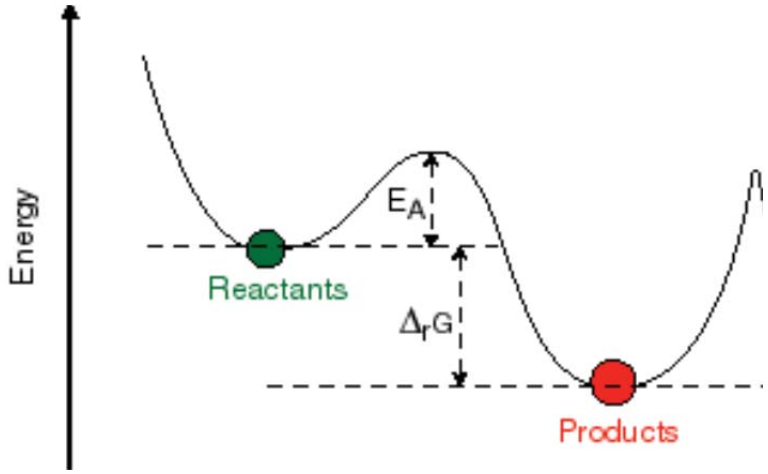


Figure 1.8 - Activation Energy diagram for Potential Surfaces[40]

By taking this diagram literally and drawing two intersecting parabolas, representing the energies of the reactant and product as the nuclei moved around, he obtained a relationship between the two states. This relationship is analogous to the nuclei being connected by springs to each other (as for Hooke's Law). In this case, the energy is dependent on the distance of the springs, whether they are extended or compressed, from their equilibrium positions. Due to the charge on atoms or molecules involved changing during electron transfer, the reactant and product have different equilibrium nuclear positions.

Figure 1.9 shows the concept of reorganization energy. ΔG_{rxn} is the free energy of the reaction, whilst $\Delta G^{\ddagger}$ is the free energy of activation. λ_S and λ_I represents the solvent (external) and internal (or intrinsic) reorganization energies respectively, and sum to give λ.[41, 42] The relative values of λ_S and λ_I depend on the system and solvent. The solvent reorganization energy is the energy required for solvent

molecules to rearrange themselves around solute molecules following a charge transfer process.

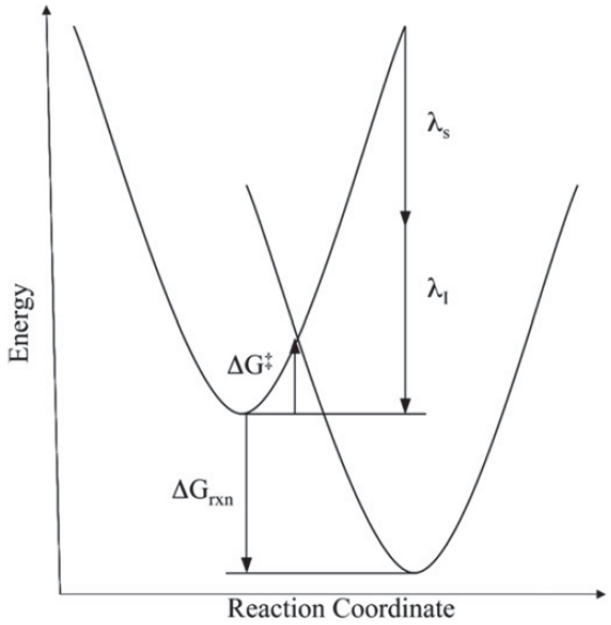


Figure 1.9 – Marcus Theory Diagram showing reorganization parameters[42]

Via Marcus theory, reorganization energy is directly applicable to applications involving electron transfer. The reorganization energy is able to be used to determine the rate of electron-transfer processes. The rate is given by the following equation:[42]

$$k_{ET} = \frac{V_{AB}^2}{h\sqrt{4\pi\lambda kT}}\ exp\left[\frac{-(\Delta G_{rxn} + \lambda)^2}{4\lambda kT}\right]$$

where λ is the total reorganization energy as stated above, and V_{AB} is the electronic overlap integral.[43] The internal reorganization energies are able to be obtained by taking a product's wavefunction and calculating the single point energy at the optimized geometry of the reactants,[42] whilst the solvent component is calculated using the Marcus solvent formula[41] which is shown in the form in which it is used for this study in Chapter 4, Section 3.6.

Reorganization energy is able to be decomposed into its contributions from the reacting molecules, the so called "internal" reorganization, and from the environment, the "solvent" reorganization.[44] Internal reorganization energy is able to be further reduced into contributions from individual vibrations, or "mode-

specific" reorganization energies. Reorganization energies were traditionally thought of as being difficult to obtain, be it experimentally or theoretically, however, when the reactant and product states are connected through an optical or electronic transition, resonance Raman intensities are able to be used to give a complete set of mode-specific reorganization energies.[44]

1.6 Homogeneous Broadening and Reorganization Energy

Chapter 2 will describe how broadening processes affect resonance Raman intensities. It is the close physical connection between the processes of broadening in optical spectroscopy and reorganization in charge-transfer processes that allow resonance Raman to be used as a probe of reorganization energy in RTILs.

The energy levels of molecules are influenced by the surrounding environment, such as a solvent for liquids, or lattices for solids. This influence of environment leads to a so-called "broadening". Generally, spectroscopic techniques make measurements over an ensemble of molecules, leading to scattered or absorbed, photons being collected from molecules in a distribution of sites, and thus a distribution of energies. In order to determine what these distributions are, statistical methods are able to be used. The distributions are characterised by two parameters; the time-scale, and magnitude, of the fluctuations. These time-scales are relative to the time period of the underlying quantum mechanical transition, and the period of the transitions is given in the inverse frequency of the transition, therefore, spectrally broad electronic transitions have very fast time-scales.

There are two ideal limiting cases which can occur using the time-scale, one case where fluctuations occur much more rapidly than the time-scale of the transition, and the other extreme case where fluctuations are essentially frozen on the time-scale of the transition. The first of these cases, each molecule will sample the full distribution of sites, and the centre and width of the distribution are sufficient to describe the broadening for all molecules. Because of this, these centre and width parameters are identical for every homogeneous molecule, and very rapid fluctuations lead to homogeneous broadening of molecular energy levels.

1.7 Inhomogeneous Broadening

In Section 1.6, broadening was described in terms of time-scale of fluctuations and transitions. Whilst homogeneous broadening, as its name suggests, is caused by each molecule experiencing the same fluctuations, and having the same parameters, inhomogeneous broadening occurs when each molecule is being affected in different ways.

Both inhomogeneous and homogeneous broadenings contribute to the width of the absorption spectrum. Reorganization energy is related only to the homogeneous broadening, however, and not inhomogeneous broadening. This means that absorption spectroscopy is not able to be used to extract reorganization energies. Absorption spectroscopy, however, is able to be used simultaneously with resonance Raman spectroscopy in order to extract these reorganization energies (see Chapter 2 and Section 3.4 for more details).

The absorption spectral width is a convolution of homogeneous, inhomogeneous, and vibronic broadening mechanisms. This means that whilst absorption spectra can be used to determine the overall effect of these contributions, they are unable to be used to determine the effect of any of these individual parameters. Resonance Raman intensities, however, are determined only by homogeneous broadening. The simultaneous modelling of absorption and Raman spectra allows the various broadening components of the spectra to be deconvoluted.

1.8 Computational studies of Reichardt's Dye

Computational studies of Reichardt's Dye and similar molecules have been performed in the past; however, the structure of Reichardt's dye makes computational studies difficult, namely due to the large number of atoms in the structure.[33, 38, 45-48] Another structural property which has a significant effect on calculations is the presence of two delocalised ring systems, namely the pyridinium ring and phenoxide ring. Electron correlation between these rings can cause changes in the structure of the solute molecule, which in turn changes the relative geometries of the rings.[47] In a range of studies, computational studies have been successful in determining and explaining many properties of Reichardt's Dye.

The methods used for these included HF/6-31G**[33], B3LYP[33, 38, 45], 6-311G**[38], RISM-SCF[47, 48], and CASSCF[48]. These studies have all produced good results, and these methods have been found to be useful for the study of Reichardt's dye.

Computational studies have also been performed using the Reichardt's and other dye molecules to find information about the properties of ionic liquids.[35, 37, 49, 50] Maroncelli et al[35] studied the solvation response of coumarin 153 in a range of RTILs, and found that predicted dynamics were faster than those both observed experimentally and obtained via molecular dynamics. It has been found that ionic liquids behave, with respect to their effect on electron-transfer reactions, as slow-moving versions of conventional solvents having high polarity.[50] It has also been found that for low-barrier adiabatic processes, there does not appear to be any significant distinction between solvation in dipolar or ionic environments, however, this situation may be different in the case of reactions with higher barriers.[50] The details of the computational studies performed in this work are described in Chapter 3, Section 5.

1.9 Summary

Chapter 2 will provide an overview of the theory of Raman intensities. This will include information on the classical and quantum mechanical models of Raman intensities, as well as details on resonance Raman, the time-domain picture, and solvent broadening models.

Chapter 3 provides an overview of the experimental procedures of this work. It includes information on the synthesis of ionic liquids, as well as information on collection and analysis of resonance Raman spectra, and more details on the computational studies performed.

Chapter 4 includes the results of the studies performed on common organic solvents. This includes absorption spectra obtained, results of computational studies, and the results of the modelling of Raman profiles for the solvents studied. The results of similar studies to these performed on ionic liquids, excepting computational studies, are reported in Chapter 5.

Chapter 2 - The Theory of Raman Intensities

2.1 The Classical Model

The classical theory of Raman scattering allows for the quantitative treatment of light scattering, in particular the frequency dependence, directional and polarization properties, and some aspects of the selection rules.[51] Briefly, Raman (and Rayleigh) scattering occurs via the generation of an induced dipole. This dipole radiates the scattered light, and is induced by application of an electric field via a radiation field. The polarizability of the dipole determines how the incident field is transformed into the scattered field. The linear induced dipole $\boldsymbol{P}^{(1)}$ is given by the following equation:

$$\boldsymbol{P}^{(1)} = \boldsymbol{P}^{(1)}(\omega_0) + \boldsymbol{P}^{(1)}(\omega_0 - \omega_k) + \boldsymbol{P}^{(1)}(\omega_0 + \omega_k) \tag{2.1}$$

where:

$$\boldsymbol{P}^{(1)}(\omega_0) = \boldsymbol{P}_0^{(1)}(\omega_0)\{\cos \omega_0 t\} \tag{2.2}$$

$$\text{with: } \boldsymbol{P}_0^{(1)}(\omega_0) = \boldsymbol{\alpha}_0 \cdot \boldsymbol{E}_0 \tag{2.3}$$

$$\boldsymbol{P}^{(1)}(\omega_0 - \omega_k) = \boldsymbol{P}^{(1)}(\omega_0 - \omega_k)\{\cos(\omega_0 - \omega_k)t - \delta_k\} \tag{2.4}$$

$$\text{with: } \boldsymbol{P}_0^{(1)}(\omega_0 - \omega_k) = \frac{1}{2} Q_{k_0} \boldsymbol{\alpha'}_{\mathrm{k}} \cdot \boldsymbol{E}_0 \tag{2.5}$$

$$\text{and } \boldsymbol{P}^{(1)}(\omega_0 + \omega_k) = \boldsymbol{P}^{(1)}(\omega_0 + \omega_k)\{\cos(\omega_0 + \omega_k)t + \delta_k\} \tag{2.6}$$

$$\text{with: } \boldsymbol{P}_0^{(1)}(\omega_0 + \omega_k) = \frac{1}{2} Q_k \boldsymbol{\alpha'}_{\mathrm{k}} \cdot \boldsymbol{E}_0 \tag{2.7}$$

The term $\cos \omega_0 t$ in 2.2 enters from the radiation field. It can be seen that there are three distinct frequency components contributing to the linear induced dipole. The first of these is $\boldsymbol{P}_0^{(1)}(\omega_0)$, which gives rise to radiation at ω_0, and accounts for Rayleigh scattering. $\boldsymbol{P}_0^{(1)}(\omega_0 - \omega_k)$ gives rise to radiation at $\omega_0 - \omega_k$, and accounts for Stokes Raman scattering, whereas $\boldsymbol{P}_0^{(1)}(\omega_0 + \omega_k)$ gives rise to radiation at $\omega_0 + \omega_k$, accounting for anti-Stokes Raman scattering. Stokes and anti-Stokes Raman scattering will be described shortly. Note that the induced dipole $\boldsymbol{P}_0^{(1)}(\omega_0)$

has the same phase as that of the incident field, however, $\boldsymbol{P}_0^{(1)}(\omega_0 \pm \omega_k)$ are shifted in phase by an amount $\pm\delta_k$ relative to the incident field. This shift defines the phase of the normal vibration Q_k relative to the field, and is different for different molecules.

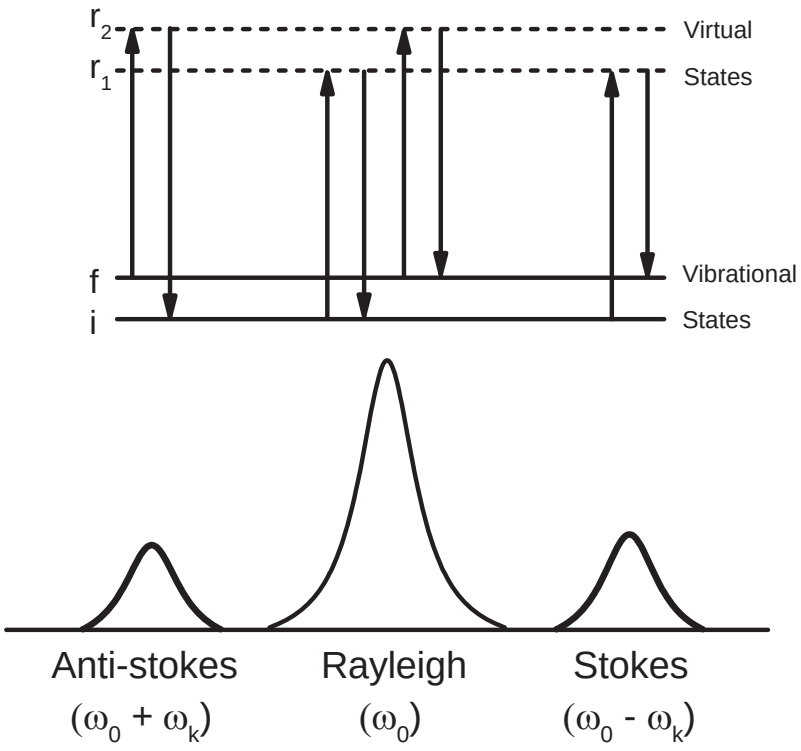


Figure 2.1 - Stokes, Rayleigh, and anti-Stokes scattering

Rayleigh, Stokes, and anti-Stokes scattering are able to be described with the aid of Figure 2.1. States *i* and *j* are vibrational states, whilst r_n are virtual states, for which it is not known which state the scattered photon enters. For Rayleigh scattering, there is no resultant change in the energy state of the system, however, scattering still occurs, with an incident photon being annihilated and a photon of the same energy being created simultaneously, leading to a scattering of radiation of unchanged wavenumber, ω_0, occurs.[51] Stokes scattering occurs when the material absorbs energy, and the emitted photon has a lower energy than the absorbed photon, as shown on the right of Figure 2.1. Anti-Stokes scattering occurs when the material experiences an overall loss of energy, and the emitted photon has a higher energy than the absorbed photon, as can be seen in Figure 2.1. A Raman spectrum, which may also include the Rayleigh peak, gives information on the scattered photons, and shows the intensity of scattered light as a function of

frequency relative to the incident photons. Raman bands are not characterised by absolute wavenumbers, but by the magnitude of the shift of wavenumber $\Delta\omega$ from the incident wavenumber.[51] This wavenumber shift can be defined as being positive for Stokes scattering and negative for anti-Stokes scattering. Stokes Raman scattering is most commonly studied, as the intensity of anti-Stokes scattering relative to Stokes scattering decreases rapidly with increasing $\Delta\omega$, as the anti-Stokes has an additional $e^{-h\Delta\omega/kT}$ term.

Stokes and anti-Stokes scattering depend on the derived polarizability, α'_k, which occurs in the frequency components $\boldsymbol{P}_0^{(1)}(\omega_0 - \omega_k)$ and $\boldsymbol{P}_0^{(1)}(\omega_0 + \omega_k)$, as shown in Equations 2.5 and 2.6. From selection rules for fundamental vibrations[51] it is known that the polarizability must change with changing bond length.

2.2 The Quantum Mechanical Model

From quantum theory, radiation is emitted or absorbed as a result of transitions between two discrete energy levels. In addition to this, the radiation itself is quantized with the energy in discrete photons. For Raman scattering, however, the radiation is treated classically and is considered as the source of a perturbation of the molecular system which is treated quantum mechanically.[51] This leads to transitions between energy levels taking place with emission or absorption of radiation, given the transition moment associated with the initial and final states is non-zero.

Many of the concepts from the classical model can be transferred to the quantum mechanical model. For a Raman transition between two states $|i\rangle$ and $|f\rangle$ of a scattering system, the intensity of light scattered at 90° to the direction of irradiation is given by the following equation:[52]

$$I_{fi}(\pi/2) = \frac{\pi^2}{\varepsilon_0^2}\left(\tilde{\omega}_0 \pm \tilde{\omega}_{fi}\right)^4 \mathcal{I}_0 \sum_{\rho,\sigma}\left[\alpha_{\rho\sigma}\right]_{fi}\left[\alpha_{\rho\sigma}\right]_{fi}^* \qquad (2.8)$$

where $\mathcal{I}_0$ is the irradiance of the incident radiation, $\tilde{\omega}_0$ and $\tilde{\omega}_{fi}$ are the wave numbers of the exciting line and the Raman transition $|f\rangle \leftarrow |i\rangle$ respectively, ε_0 is the permittivity of free space, and $\left[\alpha_{\rho\sigma}\right]_{fi}$ the ρth element of the transition polarizability tensor. For vibrational Raman scattering excited far from resonance,

the tensor α is symmetric, i.e. $\alpha_{\rho\sigma} = \alpha_{\sigma\rho}$ however, it may become asymmetric for electronic and resonance Raman scattering.[52] $[\alpha_{\rho\sigma}]_{fi}$ is given by:

$$[\alpha_{\rho\sigma}]_{fi} = \frac{1}{hc}\sum_r \left\{ \frac{[\mu_\rho]_{fr}[\mu_\sigma]_{ri}}{\tilde{\omega}_{ri} - \tilde{\omega}_0 + i\Gamma_r} + \frac{[\mu_\sigma]_{fr}[\mu_\rho]_{ri}}{\tilde{\omega}_{ri} + \tilde{\omega}_0 + i\Gamma_r} \right\} \tag{2.9}$$

The adiabatic Born-Oppenheimer approximation, in which vibronic states are formed by products of the pure vibrational and the pure electronic states, is able to be used.[52] These vibronic states, labelled $|i\rangle$, $|f\rangle$, and $|r\rangle$, are able to be written in the form:

$$\begin{aligned} |i\rangle &= |gm\rangle = |g\rangle|m\rangle \\ |f\rangle &= |gn\rangle = |g\rangle|n\rangle \\ |r\rangle &= |ev\rangle = |e\rangle|v\rangle \end{aligned} \tag{2.10}$$

where $|e\rangle$ represents an excited electronic state, and $|m\rangle$, $|n\rangle$, and $|v\rangle$ represent vibrational states of the scattering species. This enables the transition polarizability to be rewritten in the form:

$$[\alpha_{\rho\sigma}]_{gn,gm} = \frac{1}{hc}\sum_{ev} \left\{ \frac{\langle n|[\mu_\rho]_{ge}|v\rangle\langle v|[\mu_\sigma]_{eg}|m\rangle}{\tilde{\omega}_{ev,gn} - \tilde{\omega}_0 + i\Gamma_{ev}} + \frac{\langle n|[\mu_\sigma]_{ge}|v\rangle\langle v|[\mu_\rho]_{eg}|m\rangle}{\tilde{\omega}_{ev,gn} + \tilde{\omega}_0 + i\Gamma_{ev}} \right\} \tag{2.11}$$

where $[\mu_\rho]_{ge}$ is the pure electronic moment associated with the transition $|g\rangle \leftarrow |e\rangle$, which has been separated from vibrational components of the transition $|n\rangle \leftarrow |v\rangle$. Under the conditions for which the Born-Oppenheimer approximation is valid, the dependence of an electronic transition moment, such as that associated with the transition between the ground and excited states, on the k normal coordinates of the system, (Q_k) is small. This enables $[\mu_\rho]_{ge}$ to be expressed as a rapidly converging Taylor series expanded around the equilibrium position, such that:[52]

$$[\mu_\rho]_{ge} = [\mu_\rho]^0_{ge} + \sum_k [\mu_\rho]'_{ge} Q_k + \cdots \tag{2.12}$$

where $[\mu_\rho]'_{ge} = \partial[\mu_\rho]_{ge}/\partial Q_k$. This leads to non-Condon effects, i.e. dependence of electronic transition on molecular geometry, in which position and momentum are not conserved.

In addition to this, a second simplification arises from the Born-Oppenheimer approximation, in that the electronic and vibrational parts of the integrals in Equation 2.11 can be separated, such that:

$$\left\langle n\left|[\mu_\rho]_{ge}\right|v\right\rangle = [\mu_\rho]^0_{ge}\langle n|v\rangle + \sum_k [\mu_\rho]'_{ge}\langle n|Q_k|v\rangle \tag{2.13}$$

There are further approximations which are also able to be made, which are described in detail by Clark and Dines[52], and as such will not be included here. Using the approximations, the transition polarizability is able to be written as follows:

$$\begin{aligned}[\alpha_{\rho\sigma}]_{gn,gm} &= \frac{1}{hc}\sum_e \frac{2\tilde{\omega}_e}{(\tilde{\omega}_e^2-\tilde{\omega}_0^2)}[\mu_\rho]^0_{ge}[\mu_\sigma]^0_{eg}\langle n|m\rangle \\ &+ \frac{1}{hc}\sum_e\sum_k \frac{2\tilde{\omega}_e}{(\tilde{\omega}_e^2-\tilde{\omega}_0^2)}\left\{[\mu_\rho]'_{ge}[\mu_\sigma]^0_{eg} + [\mu_\rho]^0_{ge}[\mu_\sigma]'_{eg}\right\}\langle n|Q_k|m\rangle \\ &+ \frac{1}{hc}\sum_e\sum_{k,k'} \frac{2\tilde{\omega}_e}{(\tilde{\omega}_e^2-\tilde{\omega}_0^2)}[\mu_\rho]'_{ge}[\mu_\sigma]'_{eg}\langle n|Q_k Q_{k'}|m\rangle \end{aligned} \tag{2.14}$$

Briefly, the first term in Equation 2.14 contributes only to Rayleigh scattering, whilst the second term is responsible for both the Stokes and anti-Stokes Raman scattering for vibrational fundamentals. The third term gives rise to first overtones ($k = k'$) and combination bonds ($k \neq k'$), however this is usually very small and the attributed bands are very weak in normal Raman scattering. For more details on this equation, see Clark and Dines[52].

Resonance Raman scattering occurs when the incident laser frequency, $\tilde{\omega}_0$, and the transition frequency of the scattered photon, $\tilde{\omega}_{ev,gm}$, are very close. This leads to simplification of the transition polarizability being made possible for excitation under resonance conditions.[52] As these two frequencies become close, the relevant excited state will dominate the sum over states. As such, it is possible to consider only one, or at most two, electronic manifolds, and also to neglect the

non-resonant part of the transition polarizability at resonance. This means, that for resonance Raman, Equation 2.11 is able to be rewritten in as a sum of four contributions, such that:

$$\left[\alpha_{\rho\sigma}\right]_{gn,gm} = A + B + C + D \tag{2.15}$$

where:

$$A = \frac{1}{hc}\left[\mu_\rho\right]_{ge}^{0}\left[\mu_\sigma\right]_{eg}^{0}\sum_v \frac{\langle n_g|v_e\rangle\langle v_e|m_g\rangle}{\widetilde{\omega}_{ev,gm}-\widetilde{\omega}_0+i\Gamma_{ev}} \tag{2.16}$$

The full B, C, and D terms are not as significant as the A term for the conditions used in this work, that is, a single, strongly allowed electronic transition, such as the CT transition in Reichardt's Dye. Refer to Clark and Dines[52] for the full forms of B, C, and D, as well as for full explanations of each terms contribution to the transition polarizability. In order to clearly explain the time-domain picture, as described in 2.3, it is useful to re-write the A-term in a different form. The A-term is able to be re-written as follows:[53]

$$\alpha_{i\to f}(E_L) = \frac{M^2}{hc}\sum_v \frac{\langle f|v\rangle\langle v|i\rangle}{\omega_v-\omega_i-\widetilde{\omega}_0-i\Gamma} \tag{2.17}$$

where $|n_g\rangle$ has been replaced by $|f\rangle$; $|v_e\rangle$ has been replaced by $|v\rangle$; and $|m_g\rangle$ has been replaced by $|i\rangle$. ω_v and ω_i are the frequencies of the vibrational states $|v\rangle$ and $|i\rangle$ respectively, whilst $\widetilde{\omega}_0$ is the incident photon frequency. M is the electronic transition length matrix element. This is the form of the Albrecht A-term expression for excitation within an allowed absorption band.[53] From this, the complete expression for the resonance Raman cross-section is found to be:

$$\sigma_{i\to f} = \frac{5.87\times10^{-19}M^4E_S^3E_L}{hc}\left|\sum_v \frac{\langle f|v\rangle\langle v|i\rangle}{\omega_v-\omega_i-\widetilde{\omega}_0-i\Gamma}\right|^2 \tag{2.18}$$

E_S and E_L are shown in Figure 2.2 in the next section. A more detailed explanation can be found in Myers and Mathies[53].

2.3 The Time-Domain Picture

Many features of resonance Raman scattering are easier to visualise in a time-dependent picture than in the equivalent sum-over states picture. In addition to this, a time-dependent approach to analysing Raman data gives a useful framework for calculating absorption spectra and Raman intensities, and simplifies the calculation of spectra.[53]

Alternate expressions for resonance Raman parameters can now be derived easily from a sum-over-states formula, shown here as equation 2.18. Alternatively, time-domain expressions can now be found from time-dependent perturbation theory.[53] In addition to this, it has been shown that summing over a set of states having specific phase factors is equivalent to summing over a series of time-dependent wave packets.[54, 55] From this, the A term shown in Equation 2.17, is able to be rewritten in an equivalent manner by inserting a complete set of vibrational states of the electronic state of interest, and integrating over time.[56] The time-dependent form of the A term is given by:

$$\alpha_{i\to f} = \frac{i}{\hbar}\int_0^\infty \langle f|i(t)\rangle \exp[i(\omega_L + \omega_i)t] e^{-\Gamma t/\hbar}\, dt \qquad (2.19)$$

where ω_L is the frequency associated with E_L in Figure 2.2. For a more detailed derivation of Equation 2.19, see Myers and Mathies[53]. From this new form of the A term, the resonance Raman cross-section is now able to be written as:

$$\sigma_{i\to f} = \frac{8\pi E_S^3 E_L e^4 M^4}{9\hbar^6 c^4}\left|\int_0^\infty \langle f|i(t)\rangle \exp[i(\omega_L + \omega_i)t] e^{-\Gamma t/\hbar}\, dt\right|^2 \qquad (2.20)$$

When the constants are evaluated, the prefactor in this equation becomes $2.08 \times 10^{-20} M^4 E_S^3 E_L$, with all units as for Equation 2.18, and the time integral being carried out in units of picoseconds.[53]

The previous equations are able to be explained better with the aid of Figure 2.2. The incident photon interacts with the electronic transition moment, sending the initial vibrational state $|i\rangle$ to the excited electronic surface, where it is propagated by the excited-state vibrational Hamiltonian.

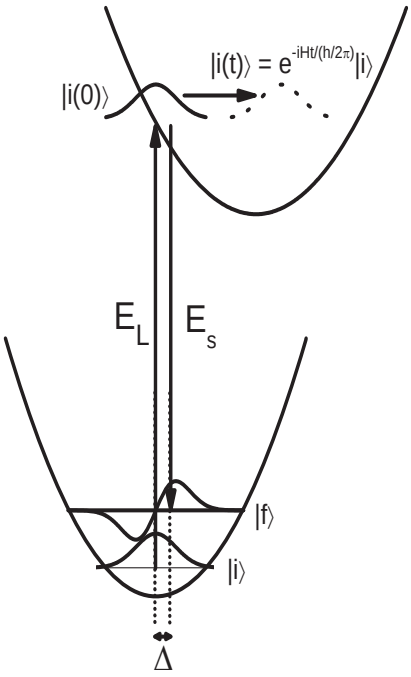


Figure 2.2 - The time-dependent picture

Changes in nuclear geometry determine the intensity of the Raman transitions for each active mode. These changes are denoted as Δ, and shown in Figure 2.2. The Raman cross-section as a function of incident photon energy is given by the square of the half Fourier transform of the overlap between $|i(t)\rangle$ and the final vibrational level $|f\rangle$.[53] This relationship is shown in Figure 2.3. The Raman overlap is zero at t = 0, however, it increases rapidly to a maximum as $|i(t)\rangle$ moves enough to overlap with one lobe of $|f\rangle$, as shown by point A in Figure 2.3. The overlap then decreases as $|i(t)\rangle$ moves far away from $|f\rangle$ as shown by B, then increases to another maximum at C. The overlap finally goes to zero at the end of a full cycle, where $|i(t)\rangle$ and $|f\rangle$ are orthogonal to each other once again.[53]

The time dependence of $\langle f|i(t)\rangle$ determines the shape of the Raman excitation profile, whilst the intensity of the Raman scattering depends on the integrated area of $\langle f|i(t)\rangle$. If there is not significant displacement of the ground and excited states, there will not be sufficient overlap with any final state, and as such the resonance Raman intensity will be low. This means that the only vibrations which can be strongly A-term enhanced are those for which there is significant distortion upon electronic excitation.[53] This is analogous to the result from the sum-over-states approach.

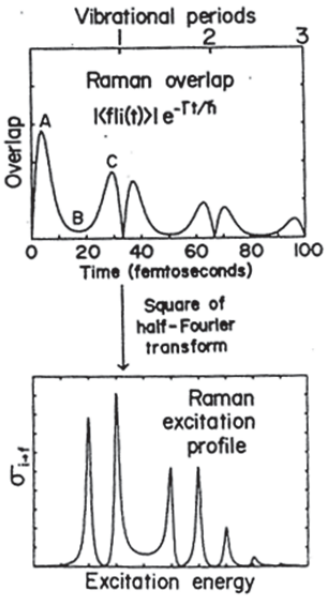


Figure 2.3 - Raman cross-section[53]

With the sum-over-states, resonance Raman intensities are found to depend on the excited-state potential surface via the vibrational eigenstates of that surface, whereas in the time-dependent picture, the excited-state potential surface determines the evolution of the vibrational wavefunction during the time between the disappearance of the incident photon and creation of the scattered photon directly, see equations 2.16 and 2.17. The Franck-Condon factors e.g. $\langle f|v\rangle$ and $\langle v|i\rangle$ determine the intensity. It is possible to move between the two pictures by either considering a wavepacket to be a superposition of eigenstates (see Equation 2.21), or considering an eigenstate to be a superposition of wavepackets (see Equation 2.22).

$$\Psi(x,t) = \sum_{n=1}^{\infty} a_n \psi_n(x) e^{-\frac{i}{\hbar}E_n t} \tag{2.21}$$

$$\psi_n(x) \propto \int_{-\infty}^{+\infty} \Psi(x,t) e^{-\frac{i}{\hbar}E_n t} dt \tag{2.22}$$

The interchangeability of wavepackets and eigenstates is useful when it comes to practical approaches to modelling Raman intensities. Wavepackets are generated by narrow time-domain pulses, generally on the order of femtoseconds, which are broad in the frequency domain, whereas eigenstates are created by broad time-domain pulses, which are narrow in the frequency domain.

Continuous wave Raman spectroscopy is a dynamic process. Continuous wave excitation is able to be thought of as a continuous train of δ-pulses (δ-pulses generate wavepackets, which undergo dynamics), and from this, continuous wave spectroscopy leads to a train of wavepackets with a fixed relationship (see equation 2.22), i.e. eigenstates. The dynamics involved determine the absorption band profile, and more importantly for this work, resonance Raman intensities. Dephasing of the wavepacket, which leads to reduced intensity, can occur due to solvent interactions. Conveniently, the wavepacket is only completely dephased once it leaves the Franck-Condon region. As resonance Raman reports on the Franck-Condon region only, it can be used to give information on solvent motion. Solvent effects are accounted for in Equation 2.20 by the term $e^{-\Gamma t/\hbar}$, which influences the time-domain profile.

If only times shorter than the fastest excited-state vibrational period make significant contributions to resonance Raman intensity, the scattering is said to be in the "short-time" limit, and many aspects of Raman scattering are simplified.[53] The wavepacket associate with Raman scattering propagates in 3N-6 directions. The movement of the wavepacket has a recurrence time, τ_R, which is the time taken for the wavepacket to travel back to the Franck-Condon region, i.e. its initial position. For a single Raman mode, $\tau_R \propto \frac{1}{\omega}$, however, for multiple modes, the recurrence time becomes very long. As can be seen in Figure 2.4, for a single mode, the Raman overlap, $\langle f|i(t)\rangle$, travels to the Franck-Condon region at small, regular intervals, as there is only one mode contributing to the function.

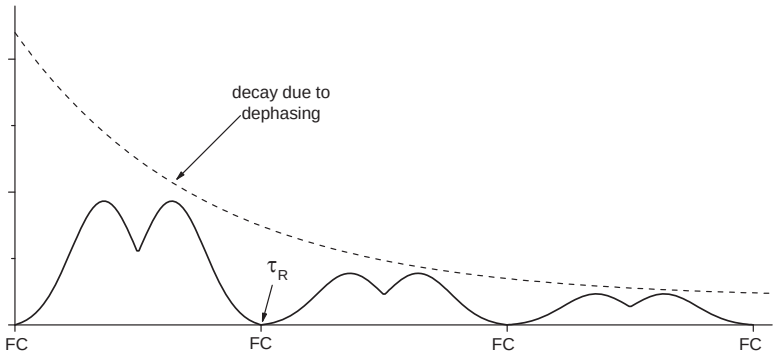


Figure 2.4 – Time-dependent wavepacket overlap function for single vibrational mode

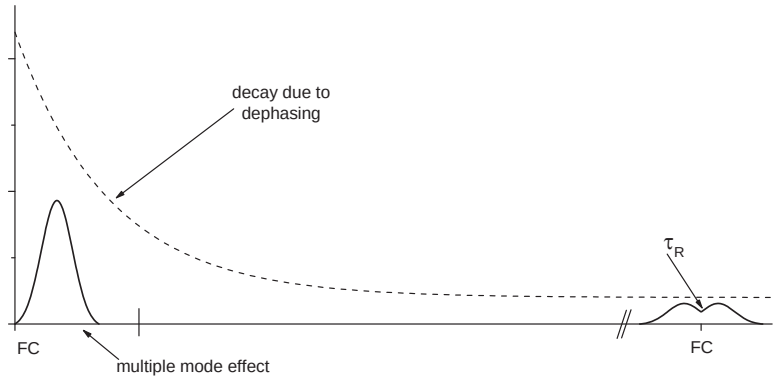


Figure 2.5 – Time-dependent wavepacket overlap function decay due to multi-mode effect

For multiple modes, however, the overlap function is narrow, and is made up of many modes propagating with different frequencies. From this, in order for the wavepacket to return to the Franck-Condon region, each of the modes must have completed an integer number of cycles. As the chances of all modes being in the same position at the same time are very small, this leads to a large τ_R, as shown in Figure 2.5. An alternative way of looking at this is shown in Figure 2.6. The single mode picture shows the mode oscillating within the excited state, whereas the multiple mode picture shows that the wavepacket travels for a short time then essentially dies away. In addition to recurrence time, there are other factors which affect the propagation of the wavepacket, and destroy the overlap. One of the predominant factors which destroys overlap is dephasing interactions due to the solvent. The combination of effects of τ_R and dephasing lead to the wavepacket being essentially destroyed before it is ever able to return to the Franck-Condon region.

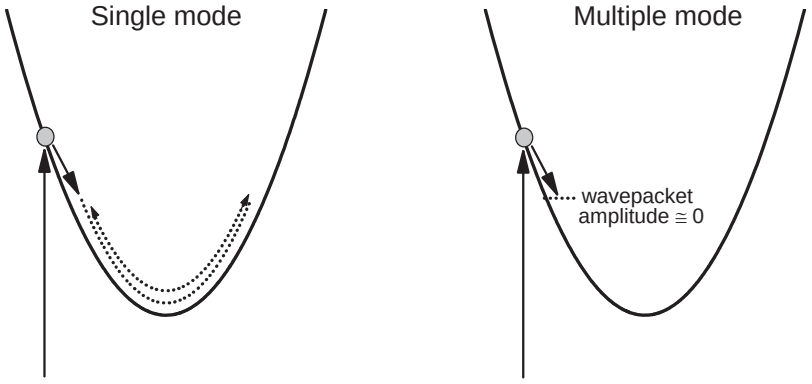


Figure 2.6 – Propagation of wavepacket centre on electronic excited-state surface; wavepacket amplitude decays rapidly for multi-mode case, depicted here by the wavepacket only sampling the Franck-Condon region

The Raman overlap function $\langle f|i(t)\rangle$ only depends on dynamics near the Franck-Condon region, and as such, those which occur at very short times.

2.4 Solvent Broadening Models in Time-Domain Picture

In order to understand the wavepacket dynamics determining Raman intensities, a model describing the distribution of solute energy levels is required. These energy levels can be represented empirically by Gaussian or Lorentzian distributions. The energy and time-domain are able to be related through a Fourier relationship via frequency and Planck's constant. The presence of the $e^{-\Gamma t}$ term in equations 2.19 and 2.20 result from the a Fourier transform of a Lorentzian function giving an exponential function. The use of the Lorentzian function comes about through the frequency domain expressions for transition polarizability shown in Chapter 2, Section 2, having the form of Lorentzian. It is possible to model the effect of the solvent on the time-dependent overlap function by multiplying the overlap function with $e^{-\Gamma t}$, which leads to the damping of the overlap function, and reduces the intensity of the Raman transition. This is due to the components of the wavepacket having different phases and becoming dephased, which leads to homogeneous broadening. This model works well for modelling the effects of the solvent on the solute, and $g(t) = e^{-\Gamma t}$ is the solvent response function in this case.

The effect of the solute on the solvent is also an important factor to account for, especially with respect to electron transfer, as the acquisition or loss of an electron by the solute during electron transfer will cause the surrounding solvent to adjust its structure. The Lorentzian and Gaussian models ignore this effect, and as such, a more sophisticated model is required.

The band shape of a molecule in solution is able to be calculated with the aid of the Brownian oscillator model for the coupling of the solvent motions to electronic transitions of a solute.[57] Figure 2.7 shows the Brownian oscillator model from both the spectroscopic and electron transfer viewpoints. What is occurring in both systems is identical. In electron transfer there are random thermal fluctuations which cause broadening of the electronic levels. The "electron" and "hole" undergo

independent dynamics which leads to dephasing occurring. The magnitude of this dephasing controls the rate of electron transfer.

The use of the Brownian oscillator gives a simple but realistic model for how a large number of solvent modes will collectively affect the vibrational motion of the solvent molecule. By assuming the vibrational mode is a Brownian oscillator, the effect of the solvent is able to be modelled. The Brownian oscillator model is analogous to Brownian motion for the classical trajectory of a particle, whereupon the trajectory is found through solving Newton's equations. The individual forces, however, are too complicated to describe explicitly, and as such, a statistical approach is adopted and the forces acting are assumed to be random. In the Brownian oscillator model, a random Langevin force is generated from Newton's equations, which leads to changes in the line shape function.[57] This Langevin force is given by equation 2.23. This leads to the standard equation of motion for a damped oscillator now including a random force term.

$$\ddot{q}_B + \gamma \dot{q}_B + \omega_B^2 q_B = f(t) \tag{2.23}$$

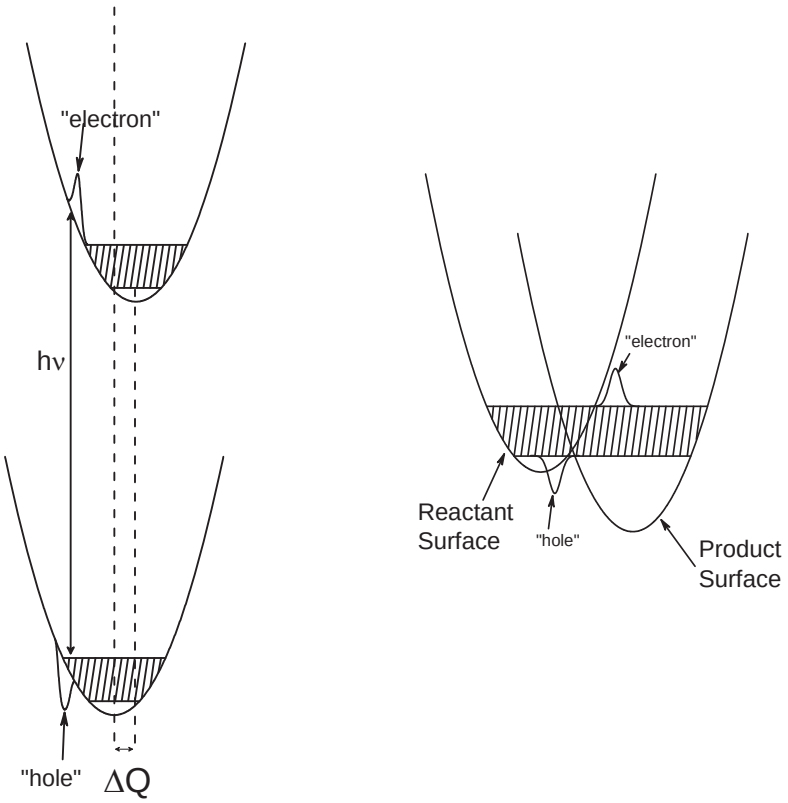


Figure 2.7 - The Brownian oscillator model is able to be applied to resonance Raman modelling; Left: Spectroscopic viewpoint; Right: Electron Transfer viewpoint

Due to the Langevin force, the line shape function, now given by g as opposed to Γ, has imaginary components. The line shape function is now:[57]

$$g(\tau) = (\Delta_S/\Lambda)^2[\Lambda\tau - 1 + e^{-\Lambda\tau}] + i(\lambda_S/\Lambda)[1 - e^{-\Lambda\tau}] \quad (2.24)$$

where Δ_S is the magnitude of the line broadening of the solvent, λ_S is the solvent contribution to the shift of emission due to displacement between the ground and excited electronic state surface, and Λ is the modulation frequency of the solvent oscillator, given by τ_L^{-1} where τ_L is the longitudinal relaxation time of a Debye solvent. The ratio Δ_S/Λ gives the stochastic line shape parameter, R_K, which is important in the modelling of Raman profiles. By neglecting the imaginary term in Equation 2.24, the form of Γ is obtained, however, this results in a purely real damping function which broadens the absorption and emission spectra, but is unable to account for the solvent-induced Stokes shift of the emission spectrum.[57] For a more detailed explanation and derivation of equations, see Mukamel et al.[57]

Chapter 3 – Experimental

3.1 Synthesis and Purification

3.1.1 1-butyl-3-methylimidazolium chloride (BMIM Cl) Synthesis

In synthesising BMIM Cl, the method of Burrell et al[58] was followed at a smaller scale. n-Chlorobutane (250mL) was slowly added to freshly distilled methylimidazole (200mL) in a 1L three-necked round-bottom flask which was fitted with a reflux condenser and a thermometer. This mixture was stirred with a magnetic stirrer at 70°C for four days, during which time a yellow solid formed. This solution was then cooled to room temperature. Any remaining solution was then decanted off before washing the solid with diethyl ether (3 × 100mL) and drying under vacuum for 24 hours. The solid was then dissolved in water (700mL) and decolourizing charcoal (15g) added, before heating the solution to 70°C for 24 hours, after which the solution was cooled and filtered. As the solid was still coloured, the decolourising step was repeated four times in total, however, some colour still remained. It was decided at this point to continue with the synthesis with the coloured ionic liquid, as the colour would be able to be removed at a later stage. The remaining water was removed through freeze-drying, and the solid was then heated under high vacuum for 48 hours at 65°C. The material was then cooled and the solid obtained. In order to check the purity of the final material, a ^{1}H NMR spectrum was compared with literature, and no significant impurities were found.

3.1.2 1-butyl-3-methylimidazolium bis(trifluoromethanesulfonyl)-amide (BMIM TFSA) Synthesis

BMIM TFSA was synthesised through the metathesis of 1-butyl-3-methylimidazolium chloride (BMIM Cl).[58] Clean BMIM Cl (40mL) was added to a solution of lithium bis(trifluoromethylsulfonyl)imide (150g in 165mL deionized water). This solution was then stirred overnight, with two layers resulting. The bottom layer was then separated and washed with deionized water (3 × 50mL). The BMIM TFSA was then heated under high vacuum for 48 hours at 65°C, and then filtered through activated alumina. The metathesis used coloured BMIM Cl and resulted in colourless BMIM TFSA, indicating that there were impurities in the n-chlorobutane used for BMIM Cl synthesis. This was later confirmed through 1H

NMR studies of starting materials and the ionic liquids synthesised. See Appendix One for ^{1}H NMR Spectra. In order to check the purity of the final material, a ^{1}H NMR spectrum was compared with literature, and no significant impurities were found.

3.1.3 Purification of Reichardt's Dye

Reichardt's Dye was purchased from Santa Cruz Biotechnology Ltd in 98% purity on a number of occasions. In most cases, this purity was sufficient for Raman spectroscopy measurements as there were only minimal fluorescence impurities affecting measurements. One batch, however, had a more significant fluorescence impurity that was large enough to have an effect on Raman spectroscopy measurements, leading to a very large fluorescence background. As such, this batch was recrystallized in methanol/water 3:1 then filtered before use.[34] In order to check the purity of the final material, a ^{1}H NMR spectrum was compared with literature, and no significant impurities were found.

3.1.4 Issues with Reichardt's dye and Solvent Impurities

It was found when preparing samples for initial studies that they tended to decolourize over time, sometimes time periods as short as a few days. It was initially thought this was due to the glassware used not being clean enough, and as such it was decided to clean all glassware with Pyroneg prior to use. As initial studies were only carried out with common organic solvents, this change in glassware treatment appeared to solve the problem.

It was found when initially preparing solutions of Reichardt's dye in ionic liquids, that some of these samples either remained colourless, or did not form as strong a colour as others. After considering previous issues with glassware cleanliness, it was hypothesized that there may be an issue with impurities in the ionic liquids. In order to test this, samples of Reichardt's dye in a selection of common organic solvents were pH adjusted by adding either concentrated acid or base to the sample. It was found that by adjusting the pH of the sample, the absorption of the Reichardt's dye changed dramatically. As such, it was decided that, in the case of ionic liquids remaining colourless upon addition of Reichardt's dye, there must be a small impurity of starting material, namely either acid or base,

remaining in the ionic liquid. Because of this problem with slight impurities in ionic liquids, a number of samples sometimes needed to be prepared in order to find an ionic liquid which did not have impurities affecting the pH of the sample.

3.2 Resonance Raman of RTILs as solvents

The following section describes the setup of the Raman spectroscopy systems used for the acquisition of resonance Raman data. As a range of wavelengths were required for data collection, multiple system setups were required. Data at 488nm, 514.5nm, and 633nm was collected at Massey University. Data at 532nm, 568nm, 594nm, and 647nm was collected at the University of Otago. The treatment of Raman data is described in detail in Section 3 of this chapter.

3.2.1 Data acquisition at Massey University

Resonance Raman measurements were completed using an incident beam and collection lens configured in a 180° back-scattering geometry. A notch filter (Iridian Spectral Technologies) was used to remove the incident laser wavelength before collection of the scattered photons at the spectrograph (Acton Research SpectraPro 2500i). The detector used was a liquid-nitrogen cooled Princeton Instruments SP2150i with a charge-coupled device (CCD) spectrometer (Princeton Instruments 7508-0001) and WinSpec/32 (version 2.5.16.5) software (Roper Scientific, Princeton Instruments).

3.2.1.1 Experimental Setup 488nm

Data at 488nm was acquired using an Argon/Ion laser (SpectraPhysics Model 165) with a power output of 24 mW measured at the sample. A 1200 g/mm grating was used, and the width of the slit allowing light to the detector was set to 150 μm, giving a spectral resolution of 2 – 3 cm^{-1}. Cyclohexane was used as a standard for calibration. All sample and solvent spectra, as well as dark and calibrated lamp spectra, were collected for 100 x 1 s exposures, however, due to some samples saturating the detector at this sample rate, samples of Reichardt's dye in BMPY TFSA and BMIM OAc, as well as dark and calibrated lamp spectra, were also acquired at 200 x 0.5 s exposures.

3.2.1.2 Experimental Setup 515nm

Data at 514.5nm was acquired using an Argon/Ion laser (SpectraPhysics) with a power output of 18 mW measured at the sample. A 1200 g/mm grating was used, and the width of the slit allowing light to the detector was set to 150 μm. Cyclohexane was used as a standard for calibration. All sample and solvent spectra, as well as dark and calibrated lamp spectra, were collected for 200 x 1 s exposures.

3.2.1.3 Experimental Setup 633nm

Data at 633nm was acquired using a Helium/Neon laser (ThorLabs) with a power output of 14 mW measured at the sample. A 1200 g/mm grating was used, and the width of the slit allowing light to the detector was set to 150 μm. Cyclohexane was used as a standard for calibration. All sample and solvent spectra, as well as dark and calibrated lamp spectra, were collected for 100 x 1s exposures.

3.2.2 Data acquisition at Otago University

Resonance Raman measurements were done using the experimental setup described in detail elsewhere.[59-62] To summarize, the incident beam and collection lens were configured in a 135° back-scattering geometry, to reduce self-absorption. A notch filter (Kaiser Optical Systems) was used to remove the incident laser wavelength before collection of the scattered photons at the spectrograph (Acton Research SpectraPro 500i). The detector used was a liquid-nitrogen-cooled back-illuminated Spec-10:100B CCD controlled by a ST-133 controller and WinSpec/32 (version 2.5.8.1) software (Roper Scientific, Princeton Instruments).

3.2.2.1 Experimental Setup 532nm

Data at 532nm was acquired using a solid state diode laser (Crystal Laser) with a power output of 36 mW measured at the sample. A 1200g/mm grating was used, and the width of the slit allowing light to the detector was set to 50μm. A toluene/acetonitrile solution was used for calibration. All sample and solvent spectra, as well as dark (i.e. absence of sample so as to measure influence of laser and environment on spectra) and calibrated lamp spectra, were collected for 200 × 1s exposures.

3.2.2.2 Experimental Setup 568nm

Data at 568nm was acquired using a Krypton ion laser (Innova I-302, Coherent, Inc.) with a power output of 34 mW measured at the sample. A 1200g/mm grating was used, and the width of the slit allowing light to the detector was set to 50μm. A toluene/acetonitrile solution was used for calibration. All sample and solvent spectra, as well as dark and calibrated lamp spectra, were collected for 300 × 1s exposures.

3.2.2.3 Experimental Setup 594nm

Data at 594nm was acquired using a solid state diode laser (Crystal Laser) with a power output of 36 mW measured at the sample. A 1200g/mm grating was used, and the width of the slit allowing light to the detector was set to 50μm. A toluene/acetonitrile solution was used for calibration. All sample and solvent spectra, as well as dark and calibrated lamp spectra, were collected at a range of exposures as there was a large variation in spectra quality if the same exposures were used. Methanol samples collected at 10 × 60s; ethanol and acetonitrile samples collected at 20 × 30s; dimethylsulfoxide, dichloromethane, and BMIM TFSA samples collected at 30 × 20s; BMIM OAc samples collected at 60 × 10s; and BMPY TFSA and BMIM PF_6 samples collected at 80 × 7s. Dark and calibrated lamp spectra were taken at all sampling settings used for solvents.

3.2.2.4 Experimental Setup 647nm

Data at 647nm was acquired using a Krypton ion laser (Innova I-302, Coherent, Inc.) with a power output of 60 mW measured at the sample. A 1200g/mm grating was used, and the width of the slit allowing light to the detector was set to 50μm. A toluene/acetonitrile solution was used for calibration. All sample and solvent spectra, as well as dark and calibrated lamp spectra, were collected for 150 × 2s exposures.

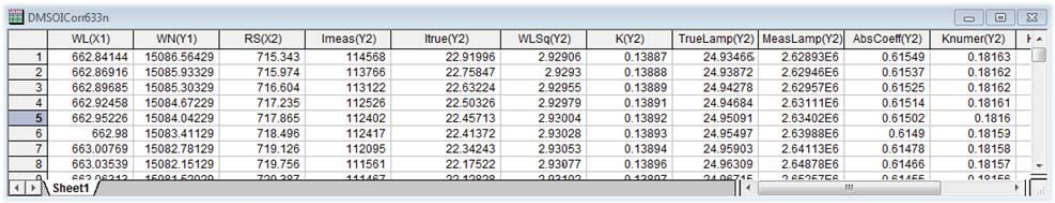
3.3 Resonance Raman Intensity Analysis

Note: This section has been written in such a way that it is able to be used as a guide for anyone performing similar analyses of Raman data. This section describes the initial steps of resonance Raman analysis of the samples. These steps

are undertaken prior to modelling of Raman intensities (which will be described in Section 4 of this chapter).

3.3.1 Conversion from Relative Intensity to True Intensity

Initially, resonance Raman and absorption spectra for each sample are imported into Origin as ASCII files, including dark and light Raman spectra. The file "ICorr" is then opened into the same project. The relevant Script Window (dependent on system which data was collected with) is then opened. The relevant White Light calibration data also must be imported into the Origin project.


DMSOICorr633n

	WL(X1)	WN(Y1)	RS(X2)	Imeas(Y2)	Itrue(Y2)	WLSq(Y2)	K(Y2)	TrueLamp(Y2)	MeasLamp(Y2)	AbsCoeff(Y2)	Knumer(Y2)
1	662.84144	15086.56429	715.343	114568	22.91996	2.92906	0.13887	24.93465	2.62893E6	0.61549	0.18163
2	662.86916	15085.93329	715.974	113766	22.75847	2.9293	0.13888	24.93872	2.62946E6	0.61537	0.18162
3	662.89685	15085.30329	716.604	113122	22.63224	2.92955	0.13889	24.94278	2.62957E6	0.61525	0.18162
4	662.92458	15084.67229	717.235	112526	22.50326	2.92979	0.13891	24.94684	2.63111E6	0.61514	0.18161
5	662.95226	15084.04229	717.865	112402	22.45713	2.93004	0.13892	24.95091	2.63402E6	0.61502	0.1816
6	662.98	15083.41129	718.496	112417	22.41372	2.93028	0.13893	24.95497	2.63988E6	0.6149	0.18159
7	663.00769	15082.78129	719.126	112095	22.34243	2.93053	0.13894	24.95903	2.64113E6	0.61478	0.18158
8	663.03539	15082.15129	719.756	111561	22.17522	2.93077	0.13896	24.96309	2.64878E6	0.61466	0.18157

Sheet1

Figure 3.1 - Example of "ICorr" window in Origin after conversion

Before the script can be run to do the conversions, the Raman intensity data for the sample must first be corrected for background. This is done by removing the dark spectrum. This corrected Raman intensity data is then copied into "ICorr" in cell "IMeas(Y2)", and at the same time, the Raman shift data is copied into the cell "RS(X2)". The measured lamp spectrum (light spectrum) is then copied into "ICorr" into "MeasLamp(Y2)". The first section of the script is then run in order to convert Raman shift to λ and ν. The script section is as follows:

```
%B=ICorr488DCM;
WVLGTH=487.986;
%B_WN=1e7/WVLGTH-%B_RS;
%B_WL=1e7/%B_WN;
```

Name allocated to "ICorr" window

Laser wavelength used for data collection

The white light calibration file is then integrated so as to give its value at each of the data points (based on wavelength). This is done by firstly fitting a power curve to the data. It was found that if the data was collected at the University of Otago a Power1 relationship gave the best fit, whereas if the data was collected at Massey University a Power2 relationship gave the best fit. This curve-fitted data is then interpolated in order to get the desired number of data points (1340) over the desired wavelength range. The interpolated data is then copied into "ICorr" into "TrueLamp(Y2)". The absorption spectra is then treated in a similar way as the

white light calibration data, however, instead of a power curve being fitted to the data, the Peak Fitting function in Origin was used (which will be described in Section 3.3 of this chapter). The interpolated absorption spectrum is then copied into "ICorr" into "AbsCoeff(Y2)". The remaining sections of the script are then run as follows:

```
%B=ICorr488MeOH;
%B_WLSq=%B_WL^2/150000;
```

cos(θ) and tan(α) change based on the experimental setup of the Raman

Absorption of sample at laser wavelength

```
%B=ICorr488MeOH;
costheta=1;
tanalpha=0.4636;
sigmaLaser=0.2568;
%B_Knumer=atan((%B_AbsCoeff*costheta/(2*sigmaLaser+2*%B_AbsCoeff*costheta))^0.5*tanalpha);
%B_Kdenom=((1+(%B_AbsCoeff/sigmaLaser)*costheta)*(%B_AbsCoeff/sigmaLaser)*costheta)^0.5;
%B_K=%B_Knumer/%B_Kdenom;
```

```
%B=ICorr488MeOH;
%B_C=%B_WLSq*%B_TrueLamp/(%B_K*%B_MeasLamp);
%B_Itrue=%B_Imeas*%B_C;
```

Once this has been completed, the true intensity values "ITrue(Y2)" are then able to be copied into a new workbook along with Raman shift values prior to continuing on with background subtraction and peak fitting.

3.3.2 Background Subtraction

Any linear background which is present after performing the above conversions is able to be simply removed using the Peak Analyzer in Origin to perform a simple baseline subtraction. This is done simply by setting the baseline mode to "constant".

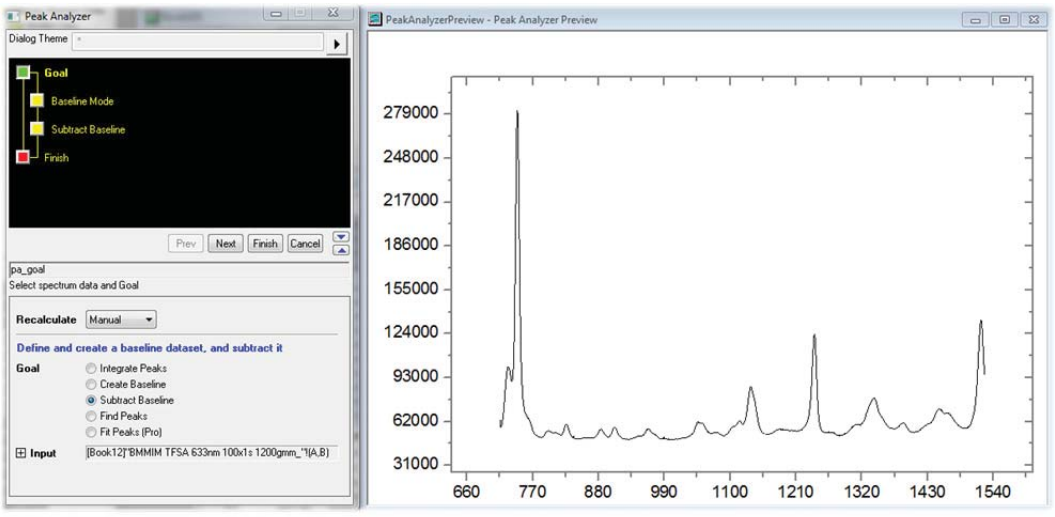


Figure 3.2 - Peak Analyzer in Origin

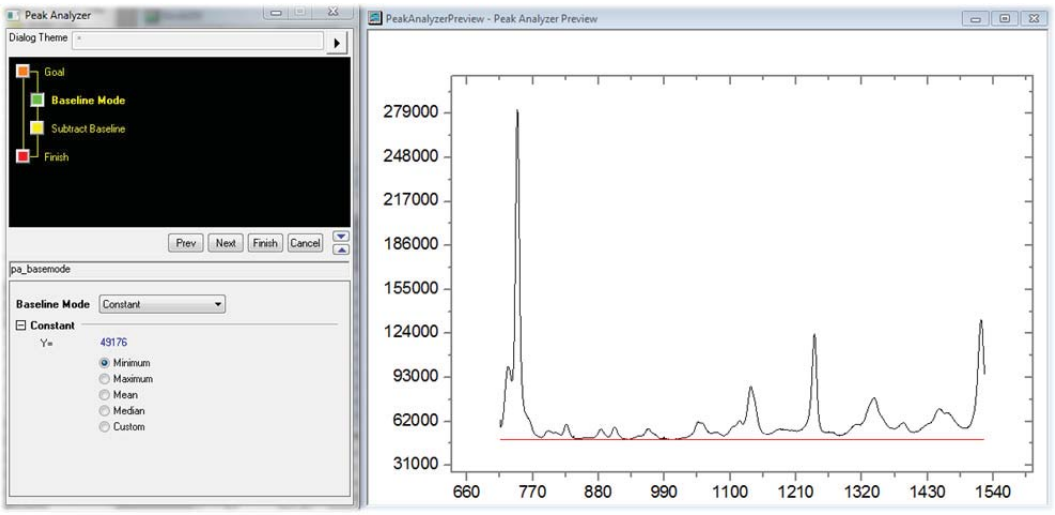


Figure 3.3 - Subtracting a linear background in Origin

Non-linear backgrounds (i.e. when there is fluorescence present in the sample) are more complicated to subtract, however, this can also be done in the Peak Analyzer in Origin. A User Defined baseline is needed. Once this has been chosen, the approximate number of points needed is able to be determined, and they will be approximately positioned on the spectrum (see Figure 3.4).

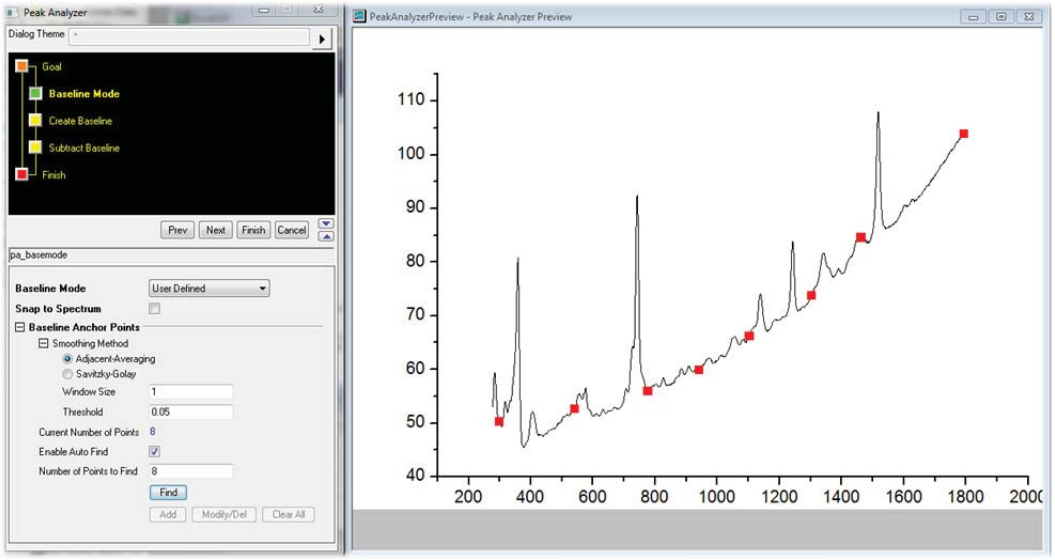


Figure 3.4 - Subtracting a non-linear background in Origin

Once the points for baseline subtraction have been approximated they are able to be modified, and either a linear or spline fitting function used, as shown in Figure 3.5.

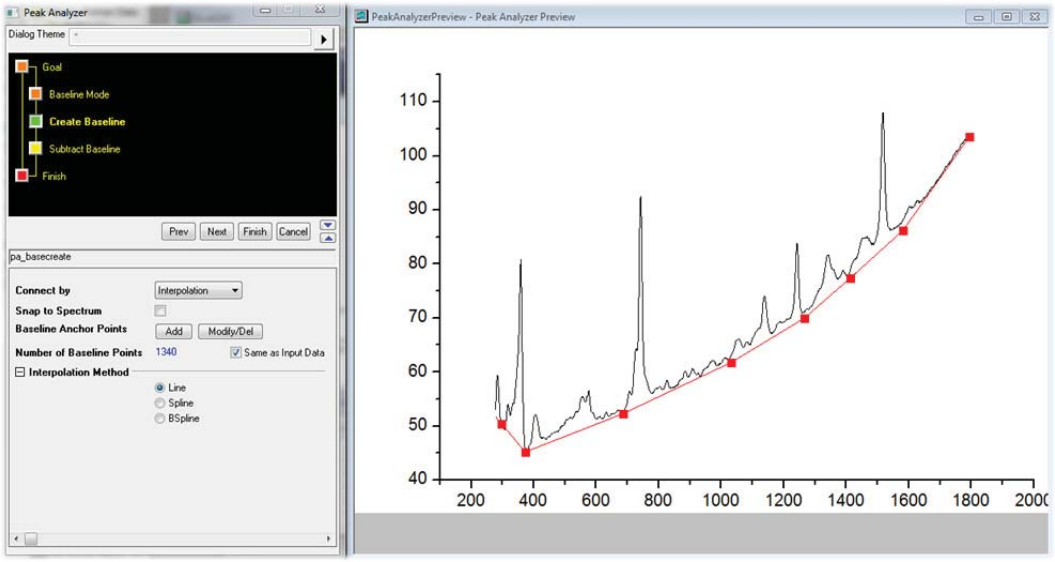


Figure 3.5 - After modifying points for user defined baseline subtraction in Origin

Once this has been done, the background is able to be removed in order to check the approximation of baseline is accurate before finalising the baseline subtraction (see Figure 3.6).

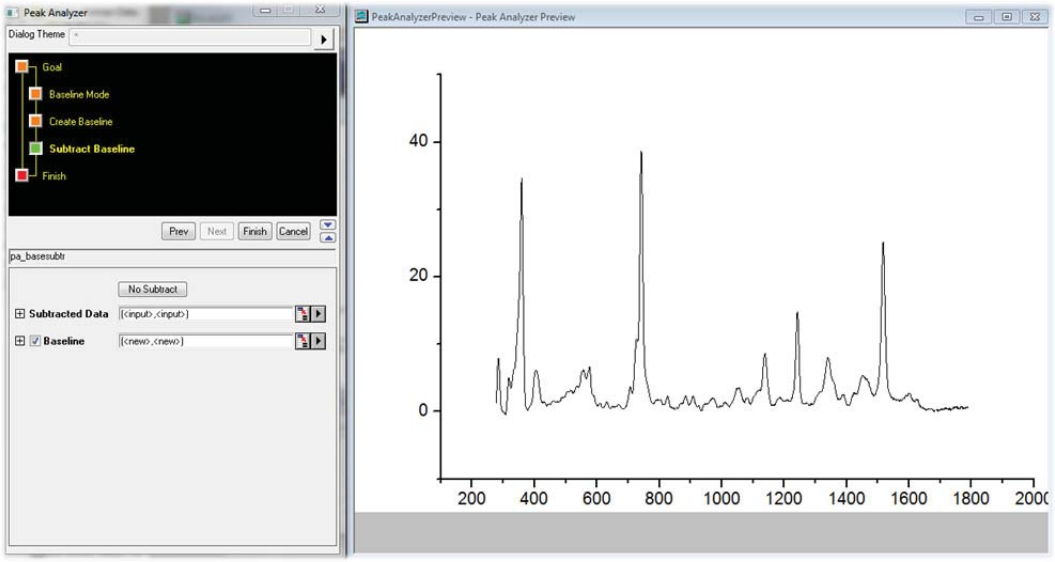


Figure 3.6 - Final stage of subtracting baseline from non-linear data in Origin

This data is then able to be used for peak fitting in Origin.

3.3.3 Peak Fitting

Peak fitting is performed using the Peak Analyzer function in Origin. Fit Peaks (Pro) allows any peaks in the spectrum to be fitted with a number of functions.

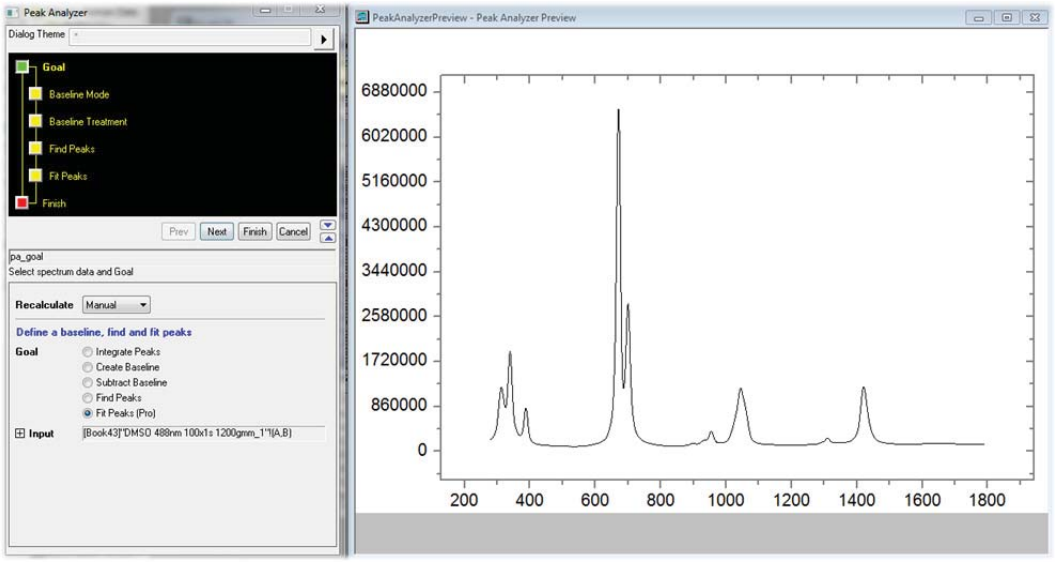


Figure 3.7 - The Fit Peaks function in Origin can be used for peak fitting

Once any background still present has been subtracted using the baseline treatment step, Origin can be used to find peaks present in the spectra (see Figure 3.8). Through changing the threshold height in the Peak Filtering sub-menu the sensitivity of this “Auto Find” can be adjusted.

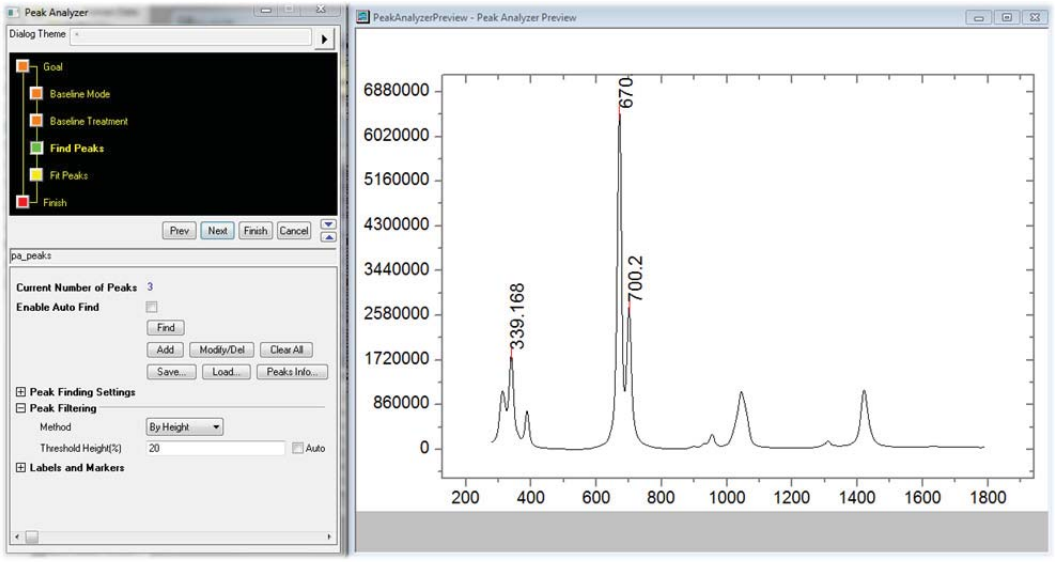


Figure 3.8 - The "Auto Find" function in Origin

In addition to this “Auto Find” the “add” button can be used to add peaks which are not significant enough to be found through the automatic method, as shown in Figure 3.9.

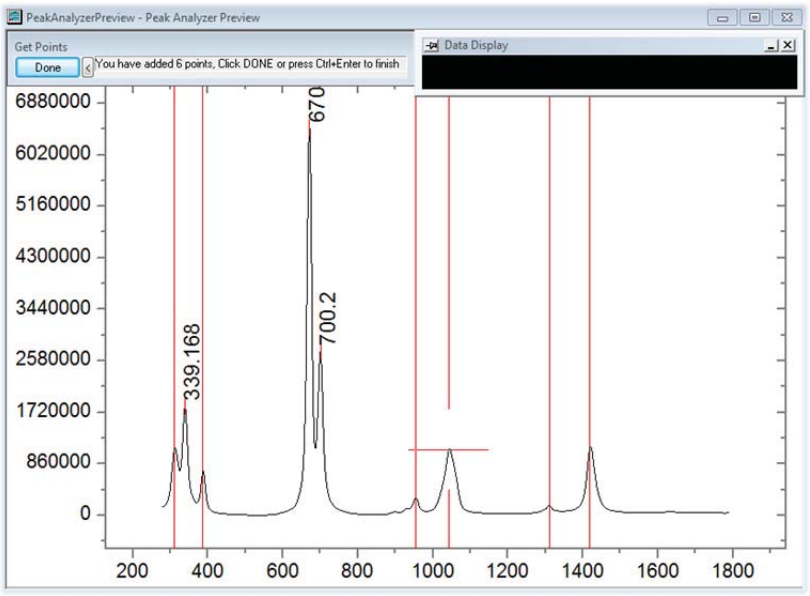


Figure 3.9 - Adding peaks manually for peak fitting

Once the peaks have been found, the "Fit Control" settings are able to be changed in order to fit the peaks to as high a degree of accuracy as possible. Changing the fitting function to be used is shown in Figure 3.10.

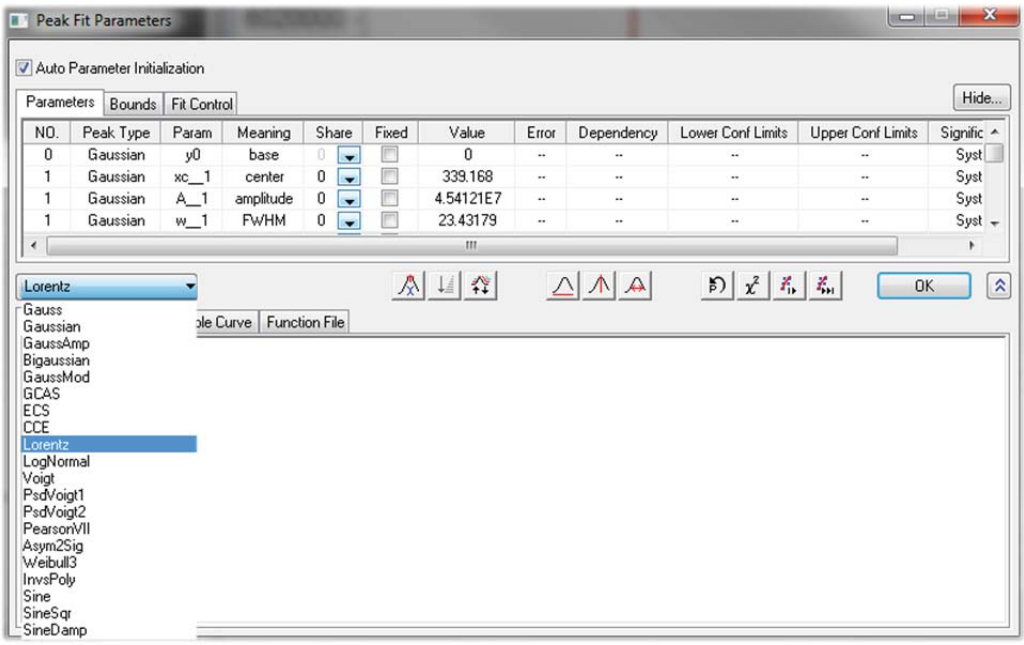


Figure 3.10 - Selecting the fitting function

Figure 3.11 shows how bounds can be applied to the fitting function. In this case, only peaks having positive areas are allowed.

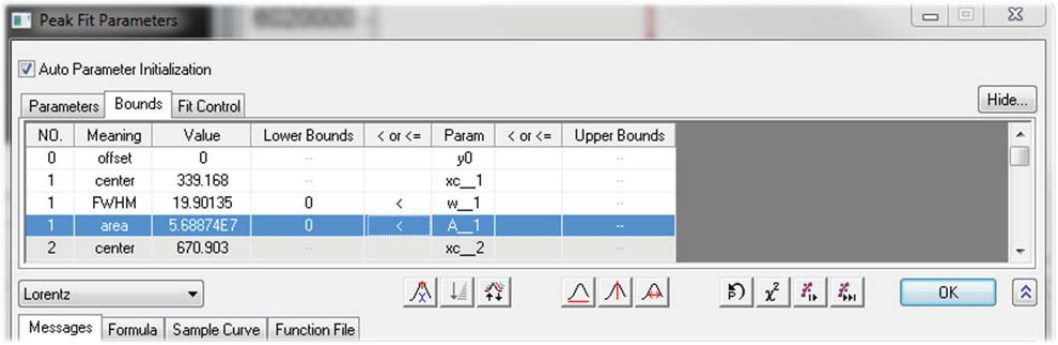


Figure 3.11 - Applying bounds to the fitting function

The tolerance and number of iterations is also able to be selected based on preference (as shown in Figure 3.12). The number of peaks present which are to be fitted has a direct impact on the time which the fit will take, as does the number of iterations. If the number of peaks is large, small numbers of iterations are best, as using a large number of iterations can cause the program to fail. With ionic liquid spectra, I found that an iteration number larger than 5000 would cause the program to freeze.

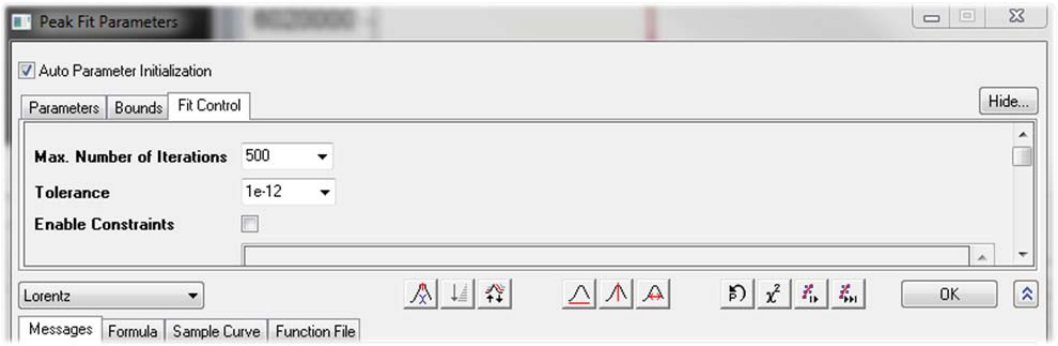


Figure 3.12 - Selecting the tolerance and number of iterations to be performed

Once the settings have been selected, a fit is able to be performed. The output for a converged fit is shown in Figure 3.13, however, if the fit does not converge after the selected number of iterations, either more iterations can be performed, or the peak positions and bounds are able to be adjusted.

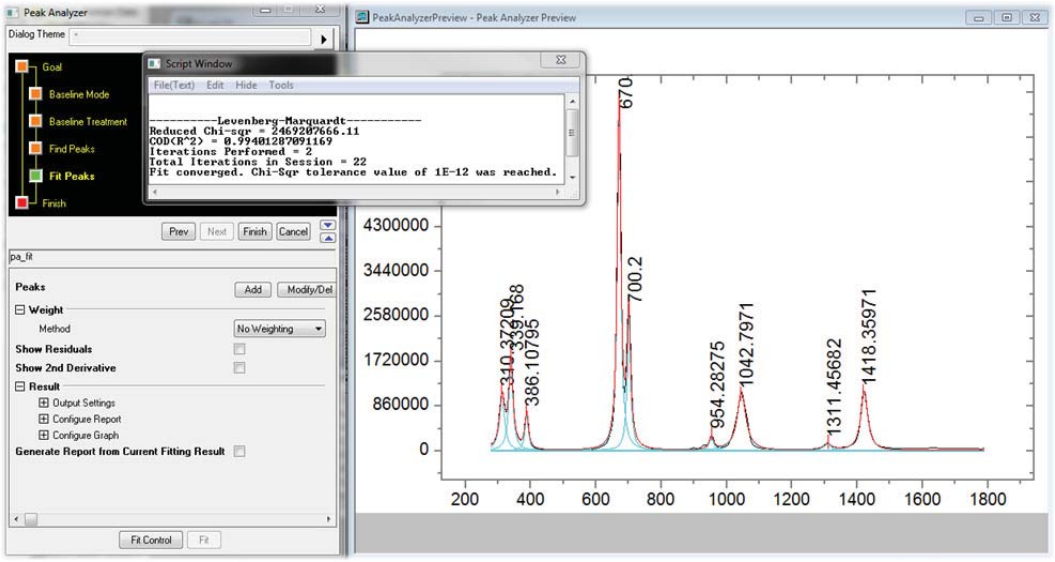


Figure 3.13 - An example of a spectrum fitted with a Chi-Sqr tolerance of $1x10^{-12}$

Upon exiting the Peak Analyzer, an output summary is shown (see Figure 3.14). This gives a summary of the peaks, and their positions, and also acts as a record of the accuracy of the fit performed.

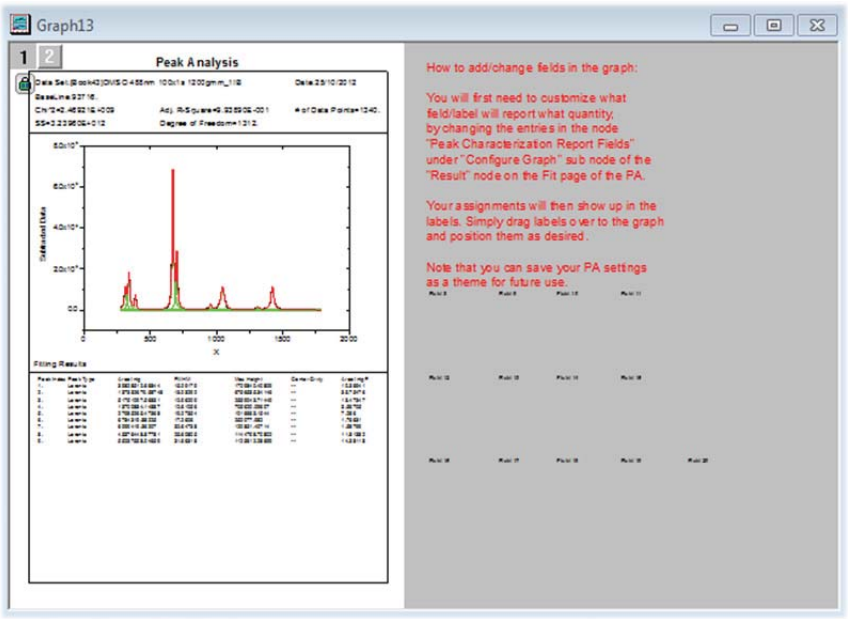
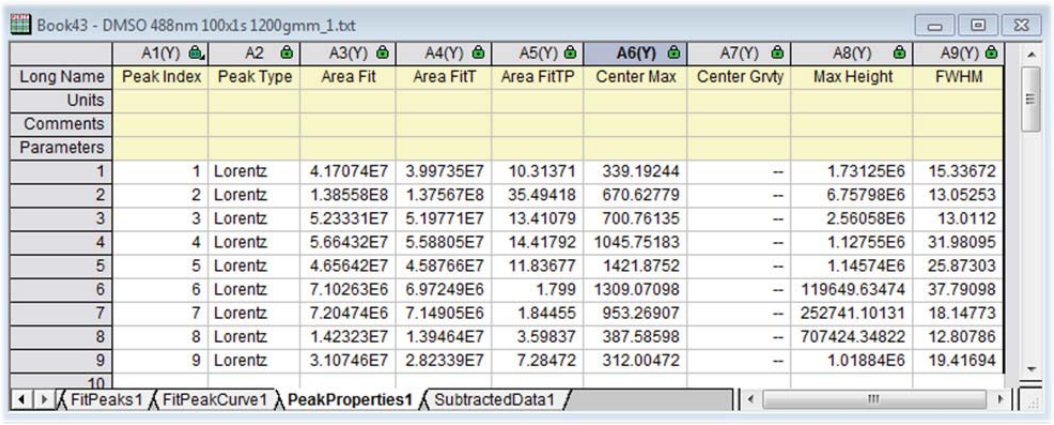


Figure 3.14 - Fitting output summary

After the peak fitting has been performed, peak fitting information is automatically inserted into the worksheet the spectral data is in. This data includes the Peak Properties, which are very important for the calculation of scattering cross-sections, and is shown in Figure 3.15.



Book43 - DMSO 488nm 100x1s 1200gmm_1.txt

	A1(Y)	A2	A3(Y)	A4(Y)	A5(Y)	A6(Y)	A7(Y)	A8(Y)	A9(Y)
Long Name	Peak Index	Peak Type	Area Fit	Area FitT	Area FitTP	Center Max	Center Grvty	Max Height	FWHM
Units									
Comments									
Parameters									
1	1	Lorentz	4.17074E7	3.99735E7	10.31371	339.19244	--	1.73125E6	15.33672
2	2	Lorentz	1.38558E8	1.37567E8	35.49418	670.62779	--	6.75798E6	13.05253
3	3	Lorentz	5.23331E7	5.19771E7	13.41079	700.76135	--	2.56058E6	13.0112
4	4	Lorentz	5.66432E7	5.58805E7	14.41792	1045.75183	--	1.12755E6	31.98095
5	5	Lorentz	4.65642E7	4.58766E7	11.83677	1421.8752	--	1.14574E6	25.87303
6	6	Lorentz	7.10263E6	6.97249E6	1.799	1309.07098	--	119649.63474	37.79098
7	7	Lorentz	7.20474E6	7.14905E6	1.84455	953.26907	--	252741.10131	18.14773
8	8	Lorentz	1.42323E7	1.39464E7	3.59837	387.58598	--	707424.34822	12.80786
9	9	Lorentz	3.10746E7	2.82339E7	7.28472	312.00472	--	1.01884E6	19.41694
10									

FitPeaks1 | FitPeakCurve1 | PeakProperties1 | SubtractedData1

Figure 3.15 - The peak information given through the peak fitting function

After peak fitting has been performed and all data acquired, solvent and sample spectra are able to be used to calculate scattering cross-sections.

3.3.4 Calculation of Solvent Cross-Sections

An internal standard method is used to determine the absolute differential Raman cross-sections of Reichardt's Dye. The solvent is a convenient choice of the internal intensity standard as the absolute Raman cross-sections of most common solvents have been reported in the literature. However, for some solvents and all of the ionic liquids used in this work the absolute differential Raman cross-sections are not known and must therefore be determined. This section describes the process of determining absolute differential Raman cross-sections using an external standard method.

In order to determine the unknown cross-sections, Raman spectra are collected under the same experimental conditions for a selection of reference solvents and the unknowns. Each sample is in a separate sample vial, and prior to full data collection, one second exposures are collected for each sample, so as to determine the maximum exposure time that can be used for all samples. This is done as there is a large amount of variance in the maximum intensities of solvent peaks, and the detector cannot be saturated for any of the acquisitions. Once the optimum exposure time has been found, an optimum exposure number is also chosen so as to obtain a good signal to noise ratio. During data collection the samples are spun so as to ensure that there are no effects from photoproducts.[53] Once the data has been collected, the peak fitting process described above can be performed in order to obtain solvent peak areas. As the calculations which are performed to determine

cross-sections use peak area ratios, no other data transformations need to be performed.

Absolute total and differential cross-sections are able to be determined for solvents through the use of a standard Excel worksheet, which is able to be adapted on a case-by-case basis. The calculations which are performed using this worksheet utilise experimentally determined values of ν_e, K, and Raman shift of solvent peak for a selection of solvents. The total cross-sections of the reference compounds are able to be calculated using the following equation:

$$\sigma_R(\nu_0) = KF_A^2(\nu_0)$$

where ν_0 is the incident frequency and where:

$$F_A = \frac{\nu^2(\nu_e^2 + \nu_0^2)}{(\nu_e^2 - \nu_0^2)^2}$$

Once the total cross-sections of the reference compounds have been calculated, using previously reported values for K and $\nu_e$the differential cross-sections of the reference compounds can then be calculated using the following equation:

$$(d\sigma_R/d\Omega) = \frac{3}{8\pi}\left(\frac{1+\rho^*}{1+2\rho^*}\right)\sigma_R$$

where ρ^* is the unknown depolarization ratio. The unknown differential cross-section is then able to be determined. This is done by calculating the unknown cross-section relative to the reference cross-sections, then averaging the results. In order to calculate these relative cross-sections, the following equation is used:

$$(d\sigma/d\Omega)_1 = \frac{I_1}{I_2}\left(\frac{n_1}{n_2}\right)^2\frac{\rho_2}{\rho_1}(d\sigma/d\Omega)_2$$

where ρ is the density in mol dm^{-3}, I is the fitted peak area of the major Raman peak of the liquid, and n is the refractive index of the liquid. After the average value of cross-section has been calculated for each incident frequency of interest, the ν^4 dependence can be removed by dividing each value by $\nu^3 \cdot \nu_0$ with each of these terms defined as above. The average value of $(d\sigma/d\Omega)/\nu^3 \cdot \nu_0$ in units of μb sr^{-1}

(where 1 b = 10^{-24} cm^2) is then able to be used in order to calculate values of differential cross-section at other incident frequencies. Alternatively, an Albrecht A-term expression can be fitted to the experimental cross-sections to extract the K and ν_e for the unknown solvent cross-sections.

3.3.5 Calculation of Solute Cross-Sections

Cross-sections are able to be calculated for solutes (in this case Reichardt's dye) in a range of solvents. This is done using the following equation:

$$\left(\frac{d\sigma}{d\Omega}\right)_{dye} = \frac{A_{dye\,peak}}{A_{solv\,peak}} \cdot \frac{\rho_{solvent}}{c_{dye}} \cdot \left(\frac{d\sigma}{d\Omega}\right)_{solvent}$$

where $\rho_{solvent}$ is the density, c_{dye} is the concentration of Reichardt's dye in the solvent, $A_{dye\,peak}$ and $A_{solv\,peak}$ are the dye and solvent peak areas respectively, obtained from Origin peak fitting output (after conversion to true intensity), and where $(d\sigma/d\Omega)_{Solvent}$) is in units of 10^{12} $Å^2$ sr^{-1}.

3.4 Raman Intensity Modelling

This section has been written in such a way that it is able to be used as a guide for anyone performing similar analyses of Raman data. This section describes the steps involved in the modelling of resonance Raman intensities, as well as a worked example of the modelling undertaken in this project. For a more detailed description of the mathematics behind the modelling simulations undertaken see Chapter 2.

3.4.1 Transition Dipole Length

The transition dipole length is required for the input file for the simulations. It is able to be calculated using the following equation:

$$\mu(\text{Å}) = \frac{\mu_{fi}}{e}$$

where ***e*** is the elementary charge and is equal to 1.60 x 10^{-19} C, and where:

$$\boldsymbol{\mu_{fi}} = \sqrt{\frac{3\varepsilon_0 hc\mathcal{A}}{2\pi^2 N_A \nu_{fi}}}$$

where $\mathcal{A}$ is the integrated area of the sample absorption profile in cm mol^{-1}, ε_0 is the permittivity of a vacuum and is equal to 8.854 x 10^{-12} J^{-1} C^2 m^{-1}, h is the Planck constant and is equal to 6.626 x 10^{-34} J s, c is the speed of light in a vacuum equal to 2.998 x 10^8 m s^{-1}, N_A is the Avogadro constant equal to 6.022 x 10^{23} mol^{-1}, and ν_{fi} is the position of the band centre in cm^{-1}. Once this value has been calculated, it can be copied into the .fin input file for simulations.

3.4.2 Preparing Input Files

The following sections describe the files which are required to be prepared for modelling. These files must be in the same folder directory as each other, with one folder being prepared for each sample.

3.4.2.1 Absorption Spectra

For modelling, the absorption spectra must be imported into the text file "expspec.txt". In order to have the correct dimensions for modelling, the x-axis of the absorption spectra must be converted from wavelength (nm) to wavenumber (cm^{-1}), whilst the y-axis must be converted from ε (L mol^{-1} cm^{-1}) to σ_A (Å^2). This second conversion can be performed using the following equations:

$$\sigma_A(cm^2\ mol^{-1}) = 10^3 \ln 10 \times \varepsilon$$

and:

$$\sigma_A(\text{Å}^2) = \frac{\sigma_A(cm^2\ mol^{-1})}{N_A(mol)} \times 10^{16}(\text{Å}^2 cm^{-2})$$

3.4.2.2 Cross-Sections

The solute cross-sections at each wavelength must be imported into the text files "exptsx***.txt" where *** indicates the laser wavelength at which the cross-sections were determined. The formatting of the original "exptsx***.txt" file must be maintained in order for the simulations to work correctly.

3.4.2.3 Final Input File

The last input file which must be prepared for simulations is a .FIN, or final input, file, the first section of which is shown below:

```
# Twostate.in for Reichardt's Dye in MeOH

#nmode, nline, ntime, nfreq, bcut, iprof
19,19,2500,7,1,1

#sig, cutoff, temp, angle,,
#sig - electronic inhomogeneos broadening
#Look at DFT calculations to see if ES1 and ES2 are collinear

0,1.00E-05,298,0

# E00, D, K, Mu
# E00 Electronic Origin
# D electronic homogeneous broadening
#,Increasing widens curve
#,Tends to dampen Raman scattering (all of it - all modes)
# K - don't change
# Mu Transition Dipole Length

12680,3700,0.1,0.423
21490,3780,0.1,0

#MLCT State = State 1
#LC State = State 2
#Homogeneous Broadening is greater in ES1 state because of larger dipole change

# Alow, Ahigh, Delta, Refrac
# Alow, Ahigh - lowest & highest energies to calculate absortion
# Delta - Time step in Fourier transform (usually about 0.5)
# Refrac - Solvent refractive index
11000,25000,0.1,1.331

# The 7 excitation frequencies:
20492.39,19435.21,18796.99,17599.44,16843.52,15801.91,15453.56
```

The values of nmode and nline are simply equal to the number of modes of interest for the sample, whilst nfreq is the number of laser incident frequencies for which data has been collected and is of interest for. The other values from the first line of code (ntime, bcut, and iprof) are generally constants. The values of sig, cutoff, temp, and angle are also assumed to be constants. E00 is the position of the maximum of the absorption peak, D represents the electronic homogeneous broadening, K is the ratio of the time-scale and magnitude parameter in the model for the solvent broadening, and Mu is equal to the transition dipole length μ calculated in 2.4.1. Increasing the value of D widens the curve approximating the absorption profile, and tends to dampen the Raman scattering of all modes. This means that if the value of D is increased significantly, the Raman scattering contribution of all the modes will need to be increased (by increasing the Δ values for each mode) in order to balance this change. It can be seen that there are two rows of values of E00, D, K, Mu. This is due to the presence of both excited states

(ES1 and ES2), both of which will have different values for E00, D, and Mu. Alow and Ahigh are the lowest and highest energies used to calculate the absorption profile respectively. Delta is the time step in the Fourier transform, and Refrac is the refractive index of the solvent used.

The next section of the .FIN file is shown below:

```
# ES1 State Freqs and Deltas:
1622,1622,0.278,0
1602,1602,0.200,0
1585,1585,0.340,0
1497,1497,0.412,0
1449,1449,0.05,0
1417,1417,0.330,0
1360,1360,0.290,0
1320,1320,0.300,0
1295,1295,0.311,0
1209,1209,0.170,0
1057,1057,0.05,0
1000,1000,0.05,0
645,645,0.355,0
605,605,0.380,0
420,420,0.420,0
336,336,0.350,0
289,289,0.380,0
231,231,0.650,0
133,133,1.200,0

# ES2 State Freqs and Deltas:
1622,0.278,0
1602,0.200,0
1585,0.340,0
1497,0.412,0
1449,0.05,0
1417,0.330,0
1360,0.290,0
1320,0.300,0
1295,0.311,0
1209,0.170,0
1057,0.05,0
1000,0.05,0
645,0.355,0
605,0.380,0
420,0.420,0
336,0.350,0
289,0.380,0
231,0.650,0
133,1.200,0
```

The ES1 and ES2 State Freqs and Deltas sections contain the information for the vibrational modes which are being modelled. The Freqs are the vibrational frequencies for the ground and excited state (it assumed these are equal in the absence of any experimental evidence to suggest otherwise) and the Deltas (Δ) are the dimensionless mode displacements between the ground and excited state

equilibrium geometries. The deltas are related to the displacements (in Angstrom for example) by:

$$\Delta Q = \sqrt{\frac{m\omega}{\hbar}}\Delta X$$

where $\Delta Q$is the delta value, and ΔX is the change in bond length. Modelling gives deltas, which are general displacements in dimensionless coordinates. $\Delta Q$is the dimensionless displacement along a normal coordinate, which is a linear combination of bond length, angle, and torsion coordinates, i.e. the "internal" coordinates.

An important point should be noted about the mode displacements. Only the magnitude of the displacement affects the calculated Raman cross-section, the calculation is insensitive to the sign of the displacement. This arises due to the appearance of only Δ^2 terms in the explicit expressions for the overlap factors generated by the wavepacket dynamics. The delta and frequency values are independent of the excitation frequency because they relate the displacement between the equilibrium geometries of the ground and excited states. As, in the case of Reichardt's dye, only one state is of interest, only the data for the ES1 state needs to be adjusted, as the transition dipole length for the other ("ES2") state will be set to zero, and, as such, this state will be ignored by the modelling program. In order to calculate the contribution of each mode (the second last column in each) the solute cross-sections need to be calculated relative to each other. As the intensities of the modes are related through $I \propto \omega^2\Delta^2$ if the most intense mode is chosen to have a particular value (usually 0.75), the relative contributions can be found using:

$$\Delta_u = \frac{\omega_{ref}^2\Delta_{ref}^2}{\omega_u^2}\frac{I_u}{I_{ref}}$$

where Δ_u, ω_u, and I_u are the unknown contribution, incident frequency, and intensity respectively, and Δ_{ref}, ω_{ref}, and I_{ref} are the reference contribution, incident frequency, and intensity. Any modes which have a negligible contribution at the incident frequency chosen are given a small relative contribution value, so as

to allow other incident frequencies in which they are present to be calculated accurately.

The following matrix is the final section of the .FIN file. It describes the composition of any overtone or combination modes that appear in the Raman spectrum in terms of the fundamental modes that are listed in the frequency and delta table. Although in this case the matrix is diagonal as no overtone or combination modes appear in any of the observed spectra. This is often the case for large molecules with large numbers of active modes. The so-called multi-mode dephasing effect prevents the occurrence of overtone and combination bands in the spectra.

```
# The matrix
0,0,0,0,0,0,0,0,0,0,0,0,0,0,0,0,0,0,1
0,0,0,0,0,0,0,0,0,0,0,0,0,0,0,0,0,1,0
0,0,0,0,0,0,0,0,0,0,0,0,0,0,0,0,1,0,0
0,0,0,0,0,0,0,0,0,0,0,0,0,0,0,1,0,0,0
0,0,0,0,0,0,0,0,0,0,0,0,0,0,1,0,0,0,0
0,0,0,0,0,0,0,0,0,0,0,0,0,1,0,0,0,0,0
0,0,0,0,0,0,0,0,0,0,0,0,1,0,0,0,0,0,0
0,0,0,0,0,0,0,0,0,0,0,1,0,0,0,0,0,0,0
0,0,0,0,0,0,0,0,0,0,1,0,0,0,0,0,0,0,0
0,0,0,0,0,0,0,0,0,1,0,0,0,0,0,0,0,0,0
0,0,0,0,0,0,0,0,1,0,0,0,0,0,0,0,0,0,0
0,0,0,0,0,0,0,1,0,0,0,0,0,0,0,0,0,0,0
0,0,0,0,0,0,1,0,0,0,0,0,0,0,0,0,0,0,0
0,0,0,0,0,1,0,0,0,0,0,0,0,0,0,0,0,0,0
0,0,0,0,1,0,0,0,0,0,0,0,0,0,0,0,0,0,0
0,0,0,1,0,0,0,0,0,0,0,0,0,0,0,0,0,0,0
0,0,1,0,0,0,0,0,0,0,0,0,0,0,0,0,0,0,0
0,1,0,0,0,0,0,0,0,0,0,0,0,0,0,0,0,0,0
1,0,0,0,0,0,0,0,0,0,0,0,0,0,0,0,0,0,0
```

3.4.3 Initial Simulations

This section contains a brief overview of the procedure involved in running the simulations in Origin. Figure 3.16 shows a screen shot of the code builder in Origin, where the codes used for the simulation process are rebuilt each time Origin is reopened. Once the codes are rebuilt, the customised simulation function can be run for a .FIN file of interest.

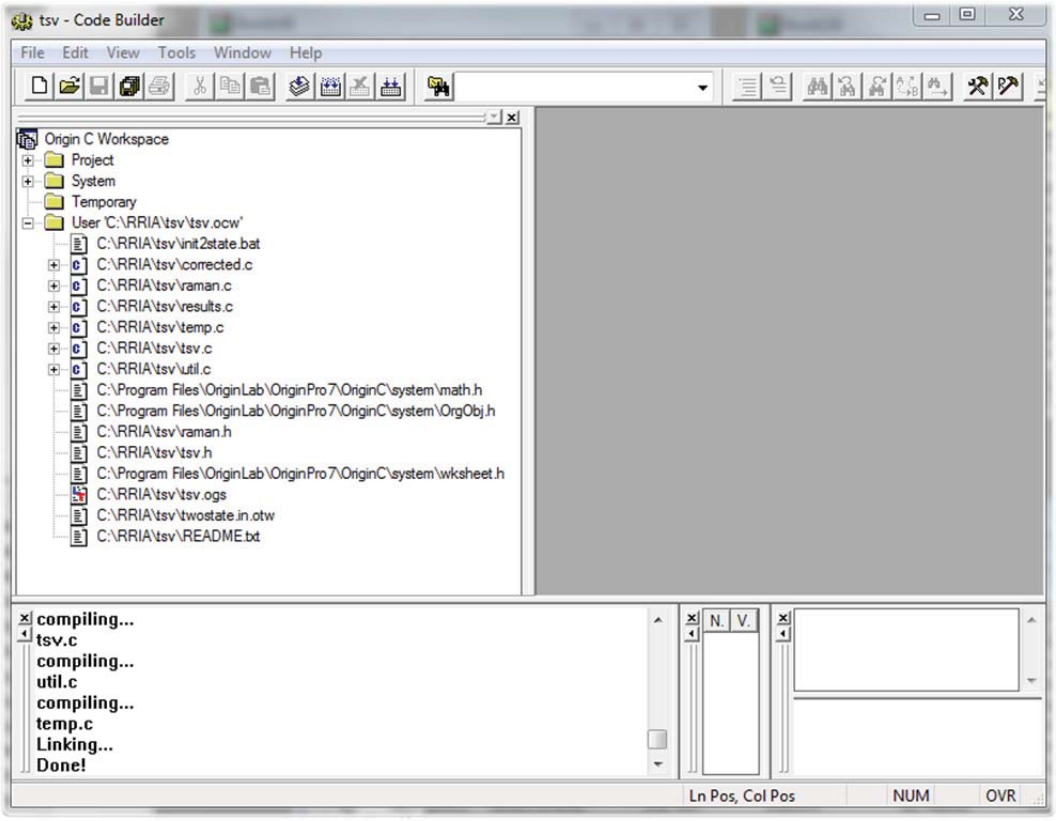


Figure 3.16 - The code builder in Origin

Once the .FIN file has been run, Origin outputs an absorption spectrum showing the comparison between experimental and simulated absorption cross-section. This spectrum is able to be used to adjust the homogeneous broadening, electronic origin, and transition dipole length parameters so as to give the best agreement between experimental and simulated data. Once the absorption spectra show good agreement, the agreement between simulated and experimental Raman cross-sections is able to be investigated.

3.4.4 Raman Profiles

In order to investigate the agreement between experimental and simulated Raman cross-sections, profiles of each of the mode are used. As a part of the simulations, Raman profiles are calculated for each mode of interest. These profiles are then able to be compared to the experimental data. This comparison is of great interest, as it is used to determine whether the calculated delta values are accurate, or whether they need to be adjusted. Adjusting each delta will have an effect on both the simulated Raman and absorption profiles, and the correct calculations of

these delta values is imperative, as they have a significant effect on the calculation of electronic parameters.

3.5 Computational Studies

Note: The computational results reported in this thesis were carried out with assistance from my supervisor.

To aid in the interpretation of the vibrational mode parameters from the Raman intensity modelling, a description of the normal modes of Reichardt's Dye was obtained using a geometry optimization and normal mode analysis using density functional methods in the Gaussian09 package.

Detailed descriptions of the computational details can be found elsewhere. Furthermore, although the veracity of the DFT output should be checked by a systematic study of the selected functionals, it has been shown in previous studies that the ubiquitous B3LYP functional provides adequate results. The relatively large size of Reichardt's molecules restricted the selected basis set size to 6-31+G(d), with diffuse functions included due to the presence of the zwitterion and polarisable functions included to account for polarisation effects due to the presence of the zwitterion dipole. Some difficulties were encountered in initial attempts at SCF convergence with each SCF convergence taking several hours. However, it appeared this was due to a poor guess under the default guess option (extended Huckel) and starting the B3LYP/6-31+G(d) from a previous semi-empirical PM3 calculation lead to much quicker convergence for the SCF procedure (a few minutes). No difficulties were encountered with the geometry optimisation or frequency calculations steps.

Chapter 4 – Reichardt's Dye in Common Solvents

4.1 Reichardt's Dye Absorption Spectra

The absorption spectra of Reichardt's dye in common solvents were collected using a Cary 100 Bio spectrophotometer (Varian Inc.) with 1cm quartz cuvettes.

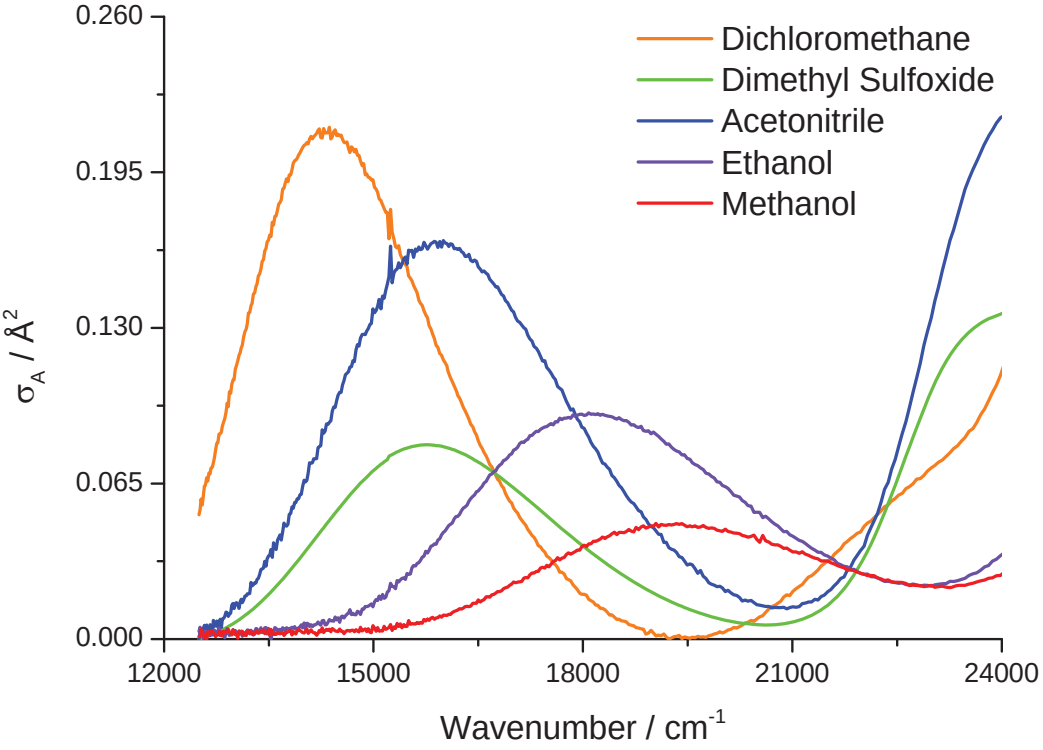


Figure 4.1 - Overlaid absorption spectra for Reichardt's dye in common organic solvents

Analysing the positions of the maxima, the degree of excitation of the dye is able to be determined. This gives an indication as to which state or states the dye exists in the selected solvent. Figure 4.1 shows the relative positions of absorption maxima, and absorption cross-sections, of Reichardt's dye in the common organic solvents used in this study. The significant shift of absorption maxima as a function of solvent polarity is able to be seen easily. As stated in 1.2, an absorption maximum at 810 nm corresponds to diphenyl ether, the most nonpolar solvent in which Reichardt's is soluble, whereas an absorption maximum at 453 nm corresponds to the dye in water. As solvent polarity increases, the dipolar ground state of the dye is more stabilised through solvation than the less dipolar Franck-

Condon excited state, which may be destabilised due to its solvation shell being equal to that of the ground state.[25]

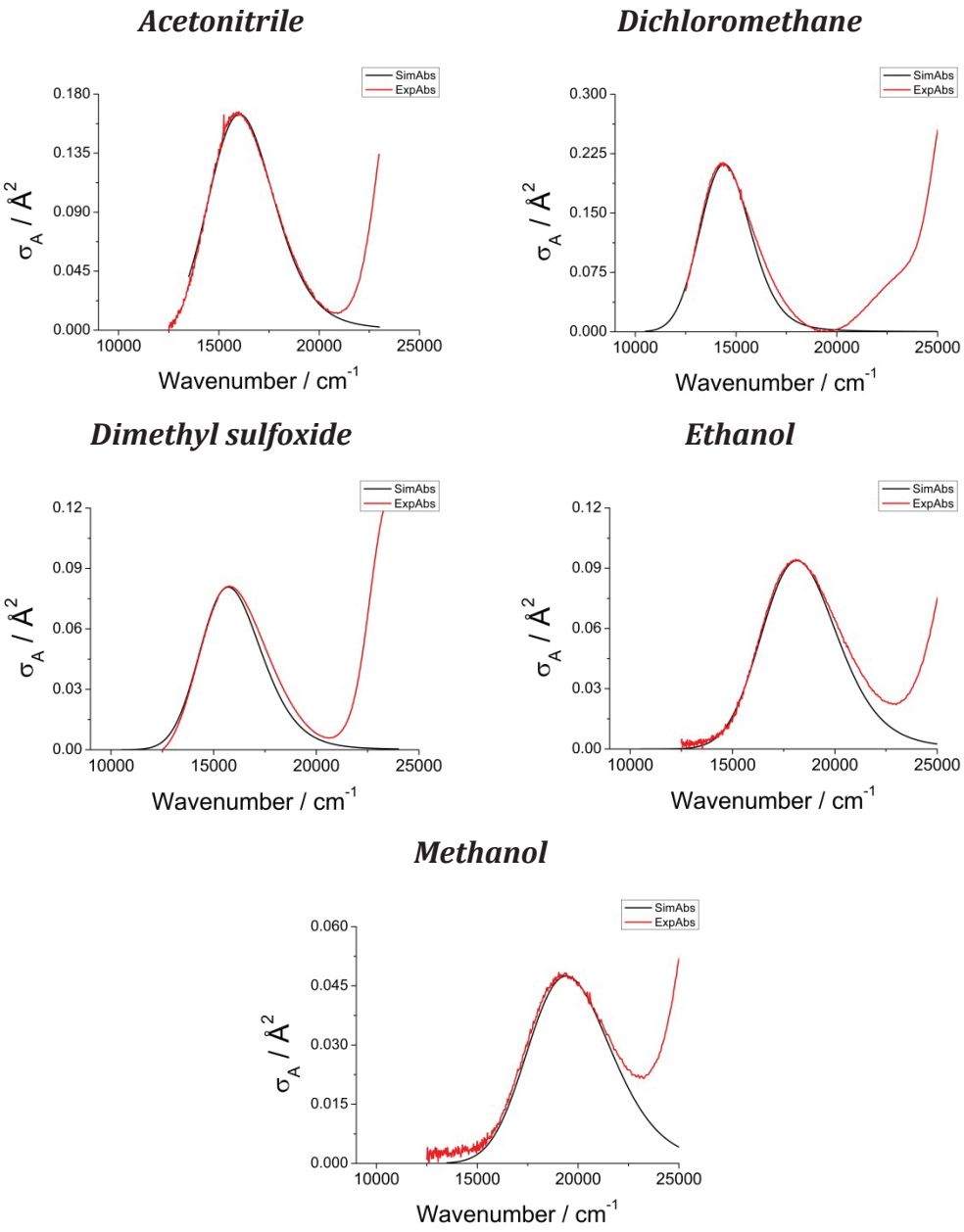


Figure 4.2 - Experimental and simulated absorption spectra of common organic solvents

The above spectra show both experimental and simulated absorption of Reichardt's dye in a selection of common organic solvents. From the above absorption spectra, and Figure 4.1, it can be seen that the position of the absorption maximum shifts as a result of changing solvent polarity, as would be expected based on the $E_T(30)$ scale, which is to be expected due to the solvatochromism of Reichardt's Dye. Figure 4.2 shows that the simulated data fits

the experimental data well at lower wavenumber (higher wavelength); however, as the wavenumber increases, and thus wavelength decreases, the simulations do not fit the absorption data as well. This is due to only one excited-state being used in this model. The inclusion of additional states would lead to better agreement between experimental and simulated spectra at higher wavenumber.

4.2 Reichardt's Dye resonance Raman Spectra and Computational Studies

4.2.1 Reichardt's Dye resonance Raman Spectra

The resonance Raman spectra were collected and treated as described in Chapter 2, sections 2 and 3.

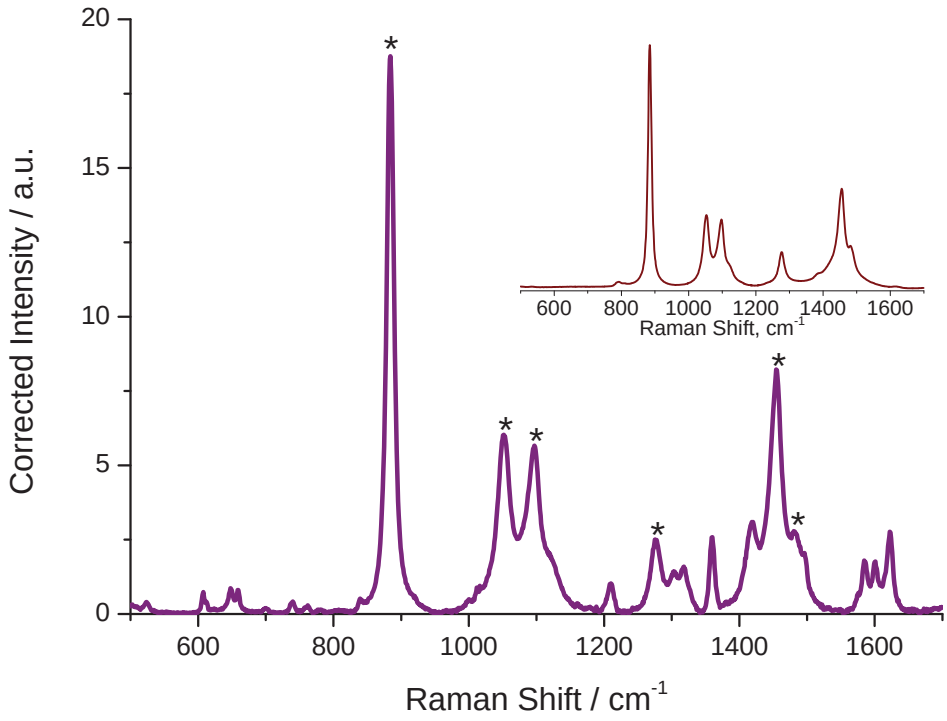


Figure 4.3 - Resonance Raman Spectrum of Reichardt's Dye in Ethanol, 532nm excitation; presence of * indicates solvent Raman modes. The inset shows the solvent Raman spectrum

Figure 4.3 shows a resonance Raman spectrum of Reichardt's Dye in ethanol (6.09×10^{-4} molL^{-1}), with a 532 nm excitation wavelength, the experimental details of which were described in 2.2.2.1. Table 4.1 on the following page, shows information on the vibrational modes of Reichardt's dye which have been

determined both experimentally and through DFT calculations. The solvent Raman spectrum of ethanol is shown in the inset. Comparing the solvent spectrum with the resonance Raman spectrum of Reichardt's dye in ethanol, a number of Reichardt's modes are able to be easily observed.

4.2.2 Reichardt's Dye Computational Studies

Results of the computational studies performed on Reichardt's Dye are shown in Table 4.1. Vibrational frequencies observed in the resonance Raman spectra were tentatively assigned to calculated modes. These assignments are shown in Table 4.1. These assignments were made through the comparison of experimental and calculated frequencies, and through qualitative consideration that resonance Raman modes which are strongly active should correspond to in-plane vibrations with high local symmetry.

Abbreviations have been used for describing mode assignments where appropriate. Figure 4.4 shows the labelling of the rings of Reichardt's dye. Py indicates the pyridinium ring in Reichardt's dye, while Px indicates the phenoxy ring. Ph indicates a phenyl ring, whilst subscripts indicate whether the phenyl ring is bonded to the pyridinium ring (written Ph_{Py}) or the phenoxy ring (written Ph_{Px}). Subscripts are used in the same manner when referring to single atoms. Symmetric stretches are indicated by symm str, whilst antisymmetric stretches are indicated by antisymm str. Minor contributions to the modes are included in brackets.

In the past, TD-DFT calculations have been performed on Reichardt's Dye in order to characterise the charge transfer transition. This has been qualitatively described as a $\pi \rightarrow \pi^*$ transition in which charge is transferred from a delocalized orbital including the phenolate fragment and smaller amplitude of the pyridinium ring to a π orbital on the pyridinium ring including the phenyl group in position 4.[45]

Table 4.1 - Mode information for Reichardt's dye in Ethanol

Theoretical frequency (cm^{-1})	Experimental frequency (cm^{-1})	Intensity	$(d\sigma/d\Omega)$ ($10^{12}A^2sr^{-1}$)	Optimized Δ value	Mode number	Calculated frequency (cm^{-1})	Mode assignment
605	608.0267	0.6095	9.37	0.200	54	606.8838	Local Ph ring bend
645	648.0897	0.7589	16.20	0.180	60	642.9555	Py, Px, Ph_{Py}, Ph_{Px} ring bend, Py torsion
1000	1012.734	0.2899	3.26	0.105	110	992.7705	Py (Ph_{Py}) antisymm str
1209	1209.659	0.9580	14.85	0.150	135	1184.349	C_{Px}-N str Py str
1295	1303.013	0.9828	32.14	0.155	145	1285.815	Px (Ph_{Px}) antisymm str
1320	1318.120	1.2375	30.56	0.120	152	1326.886	C_{Ph}-N str Py
1360	1359.651	2.5305	36.01	0.150	153	1339.567	Px (Ph_{Px}) symm str
1417	1417.985	2.4382	101.95	0.175	157	1429.775	Ph_{Px} antisymm str
1497	1496.150	1.0720	21.03	0.085	167	1496.227	Py Px antisymm str
1585	1585.034	1.5432	31.50	0.130	176	1587.925	Ph_{Py}, Py (Px) symm str
1602	1600.845	1.3783	31.76	0.130	177, 178	1588.771, 1589.771	Ph_{Px} symm str
1622	1622.241	2.6176	59.03	0.160	181	1599.289	Py, Ph_{Py} (Px) symm str

Note: The mode frequencies were scaled using an appropriate scaling factor prior to being assigned to specific Reichardt's Raman modes.[1] Abbreviations used here are explained in Section 2.2 of this chapter.

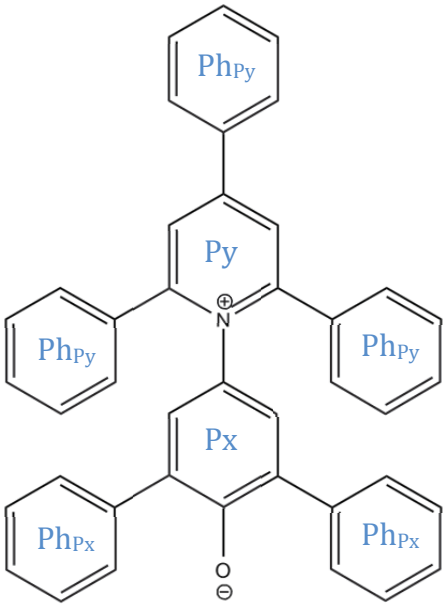


Figure 4.4 - Labelling of Reichardt's dye rings

The Kohn-Sham orbitals corresponding to the HOMO and LUMO were obtained from B3LYP/6-31+G(d) calculations, and are shown in Figure 4.5 and Figure 4.6. The HOMO-to-LUMO transition approximately describes the $\pi \rightarrow \pi^*$ charge transfer transition and resonance Raman intensities will be interpreted using this simple picture. After extensive literature review, a breakdown of transitions into one-electron (virtual-to-occupied) excitations has not been found to have been reported. Time-dependent DFT calculations will be carried out to provide a detailed analysis of the electronic transitions in future work.

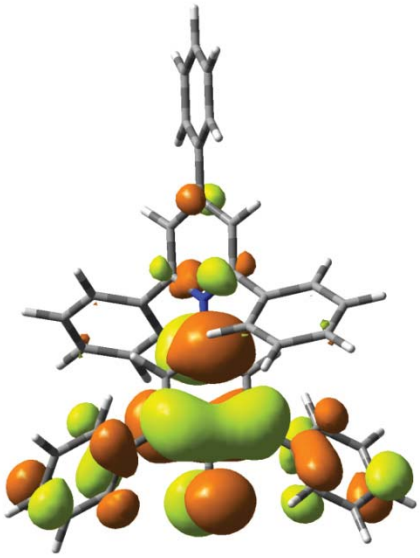


Figure 4.5 - Reichardt's HOMO; Mode 145

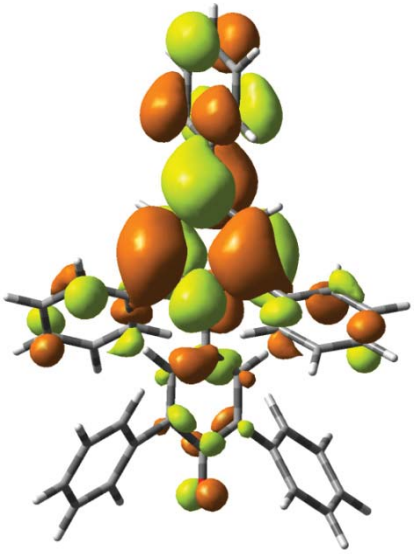


Figure 4.6 - Reichardt's LUMO; Mode 146

It was found that the Raman band at 605 cm^{-1} was best represented by mode 54 from computational studies. Mode 54 consists of local Ph ring bends, all to different extents. The local nature of ring bends means that each ring behaves as an independent oscillator, and does not have strong coupling to other parts of the molecule. Mode 54 is illustrated in Figure 4.8.

The Raman band of Reichardt's Dye at 645 cm^{-1} was found to correspond to mode 60. Modes 59 and 61 were considered, however, mode 60 is the most feasible, as it was found that modes 59 and 61 were not likely to correspond to the Raman band based on the HOMO and LUMO amplitudes. Mode 60 consists of Ph_{Py} and Ph_{Px} ring bending, in addition to Py and Px ring bending. There is also significant torsion within the structure. This torsion is associated with the Ph ring C which bonds to both the N and the Ph_{Py} rings. Large resonance Raman enhancement of torsion modes has also been shown to be present in dipyrrins.[63] The behaviour of mode 60 is demonstrated in Figure 4.8.

The assignment of mode 110 to the 1000 cm^{-1} Raman band was straightforward. It was found to be a Py antisymmetric stretch, with a contribution from Ph_{Py} antisymmetric stretch also.

The 1209 cm^{-1} Raman band corresponds to mode 135. This mode consists of a C_{Px}-N stretch, and a Py stretch, as is shown in Figure 4.8. Mode 136 was also

considered as a possible assignment, however it consists of a C_{Py}-C_{PhPy} stretch, which is not as likely to show significant enhancement.

When assigning the correct mode from the normal coordinate analysis to the 1295 cm^{-1} band in the Raman spectrum, it was found that mode 145 was the most appropriate assignment. Mode 146 (that associated with the LUMO structure of Reichardt's dye) was a Ph_{Py} antisymmetric stretch, however the rings with substantial vibrational amplitude were those which appear to have little contribution to the HOMO-LUMO transition, and so this mode was ruled out. The atoms that contribute to mode 145 also make a substantial electronic contribution to the HOMO. Figure 4.8 shows that mode 145 is predominantly a Px stretch. The HOMO extends over the Px ring and peripheral Ph rings. Due to this, creation of a hole in the HOMO should generate significant displacement (Δ) along mode 145. Mode 145 should experience significant enhancement because of this, as the mode intensity is proportional to Δ^2, and indeed this is the case, as shown in Table 4.1, mode 145 has a Δ of 0.155. A more detailed analysis of the effects of the solvent on the mode frequency of mode 145 is presented in Section 2.2.1 of this chapter.

Mode 152 was found to correspond to the 1320 cm^{-1} Raman band of Reichardt's Dye. This mode is interesting, in that it involves stretching between the substituted carbon on one Ph_{Py} ring, across to the nitrogen atom, and then onto the substituted carbon on the "opposite" Ph_{Py} ring, as is highlighted in Figure 4.7. A similar mode is also seen in conducting polymers[64-67], where it is used to analyse the distribution of charge carriers.

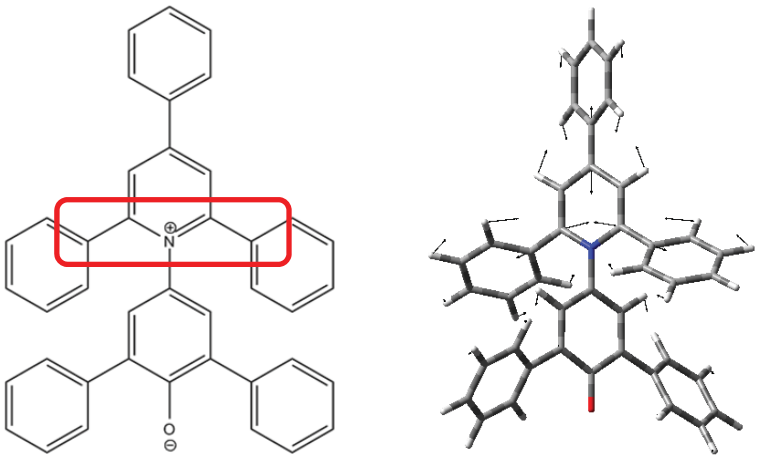
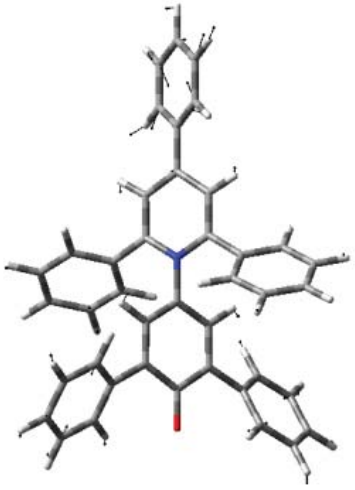
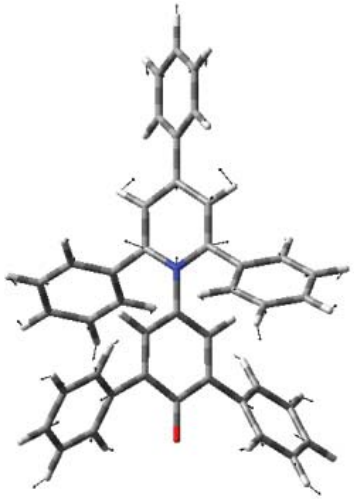


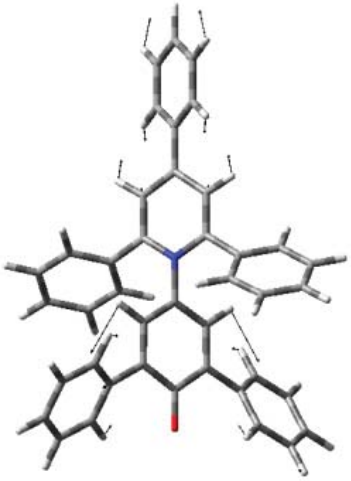
Figure 4.7 - Stretching across the nitrogen in Reichardt's Dye (Mode 152)

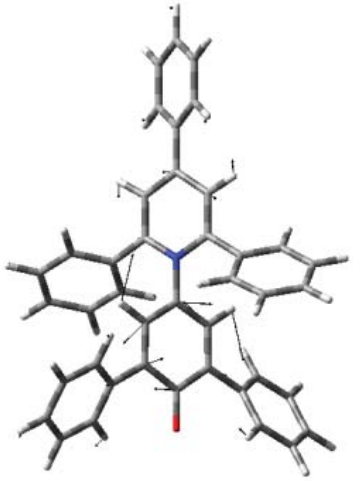
Mode 54, 605 cm^{-1} ***Mode 60, 645 cm^{-1}***



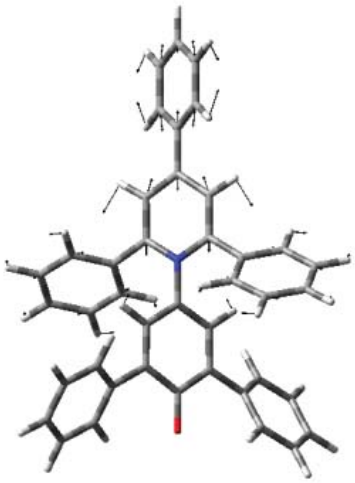


Mode 135, 1209 cm^{-1} ***Mode 167, 1497 cm^{-1}***





Mode 176, 1585 cm^{-1} ***Mode 178, 1602 cm^{-1}***



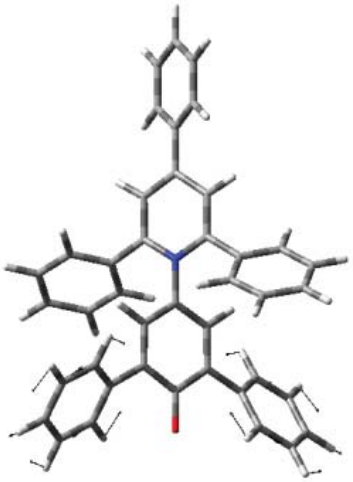


Figure 4.8 - A selection of vibrational modes of Reichardt's dye

Mode 153 was assigned to the 1360 cm^{-1} Raman band of Reichardt's Dye. This mode is a Px symmetric stretch, with a small contribution from (Ph_{Px}) symmetric

stretching. This is the purest Px mode, which has small coupling to the Ph_{Px}, leading to a large Δ value, as can be seen in Table 4.1. Mode 154 was not considered as an assignment for the 1360 cm^{-1} band as mode 154 does not involve those atoms that contribute to the HOMO or LUMO. It can be seen looking at Figure 4.9 that mode 153 corresponds to the HOMO and LUMO structure better than mode 154, as the ring stretching in mode 154 is not as likely to contribute to either the HOMO or LUMO structures as those in mode 153.

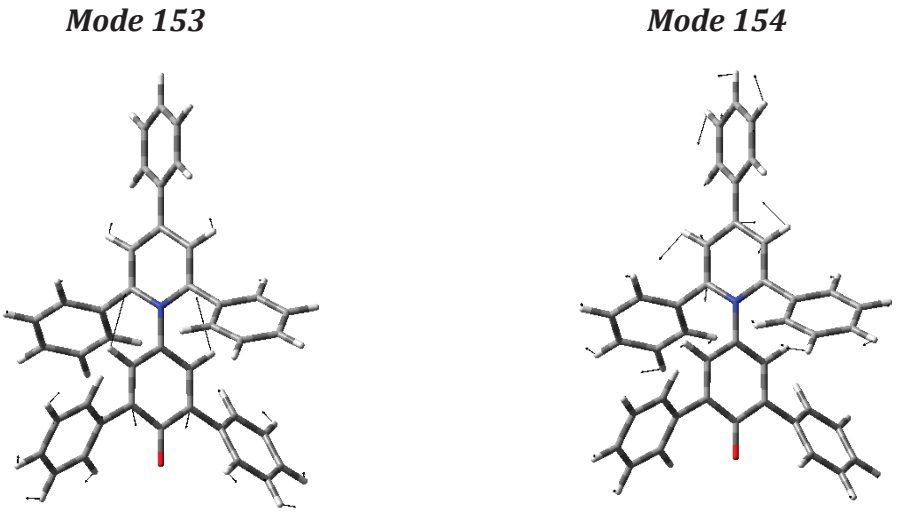


Figure 4.9 - Mode assignment for 1360 cm^{-1} Raman peak

The 1417cm^{-1} Raman band was found to correspond to mode 157. This mode consists of an antisymmetric Ph_{Px} stretch. It was found that no nearby modes would possibly contribute to the Raman spectrum, as mode 156 was too low in frequency to be a match, and 158 was a CH bend, which should not appear enhanced in a $\pi \rightarrow \pi^*$ transition.

Mode 167 was found to best correspond to the Raman band at 1497 cm^{-1}. This mode consists of significant stretching of Px and Py, which causes some stretching in both Ph_{Px} and Ph_{Py}. Modes 166 and 168 were also analysed in this case. Mode 166 consists of a CH bend, which should not appear enhanced in a $\pi \rightarrow \pi^*$ transition. Mode 168 shows a significant C-O stretch, but it is not likely to contribute to the Raman spectrum. Mode 167 is demonstrated in Figure 4.8.

It was found that mode 176 corresponded to the Raman band at 1585 cm^{-1}. This mode is a Ph_{Py} and Ph stretch, however, there is a small contribution from Px.

Mode 175 had too large a frequency shift from 176 in order to be considered as a potential corresponding mode for the 1585 cm^{-1} Reichardt's Dye Raman band. Mode 177 was not considered, as it is able to be associated with the 1602 cm^{-1} Raman peak. Mode 176 is demonstrated in Figure 4.8.

The Reichardt's Dye Raman band at 1602 cm^{-1} was found to correspond to modes 177 and 178. These modes were both found to correspond to symmetric stretching of the Ph_{Px} rings. Mode 179 was also considered, however, it was qualitatively decided it was unlikely to be enhanced based on the HOMO and LUMO amplitudes, and as such not likely to contribute to the Raman spectrum. Mode 178 is demonstrated in Figure 4.8.

Mode 181 was found to correspond to the 1622 cm^{-1} Raman band. Mode 180 was also found to be a possibility; however, this mode was comprised of a very large stretch of modes which are not expected to have a significant contribution to the HOMO-LUMO transition. Mode 181, on the other hand, comprises of Py, Ph_{Py}, and a small contribution of Px symmetric stretching.

Comparing the experimental, calculated, and theoretical frequencies for all the modes shown in Table 4.1 it can be seen that calculated and experimental frequencies at 605 cm^{-1}, 645 cm^{-1}, 1000 cm^{-1}, 1320 cm^{-1}, 1497 cm^{-1}, and 1585 cm^{-1} agree very well. The remaining bands show acceptable agreement although not as close as the first group.

4.2.2.1 Frequency Shift Analysis

The analysis of frequency shifts can give information on what is occurring in the molecule. The mode frequency is related to bond length, and thus is able to give information on bond character also. By analysing the frequency shifts of key modes in the Raman spectrum of Reichardt's dye we can get information on whether there is more bonding or anti-bonding character present in the dye. In order to perform this analysis, it was decided the shifts of the 1295 cm^{-1} Raman band would be analysed as a function of solvent.

Table 4.2 - Frequency shift analysis of the 1295 cm^{-1} Reichardt's Dye Raman peak

Solvent	Band position (cm^{-1})	Frequency shift (cm^{-1})
Acetonitrile	1291.24	-3.76
Dichloromethane	1291.96	-3.04
Dimethyl sulfoxide	1290.06	-4.94
Ethanol	1301.68	+6.68
Methanol	1303.30	+8.30

In Table 4.2, frequency shifts have been calculated using a value of 1295 cm^{-1} as the true band position. All band positions have been given from the Raman spectra collected at an excitation wavelength of 647nm.

It can be said that there is more anti-bonding character if the frequency shifts are negative, as bonds are getting weaker. The significant frequency shifts that are shown in Table 4.2 indicates that there are solvent polarity effects on the ground-state electronic structure.[38] From this, a relationship between solvent polarity and frequency shift is expected. With the exception of dichloromethane, the frequency shifts are able to be related to increasing solvent polarity. The most polar solvent of the five, methanol, shows a shift to the highest frequency, followed by ethanol, the next most polar. Acetonitrile should follow, then dimethyl sulfoxide, however, this is not quite the case. The differences in the shifts not being significant may be the reason these shifts do not follow solvent polarity as expected.

Another property of interest in the analysis of frequency shifts is the determination of the Mean Absolute Deviation (or MAD), which gives an indication of the quality of the computational study. MAD is able to be used as an indication of the confidence in the mode assignments. This is given by:

$$MAD = average\left(\left|\omega_{exp} - \omega_{calc}\right|\right)$$

where ω_{exp} is the experimental frequency of the resonance Raman vibrational mode, and ω_{calc} is the scaled calculated frequency of the vibrational mode obtained through computational studies. In this case, the MAD for this data set was found to be 12.19. This value is reasonable,[60] and is affected by a few modes which

have quite large values of $|\omega_{exp} - \omega_{calc}|$, and as such increases the value of MAD significantly.

4.2.3 Resonance Raman Spectra of Reichardt's Dye in Common Organic Solvents

Figure 4.10 shows a selection of resonance Raman spectra obtained as a part of this study. The resonance Raman spectra shown were collected and treated as described in Chapter 2, sections 2 and 3. A total of 49 resonance Raman spectra of Reichardt's dye in this selection of common organic solvents were obtained, however, only a selection have been shown here for illustration.

Looking at the resonance Raman spectrum of Reichardt's dye in acetonitrile at 488nm excitation in Figure 4.10 a), it can be seen that some Reichardt's peaks are easily visible, particularly those at 1602 cm^{-1} and 1622 cm^{-1}. The spectrum of the same sample at 594nm excitation has also been shown in Figure 4.10 b). This spectrum contains more background influences than the data for 488nm. This is somewhat problematic, as peak areas calculated for less intense Reichardt's peaks may not be as accurate as if the spectrum did not have these background influences.

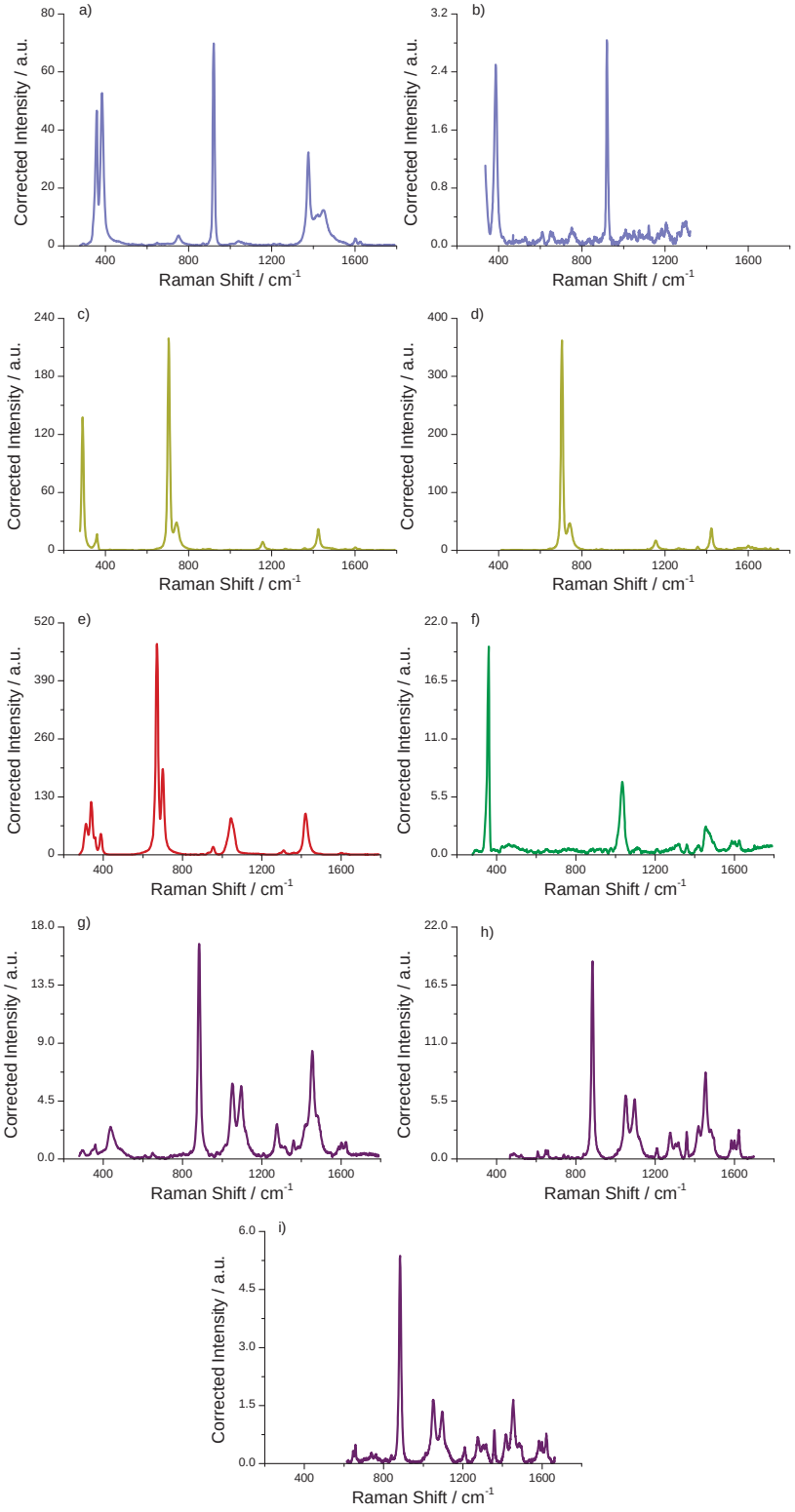


Figure 4.10 - Resonance Raman Spectra of Reichardt's Dye in common organic solvents. a) MeCN 488nm; b) MeCN 594nm; c) DCM 488nm; d) DCM 514.5nm; e) DMSO 488nm; f) MeOH 488nm; g) EtOH 488nm; h) EtOH 532nm; i: EtOH 568nm.

Looking at Figure 4.10 c) and d), it can be seen that there are not many Reichardt's peaks easily visible in the spectra. This is due to the intensity of the

solvent bands associated with dichloromethane, which are much larger than those of the Reichardt's dye bands. Looking carefully, however, there is a small peak visible around 1602 cm^{-1}.

Due to the significantly decreased intensity of the dye peaks with respect to the solvent peaks, it is much more difficult to accurately fit peaks to the dye modes, as many of the peaks fitted to the solvent modes may overlap, causing an artificially small apparent contribution from the Reichardt's mode. This leads to uncertainties being present in any calculations associated with this solution, as any results may be subject to artificial influences from solvent modes.

A spectrum of Reichardt's dye in dimethyl sulfoxide is shown in Figure 4.10 e). As with for dichloromethane, it is very difficult to see Reichardt's dye peaks in the Raman spectrum. In this case, however, the Reichardt's peaks are even less visible than in dichloromethane. This, again, leads to uncertainty in any peak areas obtained through peak-fitting processes due to the solvent modes being so intense.

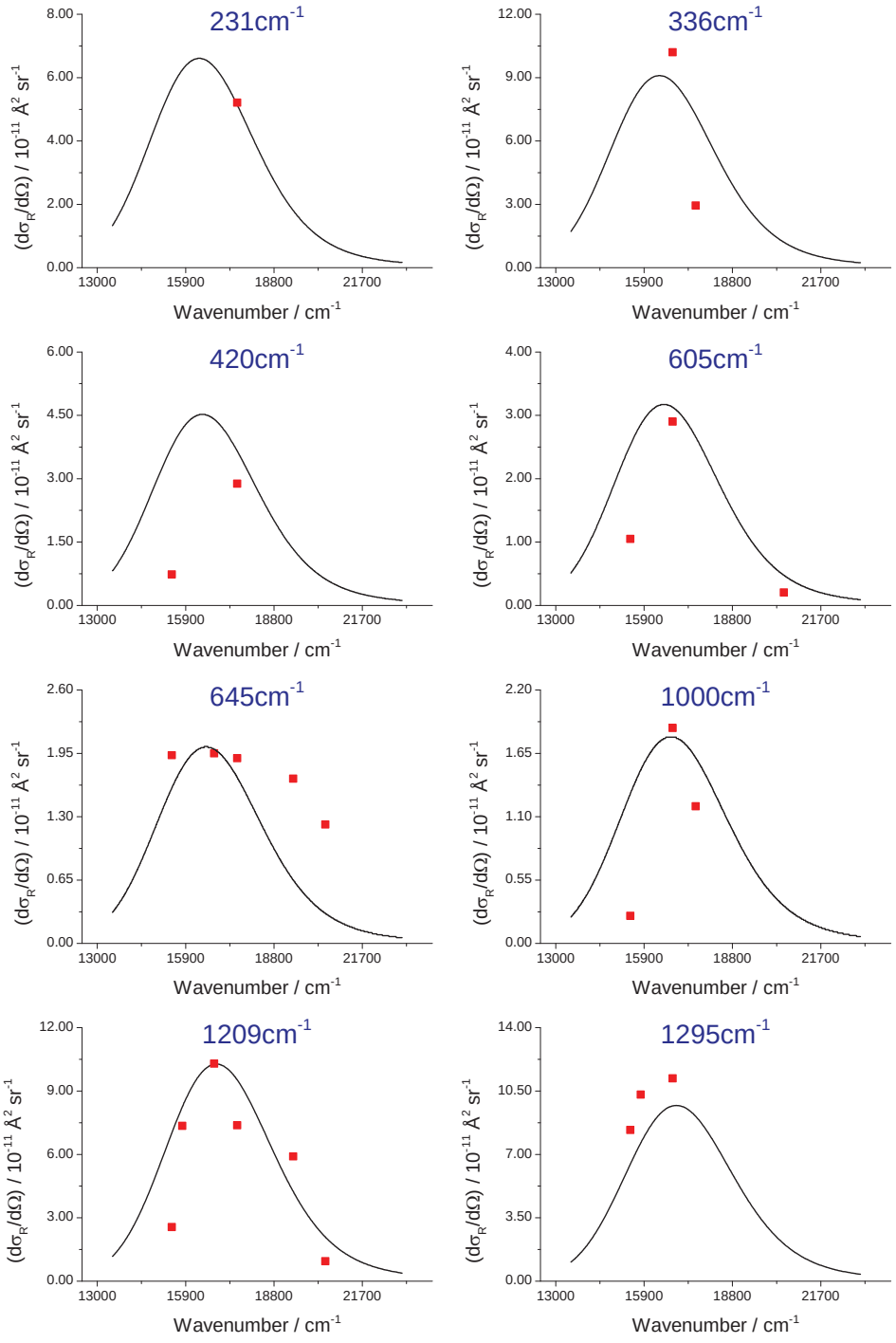
In the Raman spectrum of Reichardt's dye in methanol shown in Figure 4.10 f) it can be seen that the Reichardt's modes are more visible than in dichloromethane and dimethyl sulfoxide. This leads to more accurate representations of what is occurring with respect to Reichardt's dye in this solution, which in turn means that modelling will give a more accurate representation of the properties of this solvent than is possible for dichloromethane or dimethyl sulfoxide.

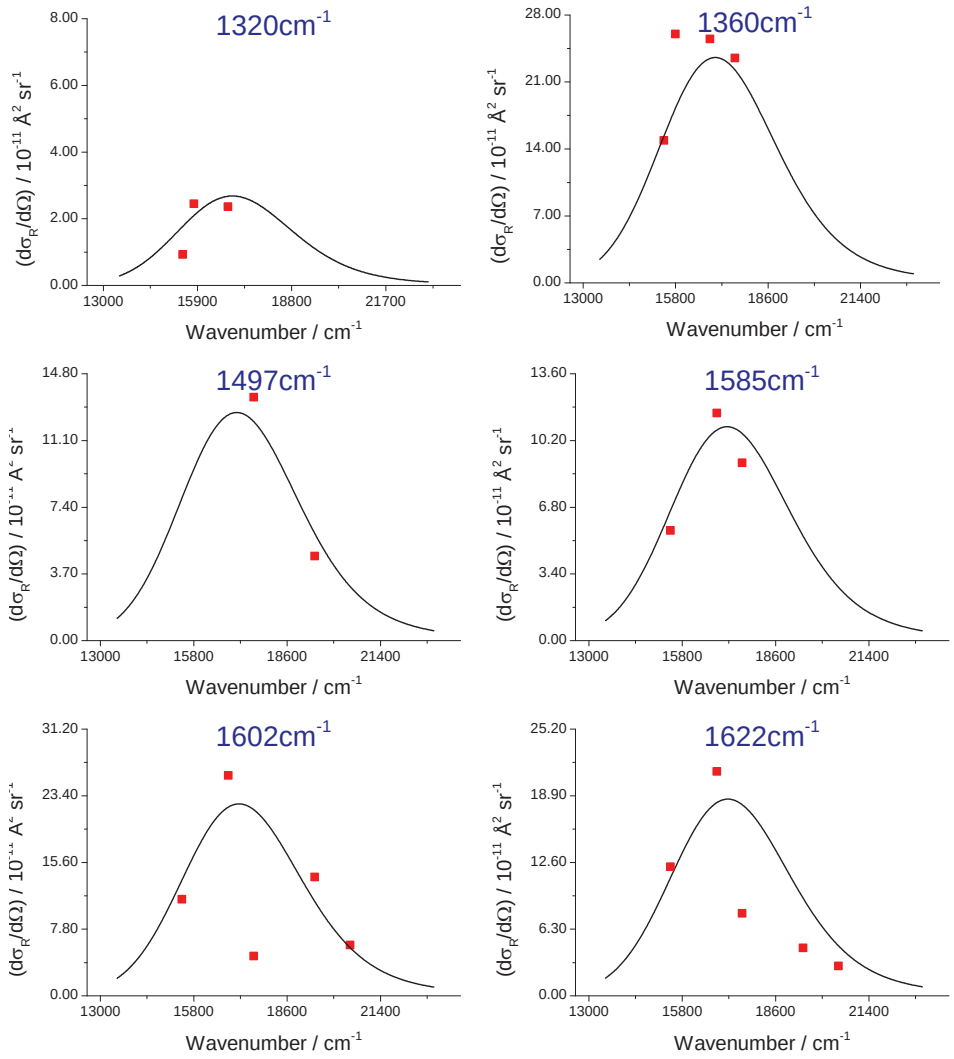
Three Raman spectra of Reichardt's dye in ethanol are shown in Figure 4.10 g)-i). It can be seen that for this sample the Reichardt's dye modes are very clearly visible. This is due to the intensity of the solvent peaks for ethanol being a lot less with respect to the Reichardt's modes than in the cases of dichloromethane or dimethyl sulfoxide. This means that peak fitting for this solution (i.e. Reichardt's in ethanol) should not be greatly influenced by the solvent modes. This is desirable, as this solution should be able to give a very accurate representation of the Reichardt's dye properties. Comparing the three spectra, it can be seen that Reichardt's peaks have different intensities at different excitation wavelengths.

4.3 Reichardt's Dye Modelling

The modelling was performed as stated in Chapter 2, Section 4. The profiles were prepared using Raman spectra of a solution of Reichardt's dye in a selection of common organic solvents. The values of the electronic origin, transition dipole length, and homogeneous broadening used to prepare each of these profiles are listed in the summary table at the end of this section.

4.3.1 Reichardt's Dye in Acetonitrile





The above profiles, and those shown in following sections, were prepared using absorption and Raman spectroscopic data as described in Chapters 2 and 5. The experimental data is represented by the red data points, whilst the simulated Raman profiles for the individual Reichardt's modes are shown by the black lines.

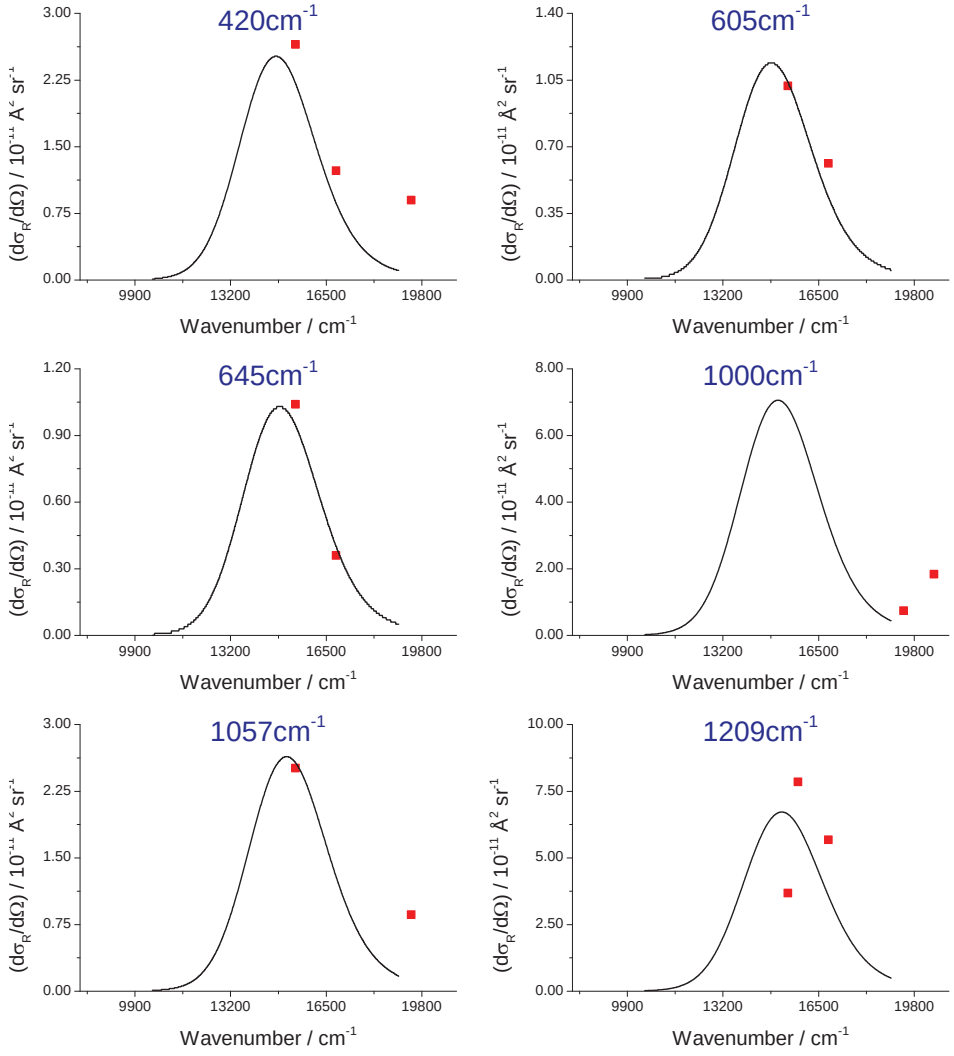
It can be seen, for this data set, that whilst many of the experimental data points fit the simulated profiles well, there are exceptions where the experimental and simulated data do not agree. As in this case the majority of these discrepancies are small, they are most likely due to slight inaccuracies in the peak fitting process which is used for the determination of differential Raman cross-sections for each of the modes.

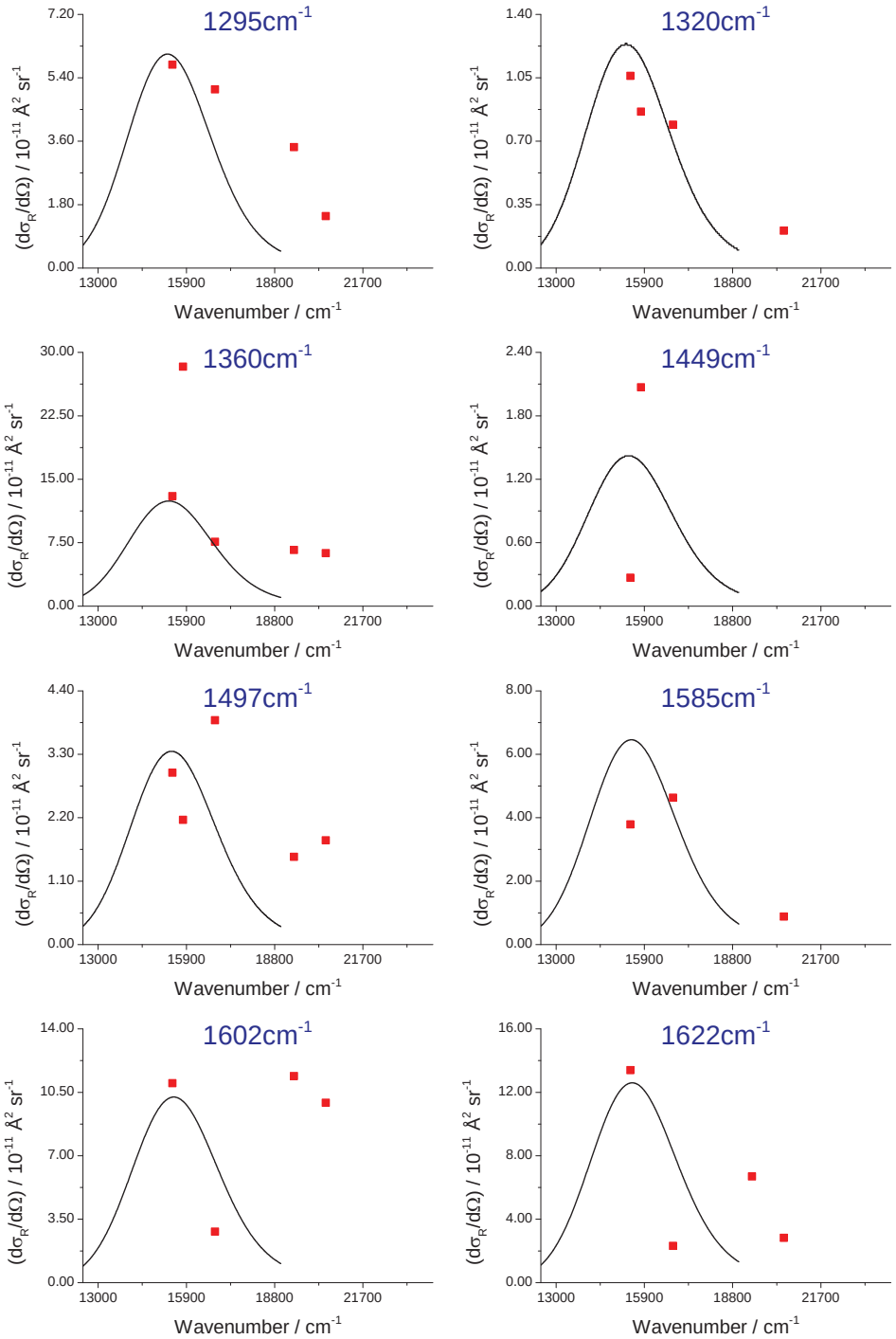
When modelling Raman profiles, decisions must be made as to the significance of data points with respect to giving specific data points more or less "weight". For this data set, many of these decisions were simple, for example with the data for

the 1000 cm^{-1} mode. The 594 nm data point was given more significance as it provided the most accurate cross-section value for this mode. This accuracy was assessed in a qualitative sense by analysing the peak fitting which was performed at each of the wavelengths for which the 1000 cm^{-1} was visible in the Raman spectrum, and finding that the fit for the 594 nm laser line was the more accurate of the fits. The same process was undertaken for each mode, so as to determine which of the data points would be the focal point of the modelling process.

Due to the intensity of the solvent bands in the Raman spectra being larger than desirable, there may be some error in the fitted peaks areas and hence cross-sections and thus profile generation. After inspection of fitted Raman spectra, however, this does not appear to be likely, as all solvent peaks of interest look to be well modelled by the Origin fitting function.

4.3.2 Reichardt's Dye in Dichloromethane





The above profiles, and those on the previous page, were prepared as described for acetonitrile. The treatment procedures, in terms of choice of the most accurate experimental data points, were also followed as for acetonitrile.

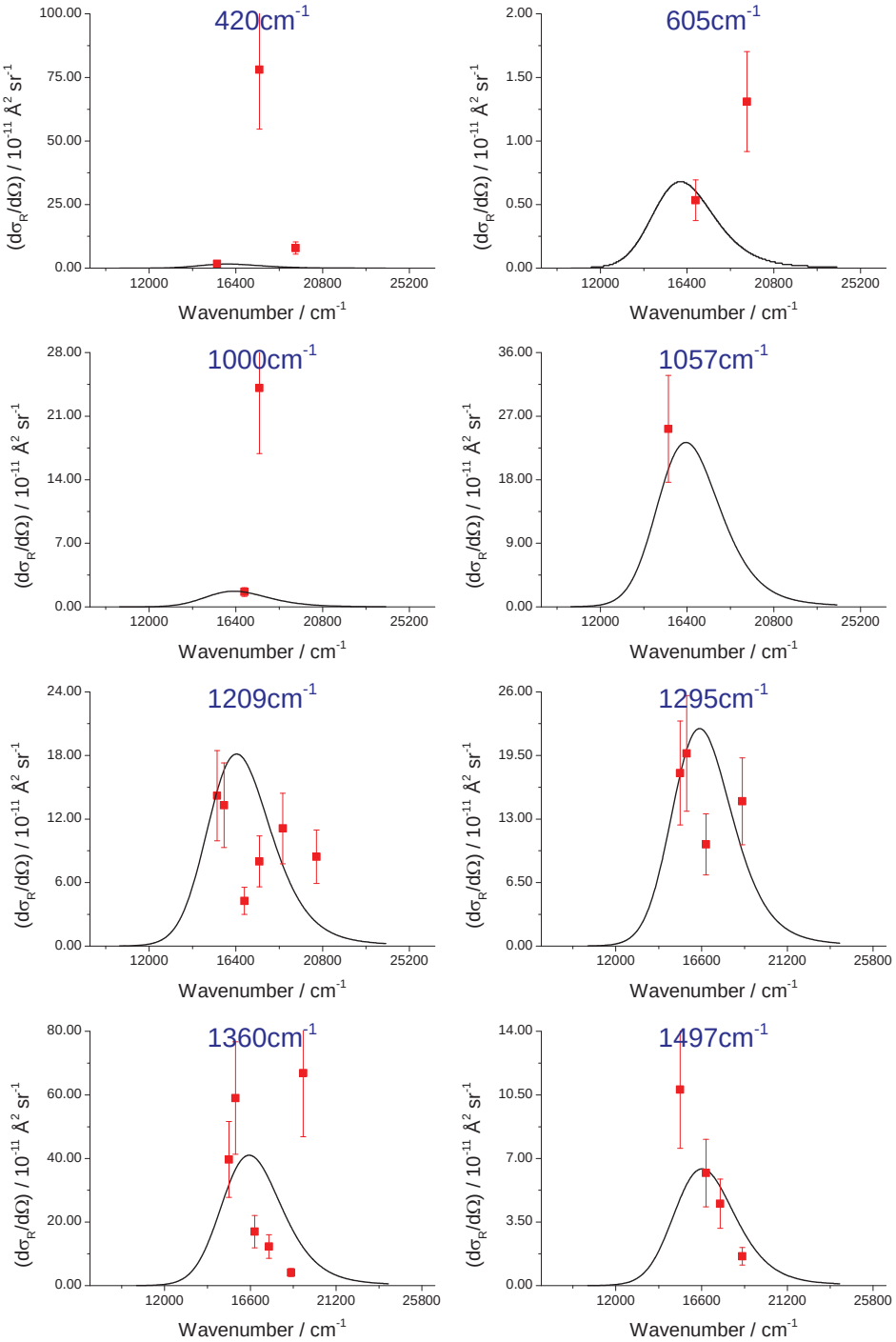
Through the analysis of the experimental data, it was found that the differential cross-sections calculated for 488 nm and 514.5 nm excitations were not within the

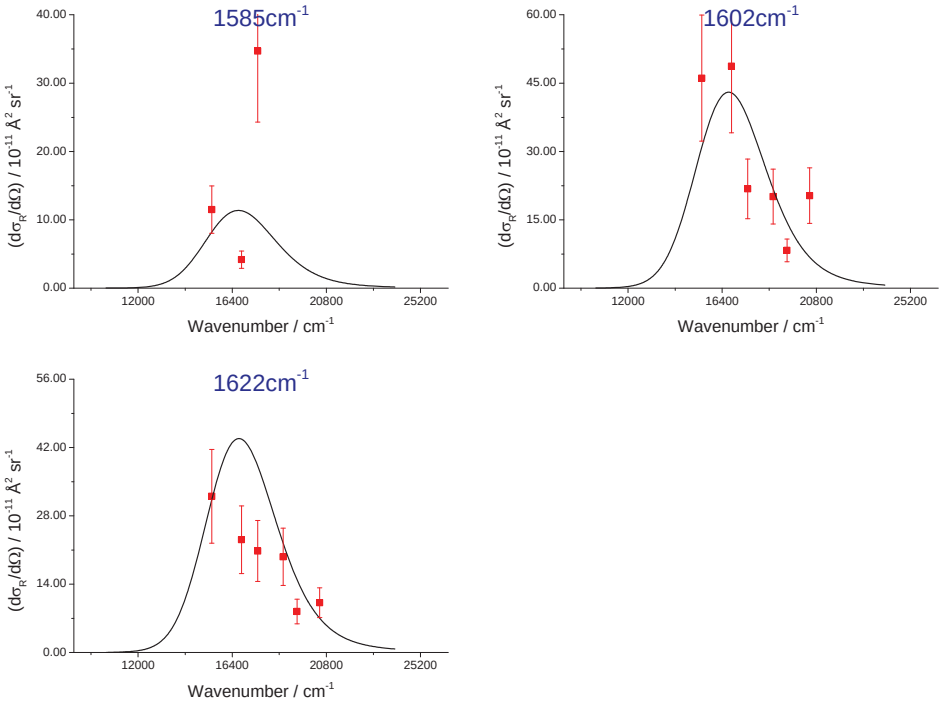
expected range, if compared to the cross-sections obtained with the other excitation wavelengths. After close inspection of the fitted Raman spectra, it was decided that the reason for these discrepancies was incorrect fitting of Raman sample spectra. Although an attempt to account for this was made, and these data sets were fitted again, it was found that the quality of the spectra simply did not allow for the accurate calculation of these cross-sections. This was due to the large intensity of the solvent peaks with respect to the intensities of Reichardt's dye mode peaks. As these spectra were taken at a wavelength that was not close to the absorption maxima, the resonance enhancement of these Reichardt's modes was not significant to overcome the intensity of the solvent peaks. As such, it was decided that the simulated profiles for Reichardt's dye modes would be based off of, wherever possible, the data from wavelengths closest to resonance.

With a few exceptions, the majority of the simulated profiles are in agreement with the experimental data points. One noticeable exception is the profile generated for the 1449 cm^{-1} Reichardt's dye mode. The simulation of this profile was difficult, as neither of the two fitted spectra stood out as being either very good or very bad fits to the data. The relative intensity of this mode to the solvent modes was simply too small to accurately fit the data, and as such, a best estimate of the position of the profile was made. It was decided that, even though this is not the most accurate method of fitting this mode, due to time constraints it was sufficient to model the solvent properties, and would give a more accurate representation of the sample than if this mode was simply ignored in the simulation process.

Whilst almost all of the profiles were able to be accurately simulated based on near-resonance Raman data, the 1000 cm^{-1} mode did not have sufficient intensity to be fitted when probed with near-resonance laser wavelengths. As such, the profile for this mode was again estimated for the same reasons as stated above for the 1449 cm^{-1} mode.

4.3.3 Reichardt's Dye in Dimethylsulfoxide





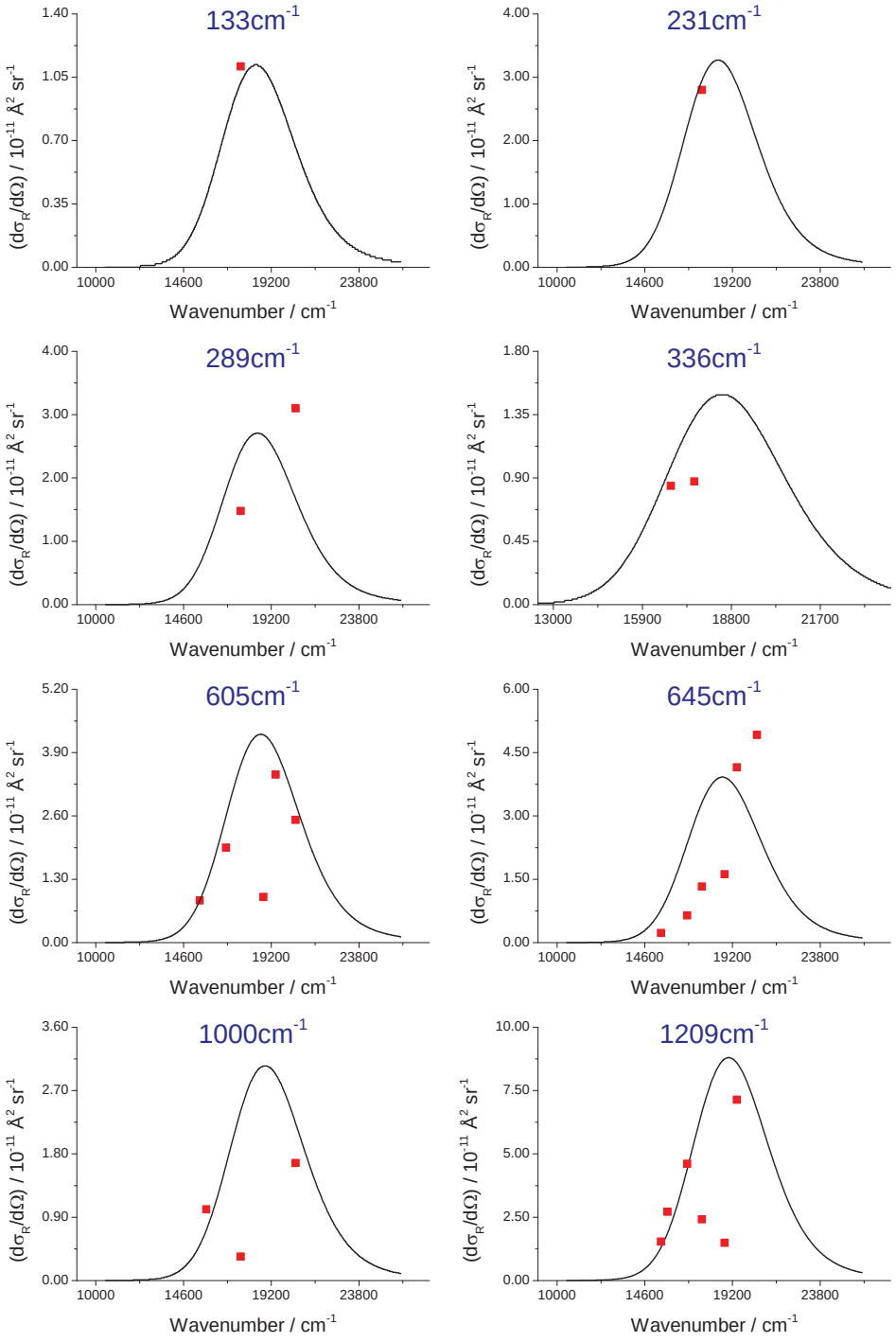
The above profiles, and those on the previous page, were prepared as described for acetonitrile. The treatment procedures, in terms of choice of the most accurate experimental data points, were also followed as for acetonitrile.

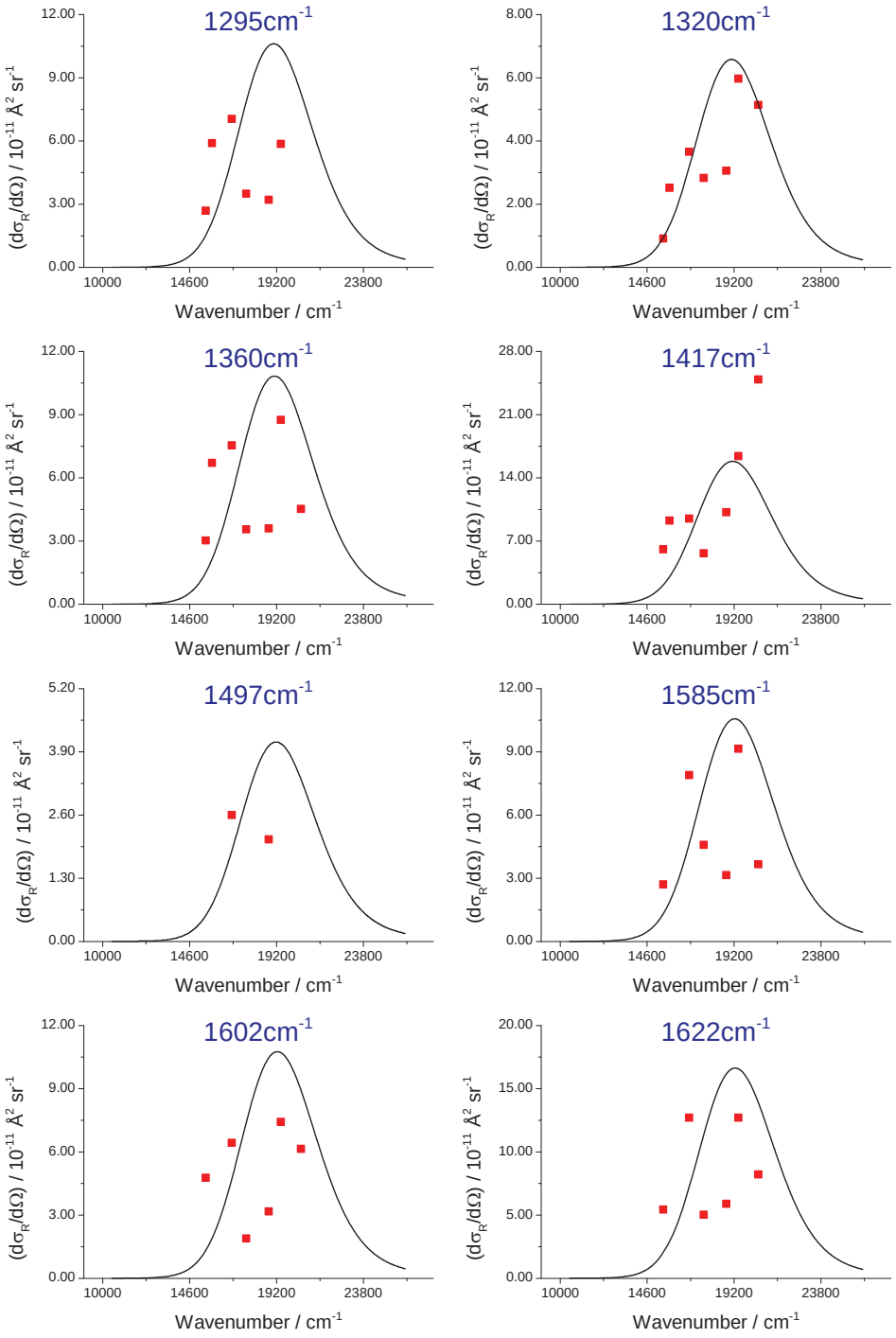
Error bars have been included for this data set, which represent a 30% error on the experimental differential cross-sections for each of the Reichardt's dye modes. This error is present purely due to the intensity of the solvent peaks being very large with respect to the Reichardt's modes in resonance Raman spectra, leading to accurate determination of peak areas being more difficult. This leads to the potential of miscalculation of solvent properties, due to a lack of accuracy of data; however, measures have been taken to ensure that data analysis and simulation have not been significantly influenced by these uncertainties.

Whilst the profiles for 420 cm^{-1}, 605 cm^{-1}, and 1000 cm^{-1} are shown with a large y-axis scale so that all recorded data points are visible, these larger data points, i.e. the 420 cm^{-1} and 1000 cm^{-1} peak at 568nm excitation, the 605 cm^{-1} peak at 514.5nm excitation , were generally ignored when undertaking simulations of Raman profiles. During the simulation process, if these data points were included when adjusting delta's to change the intensity of the profile, the delta values required to cause a large enough change in profile intensity were unrealistically

large. As such, it was decided to ignore these data points due to their being so much larger than the other experimental points. Due to the presence of the error bars, when adjusting the profile parameters, every effort was made to include as many of these error bars (if not the data points themselves) in the profile. This procedure was used so as to reduce the potential of miscalculation of solvent homogeneous broadening.

4.3.4 Reichardt's Dye in Ethanol





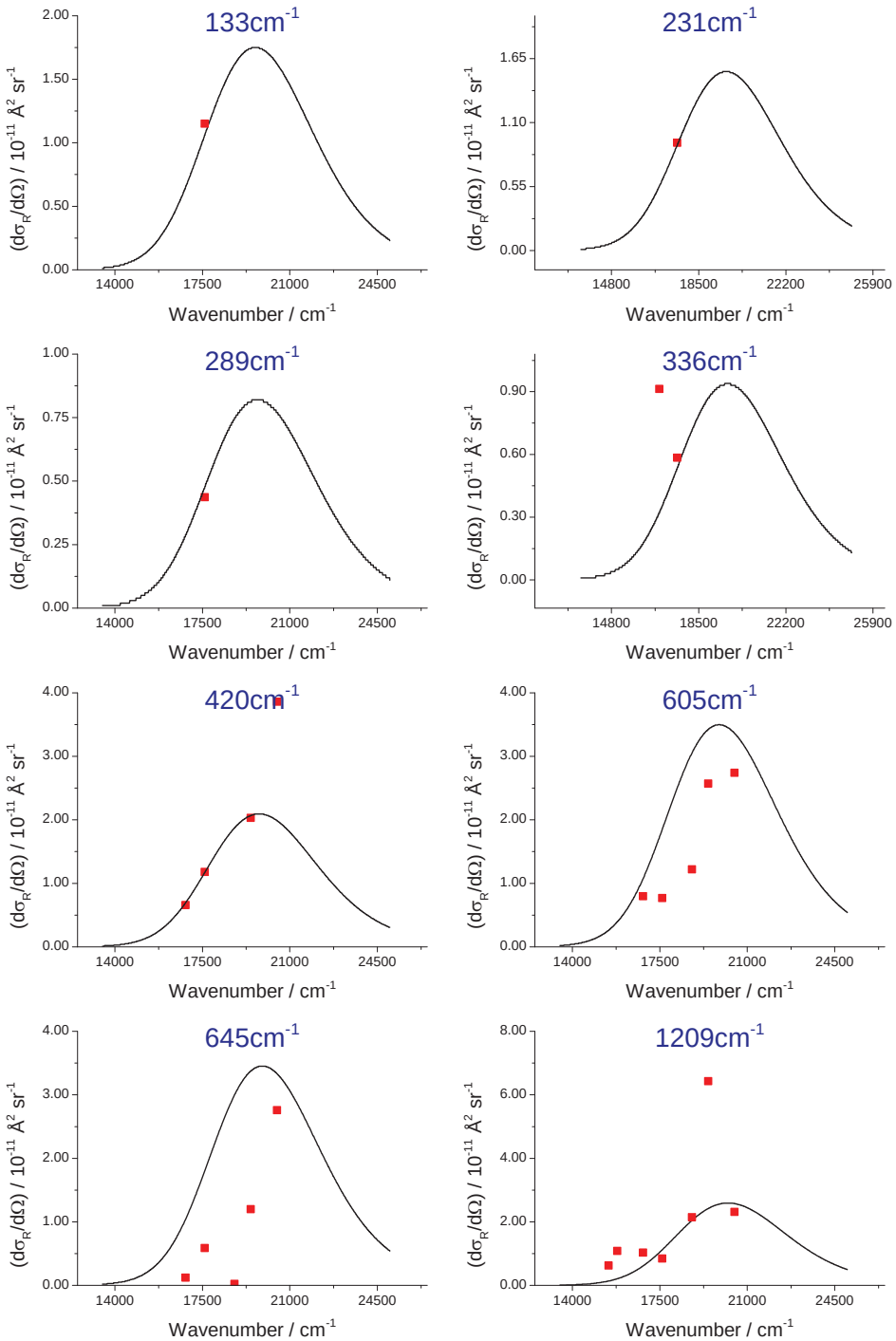
The above profiles, and those on the previous page, were prepared as described for acetonitrile. The treatment procedures, in terms of choice of the most accurate experimental data points, were also followed as for acetonitrile.

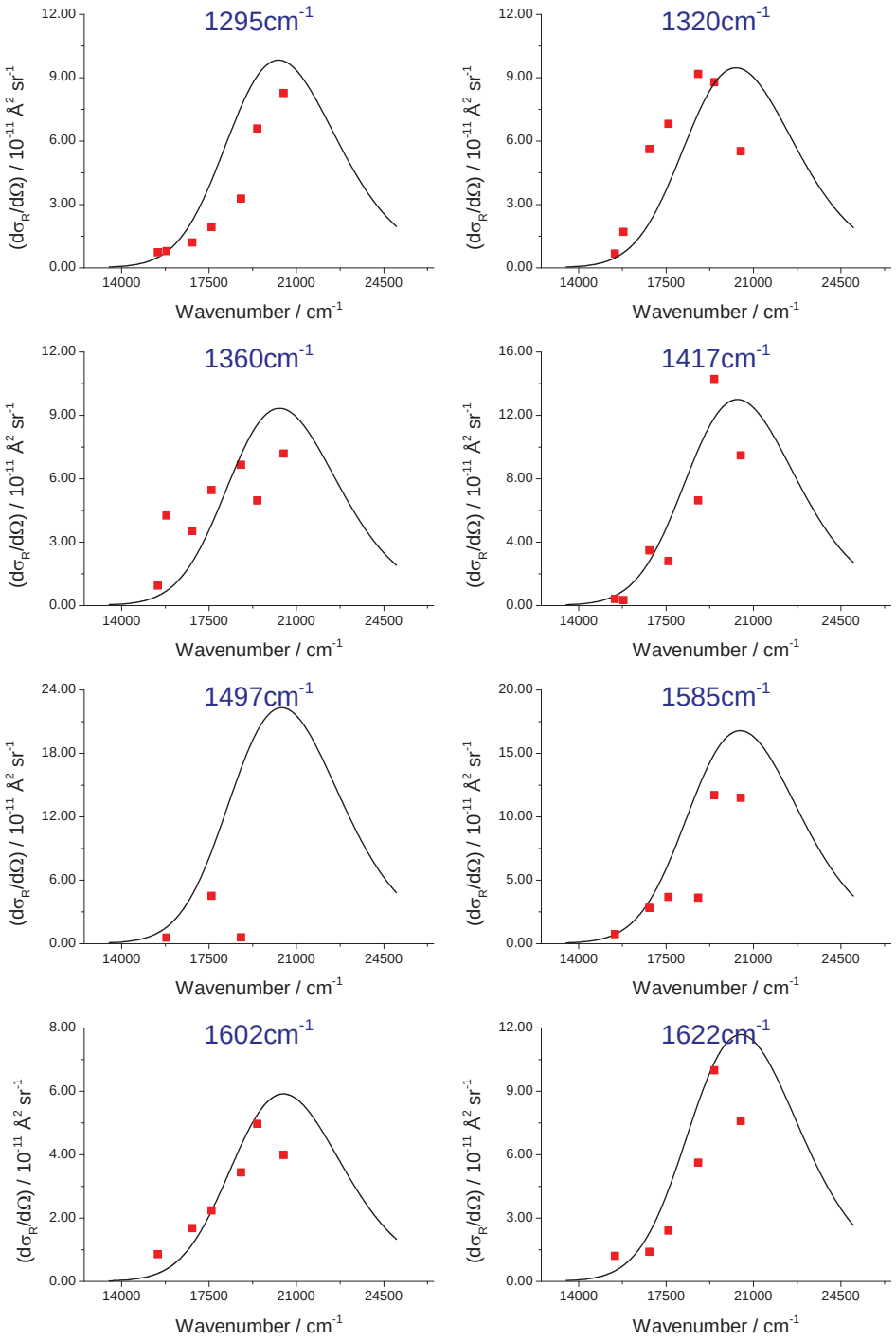
It can be seen that the profiles generated for this sample generally contain more experimental data points than those prepared for Reichardt's dye in acetonitrile, dichloromethane, or dimethyl sulfoxide. This is due to the solvent peaks of ethanol being less intense relative to the Reichardt's modes, thus leading to the ability to more accurately fit the Raman spectrum, and, as such, more accurately calculate values of differential cross-sections.

Although this data set allows for the determination of information for more modes, and at a greater range of wavelengths, it was found that the data acquired at 532 nm and 568 nm does not appear to fit the simulated profile as well as that acquired at other wavelengths. Upon further analysis, it was found that this discrepancy was most likely due to the baseline present at these wavelengths. Whilst other wavelengths studied had similar wavelengths to each other, these two wavelengths appeared to have different wavelengths to what was considered standard for this data set. As such, it was decided that values would be calculated with the standard baseline profile being subtracted from the data, but that the data would not be included when adjusting profile parameters.

If ignoring the data acquired at 532 nm and 568 nm for the reasons stated above, the agreement between the simulated profiles and the experimental data points appears to be very good for the majority of the modes. Analysing the agreement for the higher modes, it can be seen that there is a slight discrepancy between the position of the experimental data points and that of the simulated profile, as though one appears to be shifted horizontally. If this is accounted for the simulated and experimental Raman spectroscopy data agree to a larger extent, however, we are not modelling only the Raman data. The absorption spectrum for the sample is also very important for this process, and it was decided that for this data set it was more important to ensure an accurate fit to the position of the absorption profile, which is known with much greater accuracy, than the simulated Raman profiles.

4.3.5 Reichardt's Dye in Methanol





The above profiles, and those on the previous page, were prepared as described for acetonitrile. The treatment procedures, in terms of choice of the most accurate experimental data points, were also followed as for acetonitrile.

As with the profiles calculated for ethanol, the profiles for Reichardt's dye in methanol are much more accurate than those calculated for the other common

organic solvents used in this study. This is, again, due to the less intense solvent Raman spectra giving the ability to better fit and calculate data for Reichardt's modes.

The simulated profiles for methanol fit the experimental data with the best agreement of any of the common organic solvents used in this investigation. There are still small discrepancies between the simulated and experimental data; however, these are not of great concern in terms of the estimation of solvent parameters from the data.

4.3.6 Results of Reichardt's Dye Modelling in Common Organic Solvents

Table 4.3 below shows the electronic origin, homogeneous broadening, and transition dipole length which have been calculated based on fitting simulated Raman profiles to experimental data points.

$$\lambda_S = 0.5\beta \left(\frac{R_\lambda}{R_\mathrm{K}}\right)^2$$

where β is simply $1/k_B T$, k_B is Boltzmann's constant, R_K is the stochastic line shape parameter, defined in Chapter 2, and

$$R_\lambda = \frac{R_\mathrm{K}\Gamma}{a}$$

where Γ is the homogeneous line width (homogeneous broadening), and

$$a = \frac{2.35 + 1.76R_\mathrm{K}}{1 + 0.85R_\mathrm{K} + 0.88{R_\mathrm{K}}^2}$$

A value of λ_S can be easily calculated for any value of Γ, which is the only parameter which is not a constant in these equations.

Table 4.3 - Electronic properties of common organic solvents from modelling of absorption and Raman profiles

	Electronic Origin (cm^{-1})	Homogeneous Broadening (cm^{-1})	Reorganization Energy (cm^{-1})	Transition Dipole Length (Å)
Acetonitrile	11000	3370	5141	0.780
Dichloromethane	11200	2720	3349	0.840
Dimethyl Sulfoxide	11850	2900	3807	0.550
Ethanol	12100	3680	6130	0.591
Methanol	12680	3700	6197	0.423

Several methods exist in the literature for both calculating and experimentally determining reorganization energies. Some previously calculated values are shown in Table 4.4.

Table 4.4 - Reorganization energies of a selection of common organic solvents, from literature

	Experimental Estimates			Theoretical Estimates			
	Kjaer[68]	Barbara[69, 70]	Zong[30, 31]	Δμ/μ[36]	Perng[71]	Maroncelli INDO[36]	Maroncelli two-site[36]
Acetonitrile	1660	2221	6020	1510	790	4260	2570
Ethanol	2170	3900	-	2150	-	3070	3560
Methanol	2140	-	5835	2510	2930	3570	3900

Kjaer and Ulstrup[68] determined reorganization energies experimentally using the solvatochromic absorption band for the Betaine-26 dye (2,4,6-triphenyl-*N*-(di-*tert*-butyl-4-hydroxyphenyl)pyridinium in a range of polar, apolar, protic, and aprotic solvents. Through bandshape analysis, it was found that specific interactions, including hydrogen bonding and possibly solvent libration, accounted for many of the observed band features for the solvents studied, however, more detailed studies would be required in order to obtain further details on this.

Barbara et al[69, 70] studied reorganization energies of a range of solvents through the investigation of electron-transfer and back-electron-transfer kinetics of Reichardt's dye. In order to test the accuracy of results, the back-electron-

transfer kinetics[69] were compared to predicted rates from the Walker et al model[70], and it was found the agreement was very good.

Zong and McHale[30, 31] studied Raman excitation profiles for a selection of vibrational modes of Reichardt's dye in a variety of solvents. These profiles were modelled using wavepacket theory, in order to give experimental values of solvent reorganization energies.

Mente and Maroncelli[36] determined reorganization energies theoretically and computationally using both an INDO and two-site method. For both of these methods, it was assumed the solvent effect on the absorption spectrum of Reichardt's dye comes from electrostatic interactions between the effective charge distributions of solvent molecules, and the charge shift caused by excitation from the ground to excited state. The two models were used in order to model the charge shift. The two methods gave differing results of reorganization energies. In addition to this, they found the linear response estimate (Δμ/μ) using the equation:

$$\lambda = \frac{\Delta E_T}{2}\left|\frac{\vec{\mu}_1 - \mu_0}{\vec{\mu}_0}\right|$$

This equation assumes the dipole moment determines the solvation energy of the solvent. These methods use fairly simple models which work for bulk liquids. These are important, as they provide a theoretical method that can be checked using experimental data.

Perng et al[71] studied the energetics of charge transfer reactions in dipolar and nondipolar solvents theoretically. Using simple models they found that the solvatochromic effect on the absorption energy of Reichardt's dye was able to be reproduced reasonably well by the renormalized site-density theory (RST), renormalized dielectric theory (RDT), and simple harmonic approximation (HXA) theories for a range of solvents varying in polarity from carbon tetrachloride to water.

It can be seen, from comparing the literature values in Several methods exist in the literature for both calculating and experimentally determining reorganization energies. Some previously calculated values are shown in Table 4.4.

Table 4.4 to the values of reorganization energies determined in this study, shown in Table 4.3, that there are similarities between some literature values, but that these literature values vary significantly based on the method used. As such, it is impossible to clearly state whether the results from this study agree with literature, however, it can be said that they agree to a reasonable extent with selected studies in the literature, namely those by Zong[30], and to a lesser extent with those by Maroncelli[36].

Chapter 5 – Reichardt's Dye in Ionic Liquids

5.1 Reichardt's Dye Absorption Spectra

The absorption spectra of Reichardt's dye in common solvents were collected using a Cary 100 Bio spectrophotometer (Varian Inc.) with 1cm quartz cuvettes.

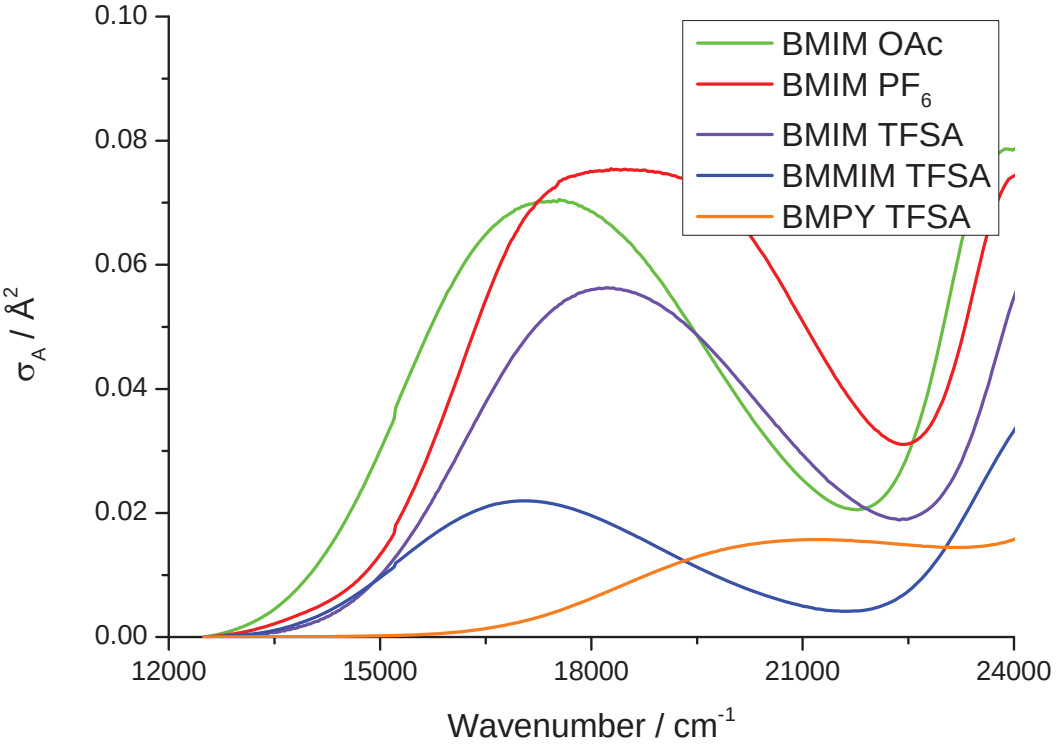


Figure 5.1 - Absorption spectra of Reichardt's dye in ionic liquids

Figure 5.1 shows the absorption spectra of Reichardt's dye in the ionic liquids studied here. It can be seen that there are significant differences in both the positions of the absorption maximum, and the absorption cross-sections across the solvent range. Comparing the data for BMIM OAc, BMIM PF_6, and BMIM TFSA, it can be seen that slight changes in absorption maximum wavelength and cross-section occur upon changing the anionic component of the ionic liquid. Similarly, by comparing BMIM TFSA and BMMIM TFSA, it can be seen that there is again a shift in both wavelength and cross-section upon changing the cationic component of the ionic liquid. This change is further exemplified through extending this comparison to include BMPY TFSA, which is an anion with a significantly different structure than those of $BMIM^+$ and $BMMIM^+$, which are similar excepting an

additional methyl group in $BMMIM^+$. There is a very significant shift of absorption maximum between BMMIM TFSA and BMPY TFSA due to the change in cation.

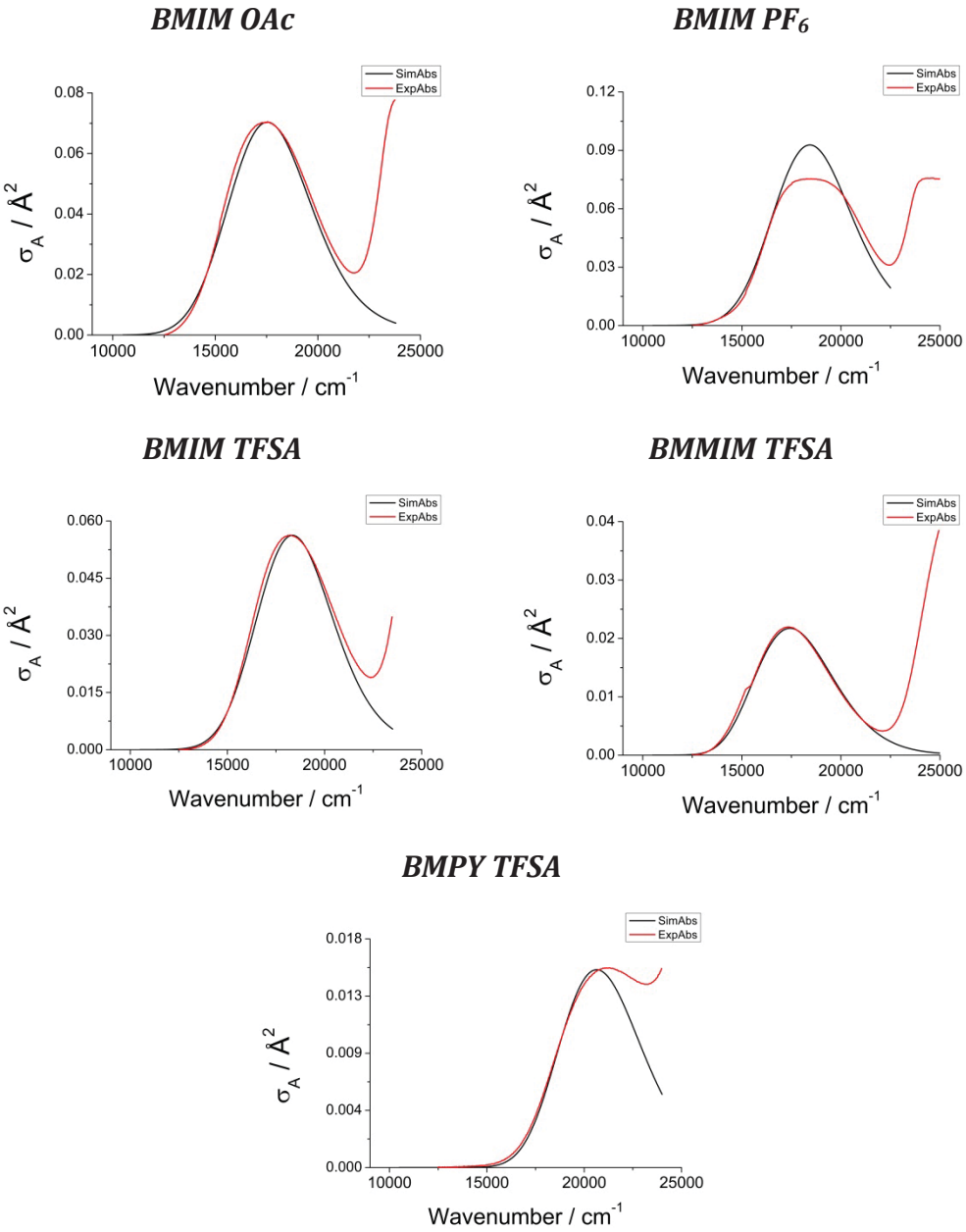


Figure 5.2 - Experimental and simulated absorption spectra of ionic liquids

From the absorption spectra in Figure 5.2 above, the effect of solvent properties on the absorption profile of Reichardt's dye is evident, as it was for the common organic solvents. Again, there are shifts in the absorption maxima and the absorption cross-section based on the ionic liquid which is acting as the solvent in each case.

5.2 Reichardt's Dye resonance Raman Spectra

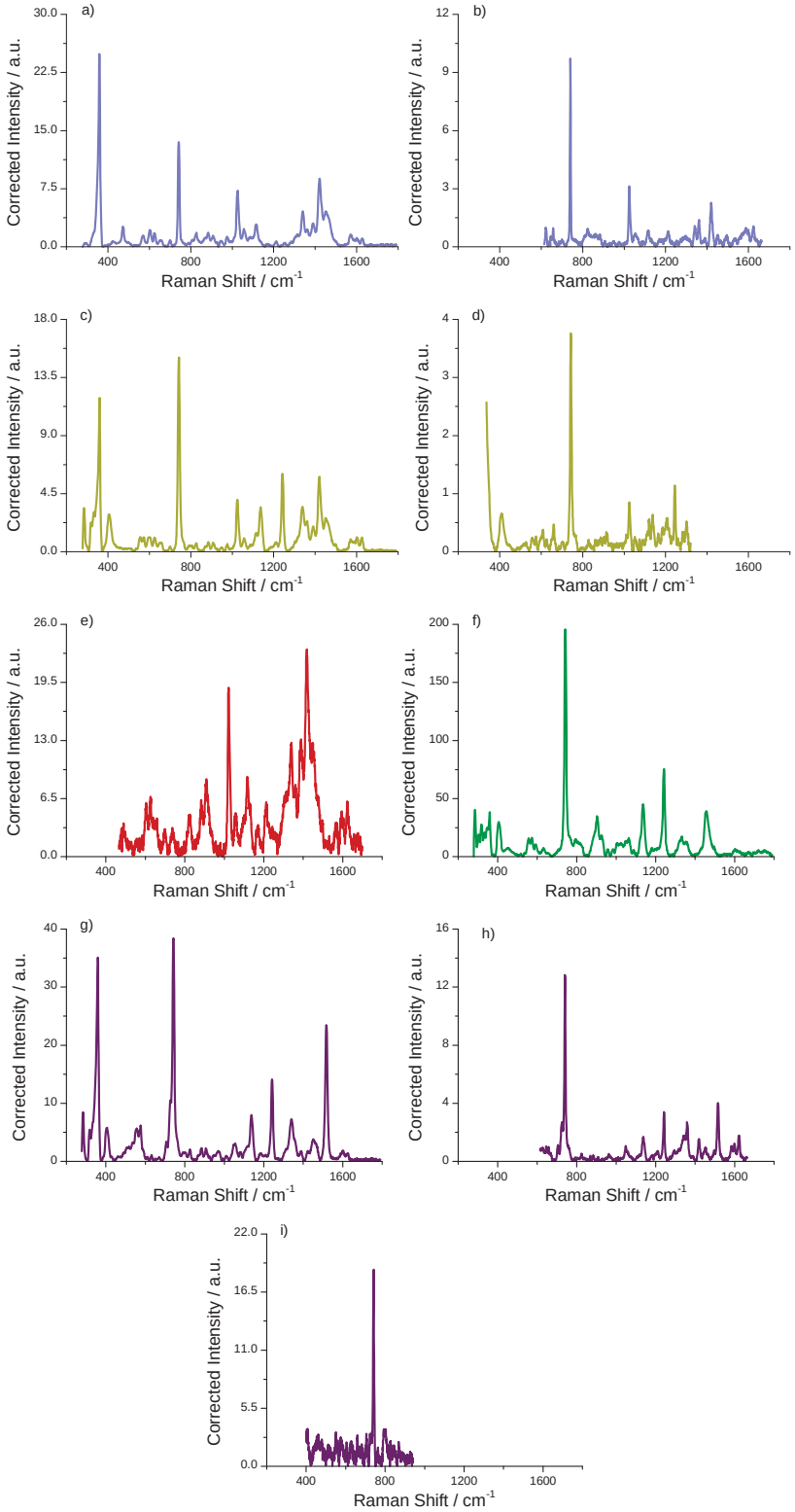


Figure 5.3 - Resonance Raman Spectra of Reichardt's Dye in ionic liquids. a) BMIM PF_6 488nm; b) BMIM PF_6 568nm; c) BMIM TFSA 488nm; d) BMIM TFSA 594nm; e) BMIM OAc 532nm; f) BMPY TFSA 488nm; g) BMMIM TFSA 488nm; h) BMMIM TFSA 568nm; i) BMMIM TFSA 647nm.

The resonance Raman spectra shown in Figure 5.3 were collected and treated as described in Chapter 2, sections 2 and 3.

Figure 5.3 a) and b) show resonance Raman spectra of Reichardt's dye in BMIM PF_6 at excitations of 488nm and 568nm respectively. It can be seen that both spectra are well resolved, and, as such, information can be easily obtained about Reichardt's modes. The solvent and dye peaks do not significantly overlap, and the peaks can be more easily determined. This leads to the ability to perform modelling for this sample over more dye modes than with, for example, dichloromethane or dimethyl sulfoxide (see Chapter 3), which in turn leads to a much more accurate determination of solvent properties such as homogeneous broadening.

Resonance Raman spectra of Reichardt's dye in BMIM TFSA, at 488nm and 594nm excitation, are shown in Figure 5.3 c) and d) respectively. As with the sample in BMIM PF_6, the solvent peaks in these spectra are able to be more easily separated from Reichardt's dye peaks than in solvents such as dichloromethane. Many Reichardt's peaks can be easily discerned in this spectrum, again leading to more accurate modelling being possible.

The resonance Raman spectrum of Reichardt's dye in BMIM OAc at 532nm is shown in Figure 5.3 e). Whilst some Reichardt's dye modes are able to be seen, a large proportion of the peaks in this spectrum are solvent peaks from the ionic liquid. This is, unfortunately, very common with ionic liquids, and can lead to uncertainty as to whether a peak belongs to the solvent or the dye, or whether peaks are combinations of both a solvent and dye peak. This situation leads to uncertainties being common when determining peak areas, and thus differential peak cross-sections which are used in modelling processes.

The above Raman spectra of Reichardt's dye in BMPY TFSA at 488nm excitation shown in Figure 5.3 f) does not show as intense a response for the 1602 cm^{-1} band as can be seen in the spectra for BMIM TFSA (Figure 5.3 c)) and BMMIM TFSA (Figure 5.3 g)) acquired at the same excitation. This shows that changing the cation can have a significant effect on the Raman modes of the solute, which is what is to be expected based on both the solvatochromism of Reichardt's dye, and the large

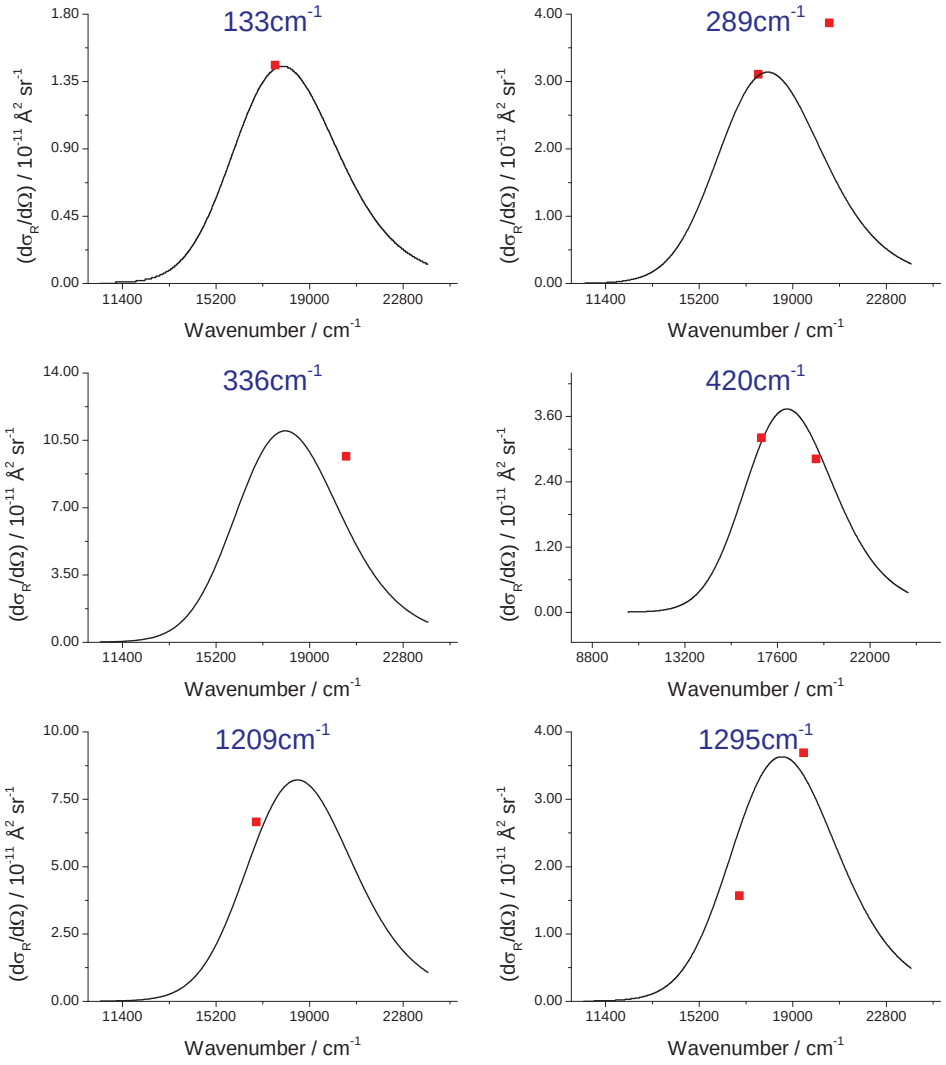
variations possible with ionic liquid properties based on anion and cation selection.

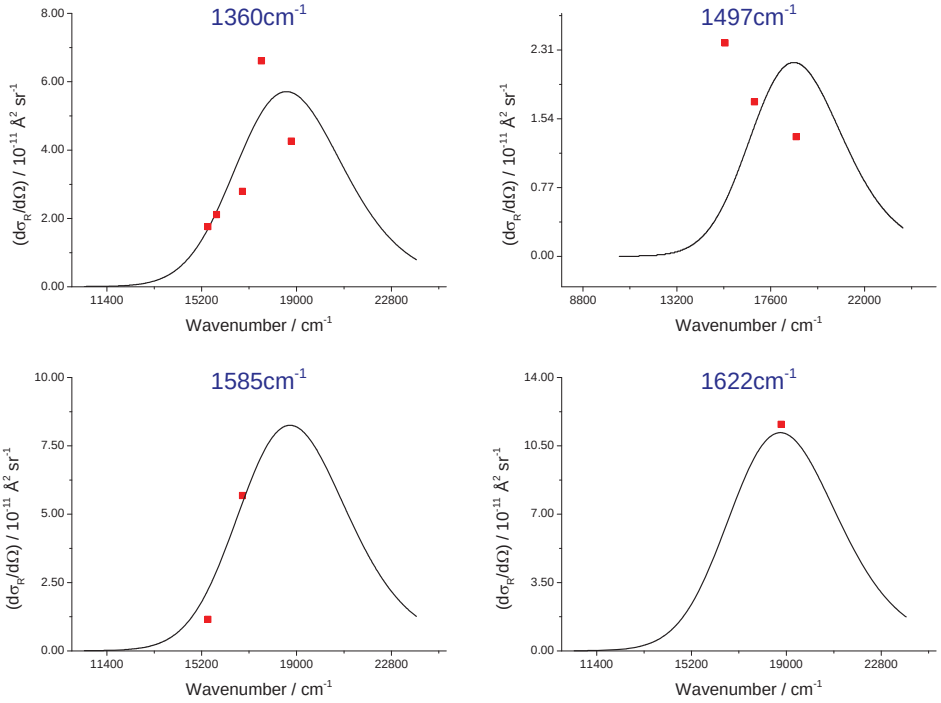
As with the BMIM PF_6 and BMIM TFSA spectra, a large number of Reichardt's peaks are able to be discerned from the spectra of Reichardt's dye in BMMIM TFSA shown in Figure 5.3 g)-i). Comparing the spectrum at 488nm excitation (Figure 5.3 g)) with that at the same excitation for BMIM TFSA (Figure 5.3 c)), it can be seen that additional methyl group has a significant influence on the solvent Raman spectra, particularly around 1400 cm^{-1}, with additional peaks appearing in the spectrum for BMMIM TFSA that don't appear in that for BMIM TFSA. Looking at the three spectra shown for BMMIM TFSA, it can be seen that by changing the excitation wavelength can have a profound effect on relative mode intensities, and also on the presence of background elements, with i) showing much more significant background effects than g) and h). The presence of the additional background can cause difficulties in modelling, as mode cross-section calculations can be affected by overlap of background elements with peaks of interest.

5.3 Reichardt's Dye Modelling

The modelling was performed as stated in Chapter 2, Section 4. The profiles were prepared using Raman spectra of a solution of Reichardt's dye in a selection of ionic liquids. The values of the electronic origin, transition dipole length, and homogeneous broadening used to prepare each of these profiles are listed in the summary table at the end of this section.

5.3.1 Reichardt's Dye in BMIM OAc

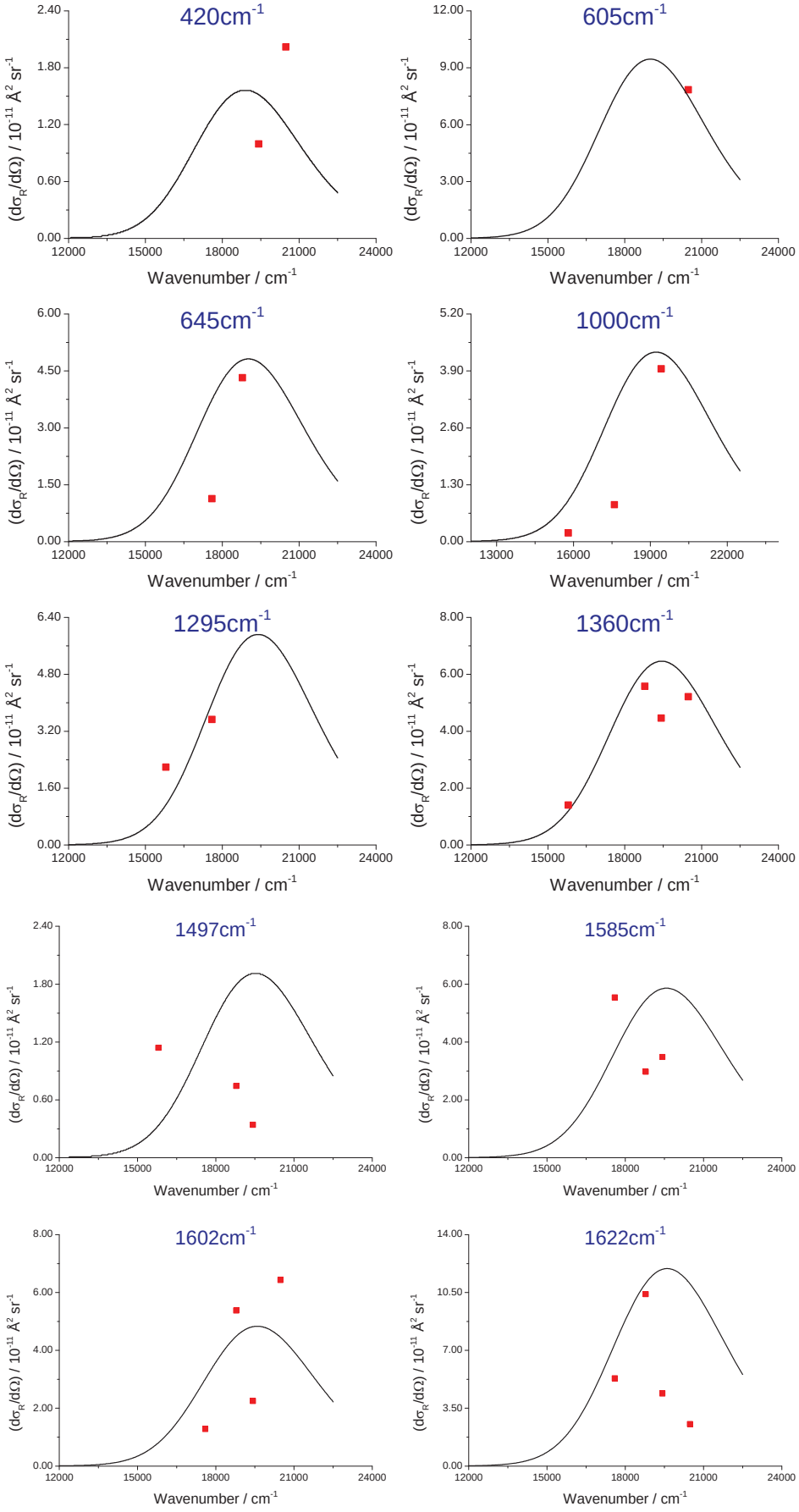




The above profiles, and those on the previous page, were prepared as previously described for acetonitrile. The treatment procedures, in terms of choice of the most accurate experimental data points, were also followed as for acetonitrile.

These simulated profiles fit the experimental data relatively well. It should be noted, however, that as ionic liquids have a large number of Raman peaks, there is a significant chance of solvent and Reichardt's Raman peaks overlapping each other. This leads to a smaller number of Reichardt's dye modes being modelled than would be possible if using a common organic solvent.

5.3.2 Reichardt's Dye in BMIM PF_6

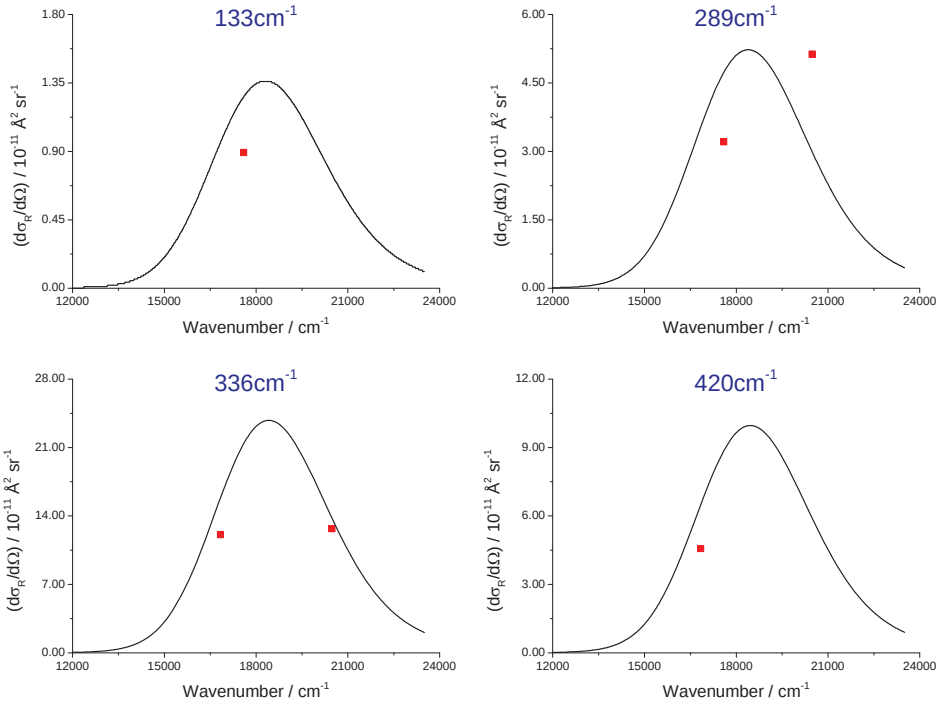


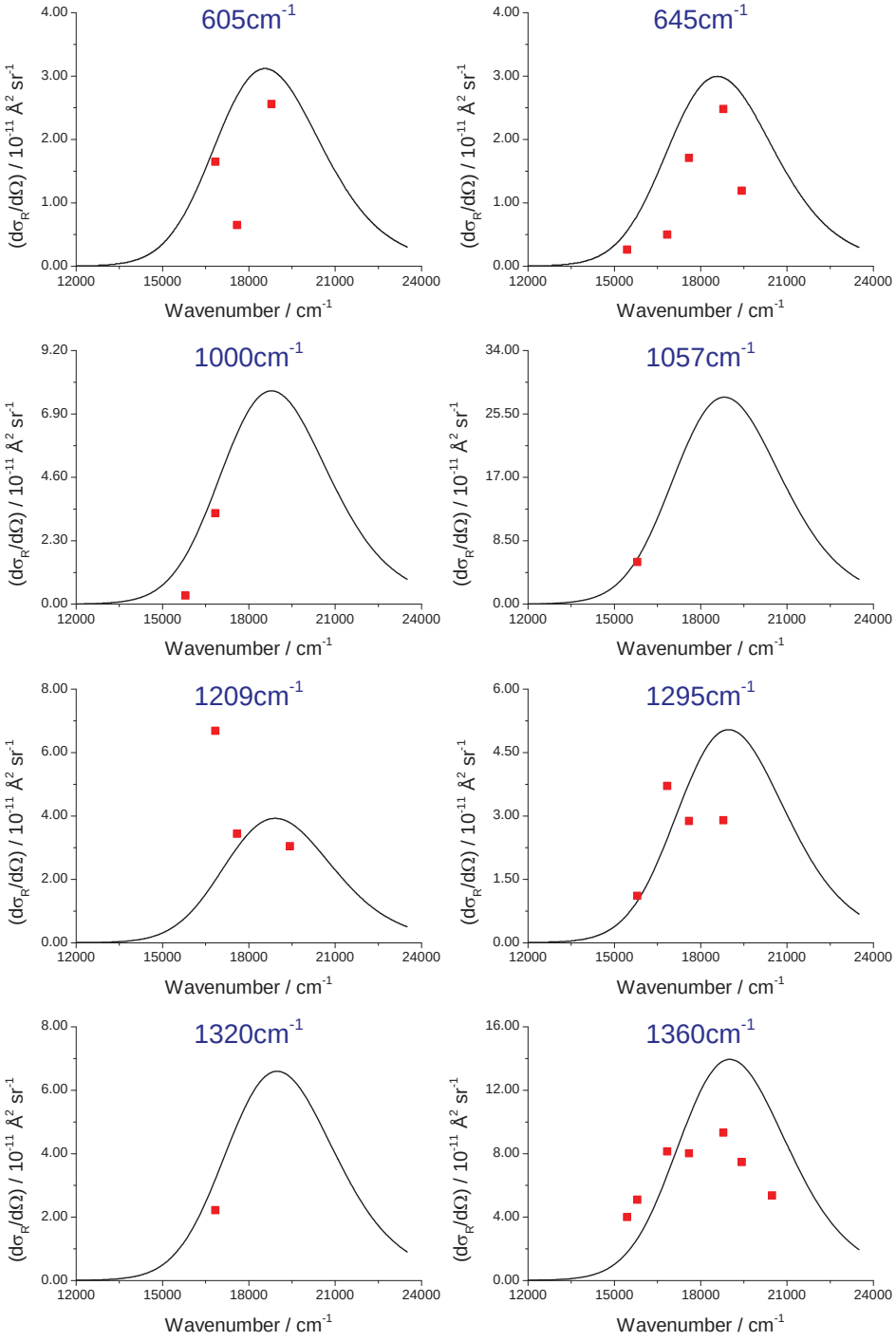
The profiles on the previous page were prepared as previously described for acetonitrile. The treatment procedures, in terms of choice of the most accurate experimental data points, were also followed as for acetonitrile.

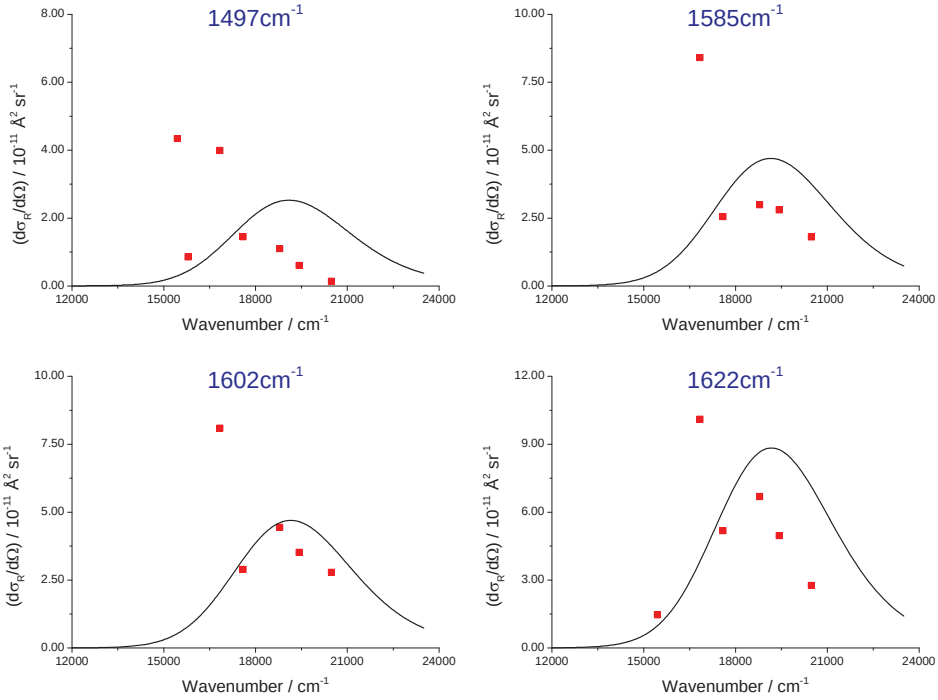
There are some discrepancies present between the experimental data and simulated Raman profiles. These are not significant, however, and are not expected to influence results.

When collecting absorption spectra of this sample, it was found that the sample was too concentrated to get accurate spectra, and as such the maximum of the absorption spectrum was flattened (as is evident in Figure 5.1). Unfortunately, due to only having a small amount of BMIM PF_6 ionic liquid available, this sample was not able to be diluted in order to get a more accurate spectrum. Because of this, it is assumed that the only change in the absorption spectrum acquired is near the maxima, and that the rest of the absorption profile is accurate.

5.3.3 Reichardt's Dye in BMIM TFSA



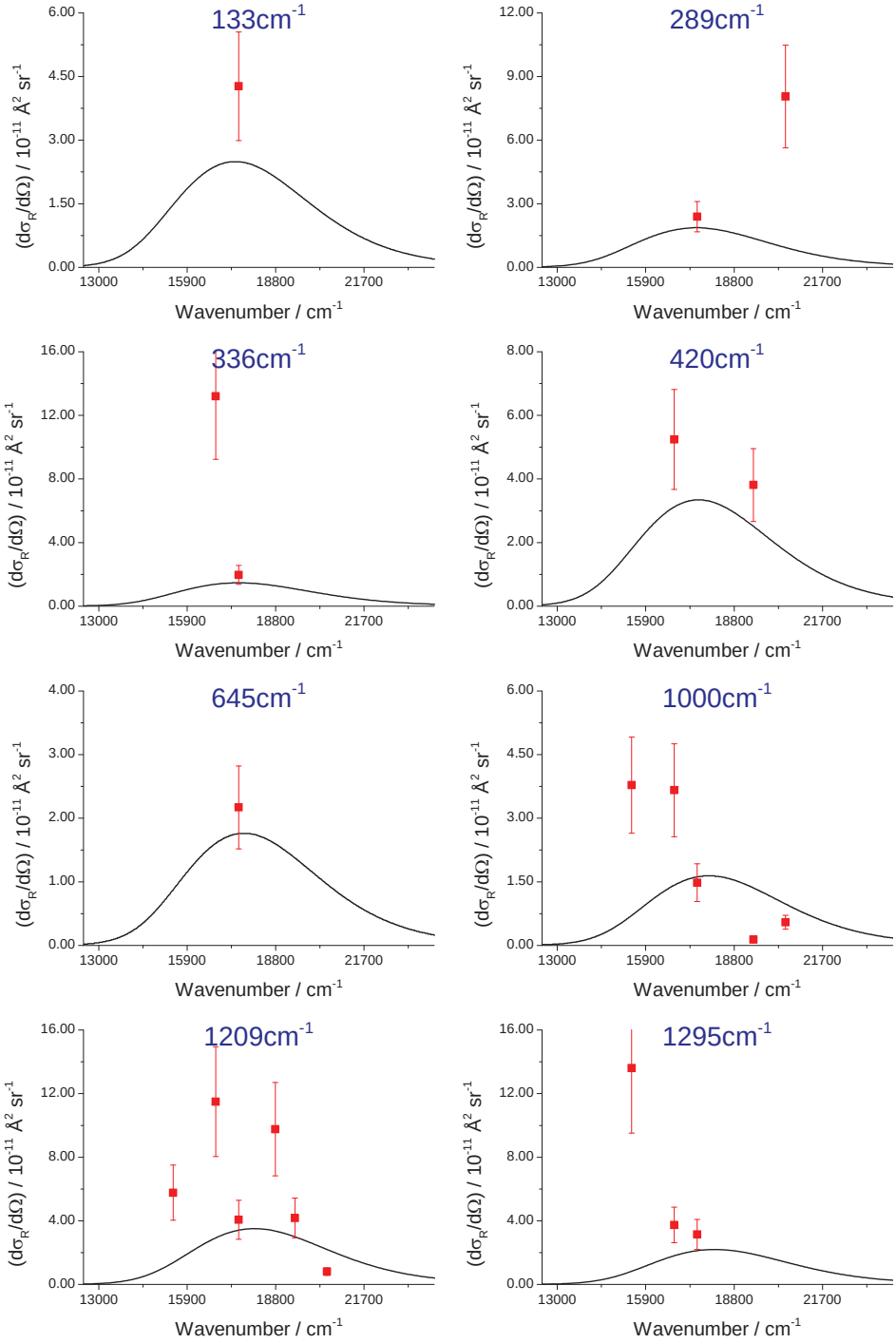

605cm-1
645cm-1
1000cm-1
1057cm-1
1209cm-1
1295cm-1
1320cm-1
1360cm-1
(dσR/dΩ) / 10-11 Å2 sr-1
Wavenumber / cm-1

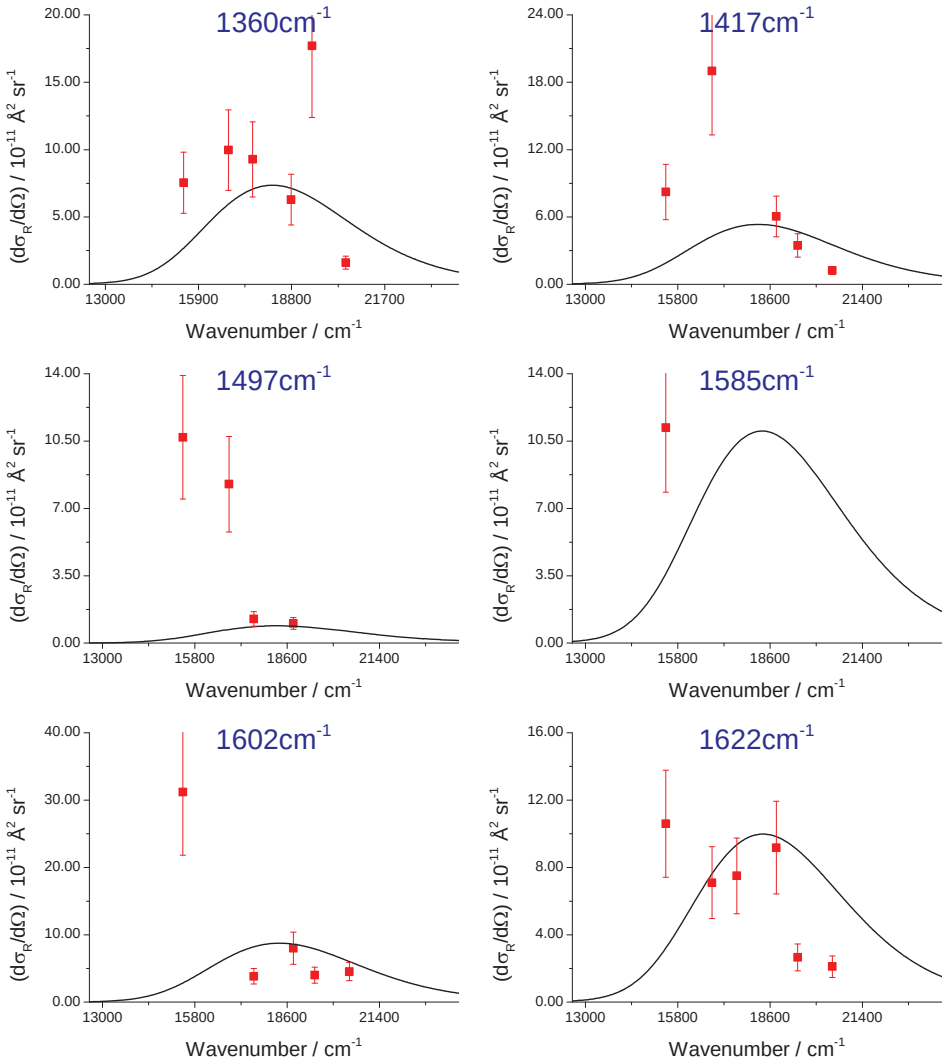


The above profiles, and those on the previous two pages, were prepared as previously described for acetonitrile. The treatment procedures, in terms of choice of the most accurate experimental data points, were also followed as for acetonitrile.

Whilst there are some discrepancies between the experimental Raman data and the simulated Raman profiles, the modelling for the majority of the modes was straight-forward and accurate. The 1497 cm^{-1} mode is an exception to this, as can be seen upon close inspection. The data acquired with lower laser wavelengths does not follow the shape of the profile as well as would be expected. As this problem is only significant in this one mode, however, it is not thought that this will have a substantial effect on the results of the modelling process.

5.3.4 Reichardt's Dye in BMMIM TFSA



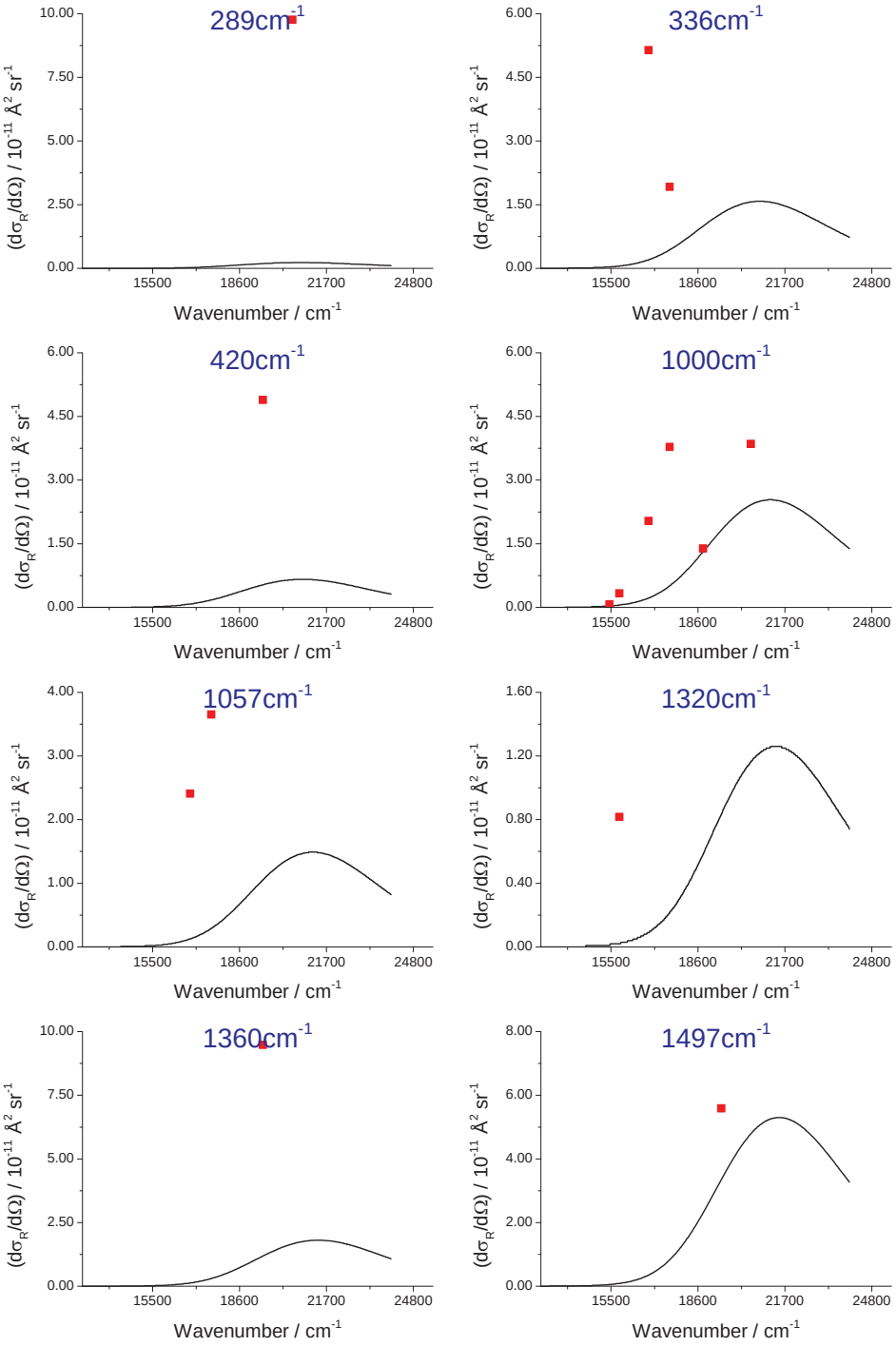


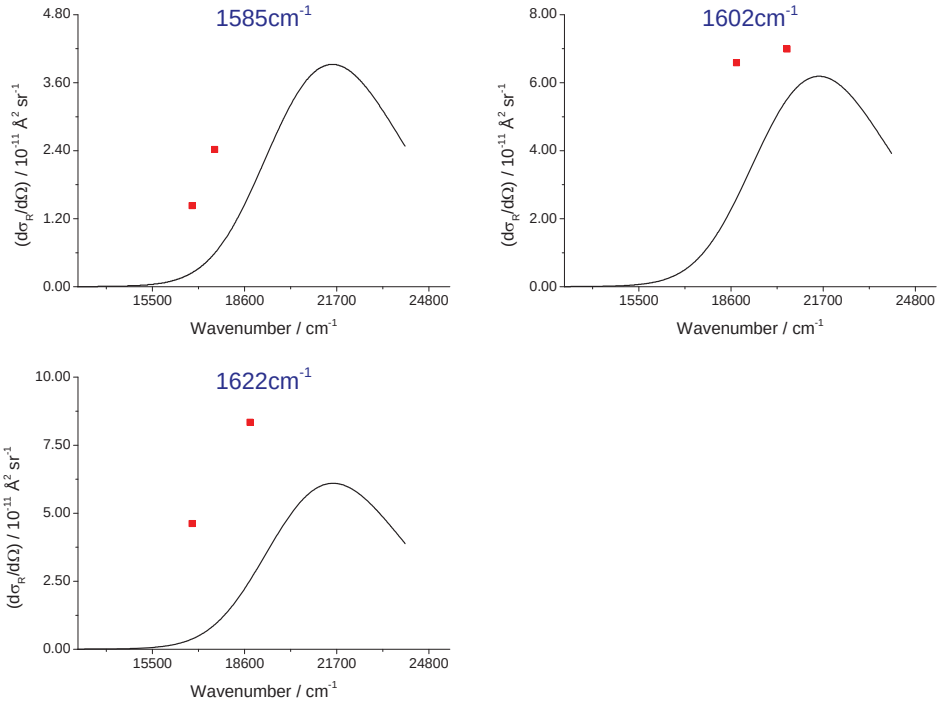
The above profiles, and those on the previous page, were prepared as previously described for acetonitrile. The treatment procedures, in terms of choice of the most accurate experimental data points, were also followed as for acetonitrile.

As can be seen upon inspection of the profiles, there are error bars present for the experimental data points. As in the case of Reichardt's dye in dimethyl sulfoxide, the determination of differential Raman cross-sections was made difficult due to solvent effects. In this case, however, a number of the Reichardt's modes were very close to solvent peaks in the Raman spectrum, and as such the peak fitting process was not as accurate as was desired.

As with previously, due to the presence of the error bars, when adjusting the profile parameters, every effort was made to include as many of these error bars (if not the data points themselves) in the profile. This procedure was used so as to reduce the potential of miscalculation of solvent properties.

5.3.5 Reichardt's Dye in BMPY TFSA





The above profiles, and those on the previous page, were prepared as previously described for acetonitrile. The treatment procedures, in terms of choice of the most accurate experimental data points, were also followed as for acetonitrile.

It can be seen upon inspection of the profiles that there are not many data points which are used for the determination of the simulated Raman profiles. The reasons for this are substantial solvent interference in the experimental Raman spectra, and the Reichardt's peak in the data acquired at non-resonant laser wavelengths not being significant enough to fit accurately. Despite this, every effort has been made to make an accurate and reasonable estimate of the Raman profiles.

An issue which arose with this sample was that the absorption spectrum acquired initially gave very low values of absorption cross-section. In order to test whether these results were accurate, it was decided to acquire another spectrum with a freshly made sample. This was found to give more reasonable values of absorption cross-section. The reasons for this are unknown; however, it is thought that some sample degradation may have occurred with the initially tested sample,

as the absorption spectra were acquired more than a week after the sample was prepared. For a more detailed explanation see Chapter 3 (Section 3.1.4).

5.3.6 Results of Reichardt's Dye Modelling in Ionic Liquids

Table 5.1 below shows the electronic origin, homogeneous broadening, and transition dipole length which have been calculated based on fitting simulated Raman profiles to experimental data points.

Table 5.1 - Electronic properties of ionic liquids from modelling of absorption and Raman profiles

	Electronic Origin (cm^{-1})	Homogeneous Broadening (cm^{-1})	Reorganization Energy (cm^{-1})	Transition Dipole Length (Å)
BMIM OAc	10300	4000	7242	0.572
BMIM PF_6	11400	4000	7242	0.620
BMIM TFSA	11500	3750	6365	0.482
BMMIM TFSA	11950	2600	3060	0.304
BMPY TFSA	14500	3280	4870	0.245

A similar table to Table 5.1 has previously been shown for a selection of common organic solvents in Chapter 3, Table 4.3. The information from these two tables can be used to prepare relative scales of solvent properties.

5.4 Reliability of Modelling of Raman Profiles

The reliability of this modelling method is able to be commented on as a result of approximations made during the modelling process. When performing modelling for this study, it was found that some Reichardt's Dye Raman modes did not appear in the resonance Raman spectra. In the case where the mode of interest simply did not appear in the resonance Raman spectra at selected excitation wavelengths, but did in others, this problem was simply overlooked. There were also some cases, however, where a selected mode or modes did not appear in the Raman spectra at any excitation wavelength, or were overlapping with solvent peaks and could not be resolved. In this case, the deltas for the modes were assumed to be very small. This leads to the possibility of solvent reorganization

energy not being accurately calculated, as these calculations are dependent on accurate delta values.

Another source of inaccuracy of modelling is the inclusion of non-Condon coupling effects.[38] For this study, the data obtained was not sufficient to gain information on non-Condon effects, and as such these were not included in the modelling process. Although it is likely that some vibrational modes have a strong effect on the transition dipole moment, this effect cannot be discerned due to the relatively high uncertainties in the fits to the Raman excitation profiles.

When performing modelling of Raman profiles, many parameters are required. One of these parameters is the stochastic line shape parameter, R_{K}, defined in Chapter 2 as the ratio of the magnitude of line broadening over the modulation frequency of the solvent. For common organic solvents a value of 0.1 is used as standard. It was assumed for this study that the value of R_{K} would be equal to 0.1 for ionic liquids also, however, this may not be realistic. If the value of R_{K} is not 0.1 for ionic liquids, the results of this study may have been affected by this discrepancy.

5.5 Properties of Ionic Liquids

Many properties of ionic liquids have been studied in order to form comparisons with common organic solvents. The polarity of ionic liquids has been compared to common organic solvents in many ways, commonly the $E_T(30)$ scale[25], as described in Chapter 1. Another property which has been studied is the rate of electron transfer. Maroncelli et al[50] compared the rates of three excited-state intramolecular electron transfer reactions in ionic liquids. They found, with great certainty in two of the three ionic liquids studied, that ionic liquids behave as slow-moving versions of conventional solvents, as far as their effect on solvent-controlled electron transfer reactions are concerned.

Another property of ionic liquids which has been studied is the effect of the charges on the ions in the liquid. Castner and Shirota[72] studied the ionic liquid 1-methoxyethylpyridinium dicyanoamide ($MOEPy^+/DCA^-$) and an analogous isoelectronic binary solution comprised of 1-methoxyethylbenzene (MOEBz) and

dicyanomethane (DCM) in order to determine whether the properties of ionic liquids are more dependent on the charges of the molecular ions, or the liquid being a complex mixture of two asymmetric species. They found that $MOEPy^+/DCA^-$ was higher in density, viscosity, and had higher intermolecular vibrational frequencies than for the isoelectronic solution. This indicates that the ionic liquid would have stronger interactions than the neutral solution. Further studies, including NMR and time-resolved fluorescence probe studies, should give further information on structural, dynamical, and thermodynamic properties of ionic liquids.[72]

As stated previously, the information acquired during the modelling process can be used to prepare relative scales of solvent properties. Of particular interest are the homogeneous broadening and reorganization energies of the common organic solvents and ionic liquids.

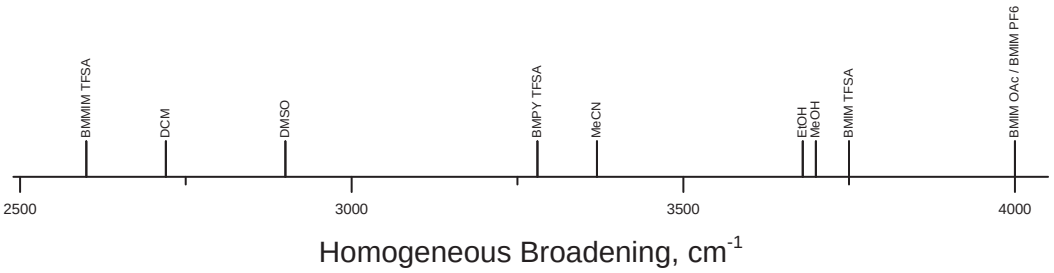


Figure 5.4 - Relative scale of homogeneous broadening of common organic solvents and ionic liquids

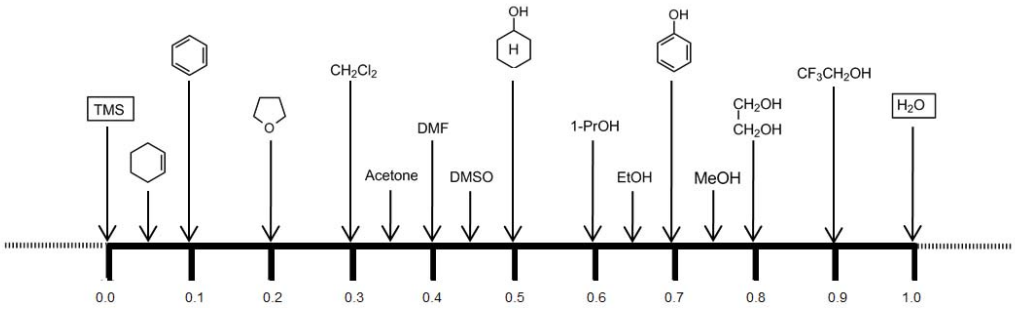


Figure 5.5 - Normalized $E_T(30)$ scale for a range of common molecular solvents[25]

Figure 5.4 shows a relative scale of homogeneous broadening of solvents found in this study. This scale is analogous to solvent polarity scales, and the order of solvents should agree with the $E_T(30)$ scale of solvent polarity, which is shown in Figure 5.5, and was shown in more detail previously in Chapter 1, Figure 1.7. As the ordering of the common organic solvents agrees between the two scales, this indicates that the method used in this study should give accurate representations of solvent properties.

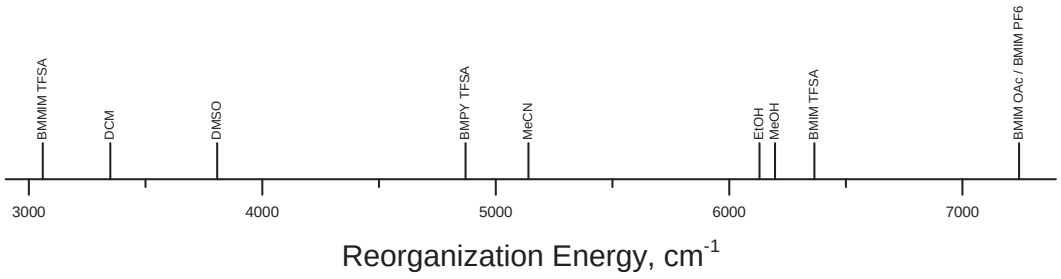


Figure 5.6 - Relative scale of reorganization energies of common organic solvents and ionic liquids

The acquisition of a relative scale of reorganization energies, as shown in Figure 5.6 above, is significant, as this is directly applicable to applications of ionic liquids involving electron transfer.

Chapter 6 – Conclusion

6.0 Conclusion

Spectroscopic and computational methods have been employed in order to determine selected properties of ionic liquids. Absorption spectroscopy, and then resonance Raman spectroscopy, were performed on the solvatochromic Reichardt's dye in a selection of organic and ionic liquid solvents. As the Raman bands associated with Reichardt's dye have different relative intensities, and thus cross-sections, in different solvents, the analysis of the resonance Raman spectra of the selected solvents enabled the solvent reorganization energies to be determined.

Computational studies were performed in order to assign the vibrational modes of Reichardt's dye. In addition to obtaining information on the vibrational modes, further understanding of the solute dynamics were able to be obtained. From the computational studies, the vibrational modes of Reichardt's dye were able to be assigned to bands in the resonance Raman spectra.

From spectroscopic measurements, the absorption and Raman scattering cross-sections of the vibrational modes of Reichardt's dye were found. These cross-sections were modelled in order to determine the solvent reorganization properties of the selected solvents and ionic liquids. The solvent reorganization energies were then compared, whereupon it was found that the reorganization energies associated with ionic liquids were similar to those of common organic solvents. This indicates that, from a solvent reorganization standpoint, it should be possible to select ionic liquids to replace common organic solvents in processes in which issues such as solvent volatility are of concern. In addition to this, the solvent reorganization parameters found using this method are able to indicate the suitability of ionic liquids in processes involving electron transfer in general.

The values of solvent reorganization energy obtained in this study were compared to those previously obtained by others. Upon analysis of the literature values of solvent reorganization energy, it was found that there was a significant variance in values obtained depending on the method used. Due to this variance, it

is not possible to state with certainty whether the values obtained in this study are truly accurate; however they are not inconsistent with those in the literature.

6.1 Future Work

The extension of this study into a wider range of common organic solvents and ionic liquids would provide further understanding of ionic liquid properties. The expansion of the solvent reorganization energy scale to include ionic liquids with different anions and cations than those studied here would provide a much wider understanding of ionic liquid properties.

In order to obtain a better understanding of the solvent properties of ionic liquids, further computational studies should be performed. By studying the properties of Reichardt's dye in each solvent in this study more explicitly, through the inclusion of an accurate solvent model in which hydrogen bonding and other solute-solvent interactions can be studied, a more complete picture can be formed. In order to accurately model processes in ionic liquids, and even common organic solvents, appropriate theories must be developed, for example, the reference interaction site model.[73] From these studies, it would be possible to compute solvent reorganization energies, which can then compared to experimental values.

Further experimental studies will also provide more information about ionic liquid properties. High Pressure Raman studies can be performed on ionic liquids[3] in order to determine changes which occur at high pressure. This is of importance for potential applications of ionic liquids. In addition, the analogous isoelectronic neutral binary solutions of the ionic liquids could be investigated using resonance Raman spectroscopy in order to determine the effect of the charged species in the ionic liquid.

Combining both computational and experimental results of studies would lead to a better understanding of ionic liquid properties, and give indications on potential applications for which the inclusion of ionic liquids would be suitable.

Bibliography

1. Scott, A. P.; Radom, L., Harmonic Vibrational Frequencies: An Evaluation of Hartree–Fock, Møller–Plesset, Quadratic Configuration Interaction, Density Functional Theory, and Semiempirical Scale Factors. *The Journal of Physical Chemistry* 1996, 100, 16502-16513.

2. MacFarlane, D. R.; Forsyth, M.; Izgorodina, E. I.; Abbott, A. P.; Annat, G.; Fraser, K., On the concept of ionicity in ionic liquids. *Physical Chemistry Chemical Physics* 2009, 11.

3. Su, L.; Li, M.; Zhu, X.; Wang, Z.; Chen, Z.; Li, F.; Zhou, Q.; Hong, S., In Situ Crystallization of Low-Melting Ionic Liquid [BMIM][PF6] under High Pressure up to 2 GPa. *The Journal of Physical Chemistry B* 2010, 114, 5061-5065.

4. Zhou, Y.; Antonietti, M., Synthesis of Very Small TiO2 Nanocrystals in a Room-Temperature Ionic Liquid and Their Self-Assembly toward Mesoporous Spherical Aggregates. *Journal of the American Chemical Society* 2003, 125, 14960-14961.

5. Dupont, J.; de Souza, R. F.; Suarez, P. A. Z., Ionic Liquid (Molten Salt) Phase Organometallic Catalysis. *Chemical Reviews* 2002, 102, 3667-3692.

6. Koel, M., Ionic Liquids in Chemical Analysis. *Critical Reviews in Analytical Chemistry* 2005, 35, 177-192.

7. Chiappe, C.; Pieraccini, D., Ionic liquids: solvent properties and organic reactivity. *Journal of Physical Organic Chemistry* 2005, 18, 275-297.

8. Wei, Z.; Liu, C.-j., Synthesis of monodisperse gold nanoparticles in ionic liquid by applying room temperature plasma. *Materials Letters* 2011, 65, 353-355.

9. Rogers, E. I.; Šljukić, B.; Hardacre, C.; Compton, R. G., Electrochemistry in Room-Temperature Ionic Liquids: Potential Windows at Mercury Electrodes. *Journal of Chemical & Engineering Data* 2009, 54, 2049-2053.

10. Yoshida, Y.; Baba, O.; Larriba, C.; Saito, G., Imidazolium-Based Ionic Liquids Formed with Dicyanamide Anion: Influence of Cationic Structure on Ionic Conductivity. *The Journal of Physical Chemistry B* 2007, 111, 12204-12210.

11. Fletcher, K. A.; Storey, I. A.; Hendricks, A. E.; Pandey, S.; Pandey, S., Behavior of the solvatochromic probes Reichardt's dye, pyrene, dansylamide, Nile Red and 1-pyrenecarbaldehyde within the room-temperature ionic liquid bmimPF. *Green Chemistry* 2001, 3, 210-215.

12. He, P.; Liu, H.; Li, Z.; Liu, Y.; Xu, X.; Li, J., Electrochemical Deposition of Silver in Room-Temperature Ionic Liquids and Its Surface-Enhanced Raman Scattering Effect. *Langmuir* 2004, 20, 10260-10267.

13. Dash, P.; Miller, S. M.; Scott, R. W. J., Stabilizing nanoparticle catalysts in imidazolium-based ionic liquids: A comparative study. *Journal of Molecular Catalysis A: Chemical* 2010, 329, 86-95.

14. Dzyuba, S. V.; Bartsch, R. A., Expanding the polarity range of ionic liquids. *Tetrahedron Letters* 2002, 43, 4657-4659.

15. Ober, C. A.; Gupta, R. B., pH Control of Ionic Liquids with Carbon Dioxide and Water: 1-Ethyl-3-methylimidazolium Acetate. *Industrial & Engineering Chemistry Research* 2012, 51, 2524-2530.

16. Valderrama, J. O.; Robles, P. A., Critical Properties, Normal Boiling Temperatures, and Acentric Factors of Fifty Ionic Liquids. *Industrial & Engineering Chemistry Research* 2007, 46, 1338-1344.

17. Ong, S. P.; Andreussi, O.; Wu, Y.; Marzari, N.; Ceder, G., Electrochemical Windows of Room-Temperature Ionic Liquids from Molecular Dynamics

and Density Functional Theory Calculations. *Chemistry of Materials* 2011, 23, 2979-2986.

18. Bhatt, A. I.; Mechler, A.; Martin, L. L.; Bond, A. M., Synthesis of Ag and Au nanostructures in an ionic liquid: thermodynamic and kinetic effects underlying nanoparticle, cluster and nanowire formation. *Journal of Materials Chemistry* 2007, 17, 2241-2250.

19. An, J.; Wang, D.; Luo, Q.; Yuan, X., Antimicrobial active silver nanoparticles and silver/polystyrene core-shell nanoparticles prepared in room-temperature ionic liquid. *Materials Science and Engineering: C* 2009, 29, 1984-1989.

20. Earle, M. J.; Seddon, K. R., Ionic liquids. Green solvents for the future. *Pure Appl. Chem.* 2000, 72, 1391-1398.

21. Peter Koch, E. K. Ionic liquids as solvents in headspace gas chromatography. US7569149, Jul 28, 2003, 2003.

22. Lavallard, G. L. a. P., Optical properties of dye molecules as a function of the surrounding dielectric medium. *Phys. Rev. A* 1999, 59.

23. Zakerhamidi, M. S.; Ghanadzadeh, A.; Moghadam, M., Solvent Effects on the UV/Visible Absorption Spectra of Some Aminoazobenzene Dyes. *Chem Sci Trans.* 2012, 1, 1-8.

24. Nag, A.; Goswami, D., Solvent effect on two-photon absorption and fluorescence of rhodamine dyes. *Journal of Photochemistry and Photobiology A: Chemistry* 2009, 206, 188-197.

25. Reichardt, C., Polarity of ionic liquids determined empirically by means of solvatochromic pyridinium N-phenolate betaine dyes. *Green Chemistry* 2005, 7, 339-351.

26. Lobaugh, J.; Rossky, P. J., Solvent and Intramolecular Effects on the Absorption Spectrum of Betaine-30. *The Journal of Physical Chemistry A* 2000, 104, 899-907.

27. Jessop, P. G.; Jessop, D. A.; Fu, D.; Phan, L., Solvatochromic parameters for solvents of interest in green chemistry. *Green Chemistry* 2012, 14, 1245-1259.

28. Zhao, X.; McHale, J. L., Probing the molecular basis for solvent-induced dephasing using resonance Raman spectroscopy: betaine-30 in CH3OH, CH3OD, and CD3OD. *Chemical Physics Letters* 2003, 378, 582-588.

29. Zhao, X.; Burt, J. A.; McHale, J. L., Resonance Raman analysis of nonlinear solvent dynamics: Betaine-30 in ethanol. *Journal of Chemical Physics* 2004, 121, 11195-11201.

30. Zong, Y.; McHale, J. L., Resonance Raman study of solvent dynamics in electron transfer. I. Betaine-30 in CH[sub 3]CN and CD[sub 3]CN. *The Journal of Chemical Physics* 1997, 106, 4963-4972.

31. Zong, Y.; McHale, J. L., Resonance Raman study of solvent dynamics in electron transfer. II. Betaine-30 in CH[sub 3]OH and CD[sub 3]OD. *The Journal of Chemical Physics* 1997, 107, 2920-2929.

32. Zhao, X.; Burt, J. A.; Knorr, F. J.; McHale, J. L., Thermosolvatochromism of Betaine-30 in CH3CN. *The Journal of Physical Chemistry A* 2001, 105, 11110-11117.

33. Catalán, J.; Paz, J. L. G. d.; Reichardt, C., On the Molecular Structure and UV/vis Spectroscopic Properties of the Solvatochromic and Thermochromic Pyridinium-N-Phenolate Betaine Dye B30. *The Journal of Physical Chemistry A* 2010, 114, 6226-6234.

34. Zhao, X.; Knorr, F. J.; McHale, J. L., Temperature-dependent absorption spectrum of betaine-30 in methanol. *Chemical Physics Letters* 2002, 356, 214-220.

35. Maroncelli, M.; Zhang, X.-X.; Liang, M.; Roy, D.; Ernsting, N. P., Measurements of the complete solvation response of coumarin 153 in ionic liquids and the accuracy of simple dielectric continuum predictions. *Faraday Discussions* 2012, 154, 409-424.

36. Mente, S. R.; Maroncelli, M., Computer Simulations of the Solvatochromism of Betaine-30. *The Journal of Physical Chemistry B* 1999, 103, 7704-7719.

37. Roy, D.; Maroncelli, M., Simulations of Solvation and Solvation Dynamics in an Idealized Ionic Liquid Model. *The Journal of Physical Chemistry B* 2012, 116, 5951-5970.

38. Moran, A. M.; Delbecque, C.; Kelley, A. M., Solvent Effects on Ground and Excited Electronic State Structures of the Push-Pull Chromophore Julolidinyl-n-N,N‘-diethylthiobarbituric Acid. *The Journal of Physical Chemistry A* 2001, 105, 10208-10219.

39. Egolf, D. S.; Waterland, M. R.; Kelley, A. M., Resonance Raman Intensity Analysis of the Carbazole/Tetracyanoethylene Charge-Transfer Complex: Mode-Specific Reorganization Energies for a Hole-Transport Molecule†. *The Journal of Physical Chemistry B* 2000, 104, 10727-10737.

40. University, A. S. The Marcus Theory of Electron Transfer. www.public.asu.edu/~laserweb/woodbury/classes/chm341/lecture_set8/The%20Marcus%20Theory%20of%20Electron%20Transfer.pdf.

41. Marcus, R. A., On the Theory of Oxidation-Reduction Reactions Involving Electron Transfer. I. *The Journal of Chemical Physics* 1956, 24, 966-978.

42. Wander, M. C. F.; Shuford, K. L., A theoretical study of the qualitative reaction mechanism for the homogeneous disproportionation of pentavalent uranyl ions. *Geochimica et Cosmochimica Acta* 2012, 84, 177-185.

43. Marcus, R. A., Chemical and Electrochemical Electron-Transfer Theory. *Annual Review of Physical Chemistry* 1964, 15, 155-196.

44. Myers, A. B., Resonance Raman Intensities and Charge-Transfer Reorganization Energies. *Chemical Reviews* 1996, 96, 911-926.

45. Kharlanov, V.; Rettig, W., Experimental and Theoretical Study of Excited-State Structure and Relaxation Processes of Betaine-30 and of Pyridinium Model Compounds. *The Journal of Physical Chemistry A* 2009, 113, 10693-10703.

46. Kim, H.; Hwang, H.; Rossky, P. J., Quantum Simulation of Solution Phase Intramolecular Electron Transfer Rates in Betaine-30. *The Journal of Physical Chemistry A* 2006, 110, 11223-11229.

47. Ishida, T.; Rossky, P. J., Solvent Effects on Solute Electronic Structure and Properties: Theoretical Study of a Betaine Dye Molecule in Polar Solvents. *The Journal of Physical Chemistry A* 2001, 105, 558-565.

48. Ishida, T.; Rossky, P. J., Consequences of Strong Coupling between Solvation and Electronic Structure in the Excited State of a Betaine Dye. *The Journal of Physical Chemistry B* 2008, 112, 11353-11360.

49. Znamenskiy, V.; Kobrak, M. N., Molecular Dynamics Study of Polarity in Room-Temperature Ionic Liquids. *The Journal of Physical Chemistry B* 2003, 108, 1072-1079.

50. Li, X.; Liang, M.; Chakraborty, A.; Kondo, M.; Maroncelli, M., Solvent-Controlled Intramolecular Electron Transfer in Ionic Liquids. *The Journal of Physical Chemistry B* 2011, 115, 6592-6607.

51. Long, D. A., *Raman Spectroscopy*. McGraw-Hill, Inc: Great Britain, 1977.

52. Clark, R. J. H.; Dines, T. J., Resonance Raman Spectroscopy, and Its Application to Inorganic Chemistry. New Analytical Methods (27). *Angewandte Chemie International Edition in English* 1986, 25, 131-158.

53. Myers, A. B.; Mathies, R. A., Resonance Raman Intensities: A Probe of Excited-State Structure and Dynamics. In *Biological Applications of Raman Spectroscopy*, Spiro, T. G., Ed. John Wiley & Sons: 1987; Vol. 2, pp 1-57.

54. Heller, E. J., The semiclassical way to molecular spectroscopy. *Accounts of Chemical Research* 1981, 14, 368-375.

55. Heller, E. J.; Sundberg, R.; Tannor, D., Simple aspects of Raman scattering. *The Journal of Physical Chemistry* 1982, 86, 1822-1833.

56. Tannor, D., *Introduction to Quantum Mechanics: A Time-Dependent Perspective*. University Science Books: Sausalito, California, 2007.

57. Li, B.; Johnson, A. E.; Mukamel, S.; Myers, A. B., The Brownian oscillator model for solvation effects in spontaneous light emission and their relationship to electron transfer. *Journal of the American Chemical Society* 1994, 116, 11039-11047.

58. Burrell, A. K.; Sesto, R. E. D.; Baker, S. N.; McCleskey, T. M.; Baker, G. A., The large scale synthesis of pure imidazolium and pyrrolidinium ionic liquids. *Green Chemistry* 2007, 9, 449-454.

59. Lind, S. J.; Gordon, K. C.; Waterland, M. R., Ultrafast dynamics in Cu(I)bisdiimine complexes from resonance Raman intensities. *Journal of Raman Spectroscopy* 2008, 39, 1556-1567.

60. Waterland, M. R.; Howell, S. L.; Gordon, K. C., Using Internal Coordinates to Describe Photoinduced Geometry Changes in MLCT Excited States. *The Journal of Physical Chemistry A* 2007, 111, 4604-4611.

61. Lundin, N. J.; Walsh, P. J.; Howell, S. L.; McGarvey, J. J.; Blackman, A. G.; Gordon, K. C., Complexes of Functionalized Dipyrido[3,2-a:2‘,3‘-c]-phenazine: A Synthetic, Spectroscopic, Structural, and Density Functional Theory Study. *Inorganic Chemistry* 2005, 44, 3551-3560.

62. Walsh, P. J.; Gordon, K. C.; Lundin, N. J.; Blackman, A. G., Photoexcitation in Cu(I) and Re(I) Complexes Containing Substituted Dipyrido[3,2-a:2‘,3‘-c]phenazine: A Spectroscopic and Density Functional Theoretical Study. *The Journal of Physical Chemistry A* 2005, 109, 5933-5942.

63. McLean, T. M.; Cleland, D. M.; Lind, S. J.; Gordon, K. C.; Telfer, S. G.; Waterland, M. R., Strongly Absorbing π–π* States in Heteroleptic Dipyrrin/2,2′-Bipyridine Ruthenium Complexes: Excited-State Dynamics from Resonance Raman Spectroscopy. *Chemistry – An Asian Journal* 2010, 5, 2036-2046.

64. Clarke, T. M.; Gordon, K. C.; Officer, D. L.; Grant, D. K., The effect of oxidation on the structure of styryl-substituted sexithiophenes: A resonance Raman spectroscopy and density functional theory study. *The Journal of Chemical Physics* 2006, 124, 164501-11.

65. Clarke, T. M.; Gordon, K. C.; Officer, D. L.; Hall, S. B.; Collis, G. E.; Burrell, A. K., Theoretical and Spectroscopic Study of a Series of Styryl-Substituted Terthiophenes. *The Journal of Physical Chemistry A* 2003, 107, 11505-11516.

66. Clarke, T. M.; Gordon, K. C., A computational study of regioisomers formed from the σ-dimerisation of asymmetric terthiophenes. *Journal of Molecular Structure: THEOCHEM* 2007, 815, 135-143.

67. Clarke, T. M.; Gordon, K. C.; Wagner, P.; Officer, D. L., Modulation of Electronic Properties in Neutral and Oxidized Oligothiophenes Substituted with Conjugated Polyaromatic Hydrocarbons. *The Journal of Physical Chemistry A* 2007, 111, 2385-2397.

68. Kjaer, A. M.; Ulstrup, J., Solvent bandwidth dependence and band asymmetry features of charge-transfer transitions in N-pyridinium phenolates. *Journal of the American Chemical Society* 1987, 109, 1934-1942.

69. Reid, P. J.; Barbara, P. F., Dynamic Solvent Effect on Betaine-30 Electron-Transfer Kinetics in Alcohols. *The Journal of Physical Chemistry* 1995, 99, 3554-3565.

70. Walker, G. C.; Aakesson, E.; Johnson, A. E.; Levinger, N. E.; Barbara, P. F., Interplay of solvent motion and vibrational excitation in electron-transfer kinetics: experiment and theory. *The Journal of Physical Chemistry* 1992, 96, 3728-3736.

71. Perng, B.-C.; Newton, M. D.; Raineri, F. O.; Friedman, H. L., Energetics of charge transfer reactions in solvents of dipolar and higher order multipolar character. II. Results. *The Journal of Chemical Physics* 1996, 104, 7177-7204.

72. Shirota, H.; Castner, E. W., Physical Properties and Intermolecular Dynamics of an Ionic Liquid Compared with Its Isoelectronic Neutral Binary Solution. *The Journal of Physical Chemistry A* 2005, 109, 9388-9392.

73. Sato, H., A modern solvation theory: quantum chemistry and statistical chemistry. *Physical Chemistry Chemical Physics* 2013, 15, 7450-7465.

Appendices

Appendix One – Ionic Liquid Solvent Bands

This appendix gives information on the Raman spectrum solvent bands for the ionic liquids used in this study. Solvent band positions are indicated below. Where it is not clear whether a shift refers to a solvent band it has italicised, but has still been included here for completeness.

BMIM OAc Raman band positions

174 cm^{-1}	*212 cm^{-1}*	*277 cm^{-1}*	*327 cm^{-1}*	*358 cm^{-1}*	*403 cm^{-1}*
414 cm^{-1}	419 cm^{-1}	433 cm^{-1}	458 cm^{-1}	*459 cm^{-1}*	480 cm^{-1}
496 cm^{-1}	*525 cm^{-1}*	542 cm^{-1}	*554 cm^{-1}*	571 cm^{-1}	602 cm^{-1}
626 cm^{-1}	637 cm^{-1}	658 cm^{-1}	*677 cm^{-1}*	700 cm^{-1}	701 cm^{-1}
736 cm^{-1}	*737 cm^{-1}*	*749 cm^{-1}*	755 cm^{-1}	*767 cm^{-1}*	778 cm^{-1}
809 cm^{-1}	821 cm^{-1}	825 cm^{-1}	*850 cm^{-1}*	880 cm^{-1}	884 cm^{-1}
907 cm^{-1}	*930 cm^{-1}*	944 cm^{-1}	955 cm^{-1}	975 cm^{-1}	*989 cm^{-1}*
1021 cm^{-1}	1055 cm^{-1}	1059 cm^{-1}	1095 cm^{-1}	1115 cm^{-1}	1117 cm^{-1}
1128 cm^{-1}	1133 cm^{-1}	*1137 cm^{-1}*	1170 cm^{-1}	*1190 cm^{-1}*	1212 cm^{-1}
1220 cm^{-1}	1254 cm^{-1}	1263 cm^{-1}	1300 cm^{-1}	1328 cm^{-1}	1373 cm^{-1}
1387 cm^{-1}	1413 cm^{-1}	1417 cm^{-1}	1447 cm^{-1}	1462 cm^{-1}	1473 cm^{-1}
1504 cm^{-1}	*1517 cm^{-1}*	*1525 cm^{-1}*	*1533 cm^{-1}*	1540 cm^{-1}	1568 cm^{-1}
1568 cm^{-1}	1599 cm^{-1}	1625 cm^{-1}	1646 cm^{-1}	1664 cm^{-1}	1702 cm^{-1}
1758 cm^{-1}	*1782 cm^{-1}*	*1800 cm^{-1}*	1825 cm^{-1}	*1860 cm^{-1}*	*1892 cm^{-1}*
1926 cm^{-1}	*1968 cm^{-1}*	*1992 cm^{-1}*	*2057 cm^{-1}*	*2151 cm^{-1}*	*2291 cm^{-1}*
2360 cm^{-1}	*2439 cm^{-1}*	*2491 cm^{-1}*			

BMIM PF_6 Raman band positions

418 cm^{-1}	*429 cm^{-1}*	442 cm^{-1}	*461 cm^{-1}*	472 cm^{-1}	*485 cm^{-1}*
498 cm^{-1}	*525 cm^{-1}*	*537 cm^{-1}*	*552 cm^{-1}*	568 cm^{-1}	601 cm^{-1}
602 cm^{-1}	624 cm^{-1}	655 cm^{-1}	701 cm^{-1}	713 cm^{-1}	*729 cm^{-1}*
742 cm^{-1}	*756 cm^{-1}*	775 cm^{-1}	807 cm^{-1}	*818 cm^{-1}*	826 cm^{-1}
842 cm^{-1}	866 cm^{-1}	882 cm^{-1}	909 cm^{-1}	930 cm^{-1}	947 cm^{-1}
976 cm^{-1}	995 cm^{-1}	1026 cm^{-1}	1057 cm^{-1}	1066 cm^{-1}	1091 cm^{-1}
1116 cm^{-1}	1134 cm^{-1}	1147 cm^{-1}	1167 cm^{-1}	1186 cm^{-1}	1211 cm^{-1}
1237 cm^{-1}	1255 cm^{-1}	*1259 cm^{-1}*	1281 cm^{-1}	1309 cm^{-1}	1340 cm^{-1}
1389 cm^{-1}	1421 cm^{-1}	1449 cm^{-1}	1467 cm^{-1}	*1472 cm^{-1}*	1496 cm^{-1}
1518 cm^{-1}	1537 cm^{-1}	1570 cm^{-1}	*1608 cm^{-1}*	*1631 cm^{-1}*	*1633 cm^{-1}*
1655 cm^{-1}	*1680 cm^{-1}*	*1729 cm^{-1}*	*1785 cm^{-1}*	*1879 cm^{-1}*	

BMIM TFSA Raman band positions

176 cm^{-1}	*207 cm^{-1}*	*278 cm^{-1}*	*313 cm^{-1}*	*332 cm^{-1}*	405 cm^{-1}
414 cm^{-1}	*440 cm^{-1}*	458 cm^{-1}	*462 cm^{-1}*	*478 cm^{-1}*	501 cm^{-1}
511 cm^{-1}	534 cm^{-1}	554 cm^{-1}	*555 cm^{-1}*	571 cm^{-1}	574 cm^{-1}
590 cm^{-1}	597 cm^{-1}	624 cm^{-1}	*645 cm^{-1}*	654 cm^{-1}	684 cm^{-1}
742 cm^{-1}	764 cm^{-1}	797 cm^{-1}	807 cm^{-1}	825 cm^{-1}	859 cm^{-1}
882 cm^{-1}	908 cm^{-1}	946 cm^{-1}	*959 cm^{-1}*	976 cm^{-1}	1025 cm^{-1}
1057 cm^{-1}	*1061 cm^{-1}*	1090 cm^{-1}	*1112 cm^{-1}*	1114 cm^{-1}	1137 cm^{-1}
1177 cm^{-1}	1200 cm^{-1}	*1213 cm^{-1}*	1243 cm^{-1}	1281 cm^{-1}	*1301 cm^{-1}*
1304 cm^{-1}	1311 cm^{-1}	*1331 cm^{-1}*	1338 cm^{-1}	1357 cm^{-1}	1389 cm^{-1}
1419 cm^{-1}	*1422 cm^{-1}*	1432 cm^{-1}	1452 cm^{-1}	1465 cm^{-1}	*1476 cm^{-1}*
1526 cm^{-1}	*1541 cm^{-1}*	1570 cm^{-1}	1609 cm^{-1}	1630 cm^{-1}	*1691 cm^{-1}*
1713 cm^{-1}	*1763 cm^{-1}*	*1805 cm^{-1}*	*1875 cm^{-1}*	*1969 cm^{-1}*	*2053 cm^{-1}*
2153 cm^{-1}	*2274 cm^{-1}*	*2359 cm^{-1}*			

BMMIM TFSA Raman band positions

175 cm^{-1}	*279 cm^{-1}*	*313 cm^{-1}*	*328 cm^{-1}*	*341 cm^{-1}*	404 cm^{-1}
492 cm^{-1}	506 cm^{-1}	535 cm^{-1}	553 cm^{-1}	557 cm^{-1}	574 cm^{-1}
589 cm^{-1}	*591 cm^{-1}*	609 cm^{-1}	630 cm^{-1}	*633 cm^{-1}*	666 cm^{-1}
706 cm^{-1}	725 cm^{-1}	*729 cm^{-1}*	742 cm^{-1}	762 cm^{-1}	798 cm^{-1}
805 cm^{-1}	825 cm^{-1}	*858 cm^{-1}*	883 cm^{-1}	*891 cm^{-1}*	908 cm^{-1}
943 cm^{-1}	965 cm^{-1}	965 cm^{-1}	1015 cm^{-1}	1051 cm^{-1}	1056 cm^{-1}
1078 cm^{-1}	1113 cm^{-1}	*1115 cm^{-1}*	1138 cm^{-1}	1187 cm^{-1}	1195 cm^{-1}
1243 cm^{-1}	1273 cm^{-1}	1309 cm^{-1}	1311 cm^{-1}	1340 cm^{-1}	1350 cm^{-1}
1389 cm^{-1}	1427 cm^{-1}	1448 cm^{-1}	1455 cm^{-1}	1466 cm^{-1}	*1474 cm^{-1}*
1517 cm^{-1}	*1554 cm^{-1}*	1590 cm^{-1}	*1809 cm^{-1}*	*2049 cm^{-1}*	*2154 cm^{-1}*
2271 cm^{-1}	*2353 cm^{-1}*	*2418 cm^{-1}*	*2449 cm^{-1}*		

BMPY TFSA Raman band positions

281 cm^{-1}	*308 cm^{-1}*	*334 cm^{-1}*	405 cm^{-1}	*419 cm^{-1}*	457 cm^{-1}
493 cm^{-1}	*494 cm^{-1}*	553 cm^{-1}	563 cm^{-1}	573 cm^{-1}	591 cm^{-1}
631 cm^{-1}	655 cm^{-1}	*667 cm^{-1}*	*706 cm^{-1}*	722 cm^{-1}	742 cm^{-1}
764 cm^{-1}	796 cm^{-1}	806 cm^{-1}	826 cm^{-1}	*843 cm^{-1}*	*886 cm^{-1}*
904 cm^{-1}	*905 cm^{-1}*	930 cm^{-1}	954 cm^{-1}	*970 cm^{-1}*	1005 cm^{-1}
1019 cm^{-1}	1052 cm^{-1}	1060 cm^{-1}	1121 cm^{-1}	1137 cm^{-1}	1184 cm^{-1}
1197 cm^{-1}	*1231 cm^{-1}*	1243 cm^{-1}	*1261 cm^{-1}*	*1273 cm^{-1}*	1330 cm^{-1}
1355 cm^{-1}	*1437 cm^{-1}*	1456 cm^{-1}	1465 cm^{-1}	1490 cm^{-1}	1538 cm^{-1}
1570 cm^{-1}	1602 cm^{-1}	1614 cm^{-1}	1636 cm^{-1}	*1657 cm^{-1}*	*1689 cm^{-1}*
1700 cm^{-1}	*1742 cm^{-1}*	*1776 cm^{-1}*	*1806 cm^{-1}*	*1862 cm^{-1}*	*1916 cm^{-1}*